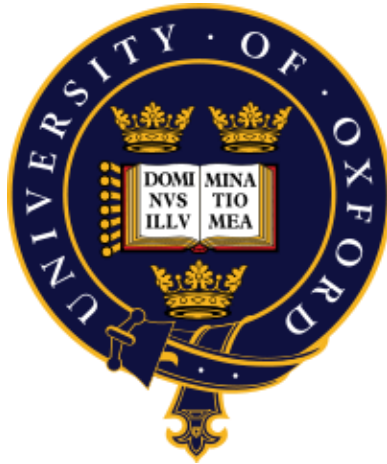


**Utilization of Exterior Surface Dimples for Stream-Wise
Force Reduction for a Circular Cylinder in Cross-Flow**

Minchao Wu (Francis)

Linacre College



A thesis submitted in partial fulfilment of the requirements of the degree of
Master of Science by Research at the University of Oxford
Trinity Term, 2010

Supervised by Professor Roger Ainsworth and Professor Li He

Southwell Laboratory (Osney)
Department of Engineering Science
University of Oxford

**Utilization of Exterior Surface Dimples for Stream-Wise Force
Reduction for a Circular Cylinder in Cross-Flow**

Minchao Wu (Francis)

Linacre College

A thesis submitted in partial fulfilment of the requirements of the degree of
Master of Science by Research at the University of Oxford
Trinity Term, 2010

Abstract

Applying dimples on spherical bluff bodies have been found to be a major technique to control the surface flow and reduce the stream-wise force. However, not much work has been done on dimple applications on cylindrical Objects .

This research project aims to investigate, firstly, whether the stream-wise force on a circular cylinder could be reduced by using dimples on its outer surface. Secondly, if it could, whether there is an optimum design that gives the biggest force reduction. Thirdly, what the roles of different approaches in this project might be?

In order to find answers to these questions, experimental and computational methods have been used. One smooth and three dimpled cylinders have been

tested. It was found that applying dimples on the outer surface of a cylinder is very effective in reducing stream-wise force. Drag coefficient significantly reduced by 17% to 48% depending on different Reynolds numbers. However, the dimpled design did not seem to be the key factor of the reduction, and the level of drag reduction was found to be insensitive to different dimpled patterns.

Furthermore, it has also been found that CFD method would not be suitable as the research tool for this project because of its demanding requirement in computer power. Therefore, rig tests remained the primary method for this project. In addition, flow visualization technique was also used to show the wake region behind both the smooth and dimpled cylinders. It was clear that a smaller wake was associated with the dimpled case, which resulted in the pressure drag on the dimpled cylinder being smaller than for the smooth cylinder.

For My Parents and Xin Zhang.

Acknowledgements

Firstly, I would like to thank Professor Roger Ainsworth and Professor Li He for their support over these years. There were a lot of challenges for me during this period, but my supervisors always accompanied and supported me whenever I needed.

The experimental work undertaken would not have been possible without the patient help of Gerald Walker and Peter Fair. They spent a lot of time helping me to build the rig and different test equipment.

Thanks also go to the research students and staff at Osney Laboratory: Dr Qiang Zhang, Richard Fawcett, Adam Jackson, Ian Helms, Devin O'Dowd, and all others. I have really enjoyed the friendly environment over the years.

I acknowledge the support of the Korea Institute of Geoscience and Mineral Resources (KIGAM) for its funding of this project.

Last, but by no means least, I would like to thank my mother, father, and Xin Zhang for their unfailing love, support, and inspiration.

Table of Contents

1. Introduction.....	1
1.1 Project Background and Overview	1
1.2 Aims and Objectives of the Project	4
1.3 Significance of the Project.....	6
1.4 Summary of Introduction.....	6
1.5 Thesis Structure	8
2. Background on the Flow Physics and Literature Review	10
2.1 Flow Physics Analysis	11
2.1.1 Assumptions and Flow Regime Classifications.....	11
2.1.2 Concepts of Boundary Layer	17
2.1.3 Laminar and Turbulent Boundary Layers.....	17
2.1.4 Separation of Boundary Layers	18
2.1.5 Promotion of Boundary Layer and Significance	20
2.1.6 Forces and Effective Phenomena in the Stream-Wise Direction.....	29
2.2 Definition and Key Parameters of a Dimple.....	30
2.3 Review of the Open Literature.....	30
2.4 Summary of Literature Review.....	37
3. Preparations and Experimental Setups	39
3.1 Experimental Objectives and Proposal	40
3.2 Design and Construction of Experimental Facilities	41

3.2.1 Design of the Wind Tunnel and Test Rig	41
3.2.2 Design of the PCB Circuits and Sensor Calibrations	52
3.2.2 Design of the Data Acquisition Unit.....	54
3.2.3 Performance of the Fan.....	55
4. Results and Discussion.....	56
4.1 Results and Discussion on the Smooth Cylinder	56
4.1.1 Design of the Smooth Cylinder and Measurements	56
4.2 CFD Modelling of a Smooth Cylinder	61
4.3 Results and Discussion on Different Dimpled Cylinders	68
4.4 CFD Simulations and Results on Different Dimpled Designs	83
4.4.1 Conclusions on CFD Side.....	91
4.5 Comparison between Experimental and Computational Methods	91
4.6 Checking the Time-Mean Lift Coefficient	92
4.7 Uncertainty and Repeatability of the Experiments	92
4.8 Conclusions on Results and Discussions	99
4.9 Differences between Experiments and Real Life Situations	100
5. Flow Visualization.....	102
5.1 Introduction of the Smoke Generator	102
5.2 Successful “L-shape” Probe.....	104
5.2.1 Results on Flow Visualization	105
5.3 Conclusion on Flow Visualization Experiments	109

6. Summaries and Conclusions	111
6.1 Preparations and Experimental Setups	111
6.2 Results and Discussions of Smooth Cylinder	112
6.3 Results and Discussions on Dimpled Cylinders	113
6.4 Time-Average Lift Coefficient and Repeatability of Experiments	115
6.5 Flow Visualization	116
7. Suggestions on Possible Further Work.....	117
References.....	119
Appendix I – Schematics of the LabView Code	126
Appendix II – A Sample of the Raw Experimental Data	127
Appendix III – Gantt Chart of the Project Progress	128

List of Figures

Figure 1 Schematics of the lifting system for manganese nodules from the seabed	3
Figure 2 Top view and side view of the cylinder	12
Figure 3 Cd variations with respect to Re for cylinder and sphere (White, 2003)	16
Figure 4 Boundary layer on a flat plate (Massey, 2005)	18
Figure 5 Flow separations around a cylinder (Massey, 2005).....	18
Figure 6 Velocity profile during separation (Massey, 2005).....	20
Figure 7 Cd variations for spheres with different surface roughness (Achenbach, 1974).....	21
Figure 8 Variation of Cd with Re for smooth, sand-roughened, and dimpled cylinders (Bearman and Harvey, 1993)	21
Figure 9 Figure scanned from Achenbach, 1974	22
Figure 10 Figure scanned from Maxworthy, 1969	25
Figure 11 Figure scanned from Nakamura and Tomonari, 1982.....	25
Figure 12 Figure scanned from Choi et al., 2006	26
Figure 13 Figure scanned from Choi et al., 2006	27
Figure 14 Schematic diagram of drag-reduction mechanism by dimples (Choi et al., 2006)	28
Figure 15 Friction coefficient with respect to total drag coefficient (Achenbach, 1968).....	29
Figure 16 A circular cylinder with dimples (Bearman and Harvey, 1993)	32
Figure 17 A small cylinder in the shear layer of the test cylinder (Igarishi and Tsutsui, 1992)	33

Figure 18 A control cylinder placed upstream of the main cylinder (Tsutsui and Igarashi, 2002)	33
Figure 19 Schematic of circular cylinder with sinuous axis (Owen et al., 2001)..	35
Figure 20 Circular cylinder fitted with surface control bumps (Owen et al., 2001)	35
Figure 21 Schematic of perforated shroud and helical cables around the cylinder (Chung and Whitney, 1993).....	36
Figure 22 A blower with a convergent section fitted behind.....	42
Figure 23 Mean drag coefficient vs cylinder aspect ratio: (a) $Re = 4.3 \times 10^4$, (b) $Re = 1.3 \times 10^6$ (Szepessy and Bearman, 1991).....	43
Figure 24 Picture showing the convergent section, straight working section, traverse system, and test cylinder	44
Figure 25 C_p distributions for two different cases	46
Figure 26 Schematic diagram of the test section	47
Figure 27 Schematic of a pitot-static probe (Massey, 2005)	47
Figure 28 Picture of the blower, convergent, and straight working section	51
Figure 29 Equipment used to calibrate the pressure transducers.....	52
Figure 30 Calibration graph for ± 2.5 mbar pressure transducer.....	53
Figure 31 Graph showing a linear relation between fan speed and Re	55
Figure 32 Smooth cylinder fitted with 36 pressure tapings	57
Figure 33 Close up view of the pressure tapings on the smooth cylinder	57
Figure 34 Three different cases for measuring the pressure distribution around the cylinder	59

Figure 35 Pressure coefficient plot against different Reynolds numbers (part one)	59
Figure 36 Pressure coefficient plot against different Reynolds numbers (part two)	60
Figure 37 Lift coefficient vs flow time of a smooth cylinder in laminar flow	63
Figure 38 CFD domain for smooth cylinder simulation	64
Figure 39 Schematics of the mesh around the smooth cylinder	64
Figure 40 Vortex shedding behind a smooth cylinder	65
Figure 41 Pressure coefficients from experiment and CFD prediction at 1×10^5	67
Figure 42 C_p around a cylinder for laminar BL, turbulent BL, and theoretical prediction (Massey, 2005)	67
Figure 43 Variation of C_d with Re for smooth, sand-roughened, and dimpled cylinders (Bearman and Harvey, 1993)	69
Figure 44 The dimpled cylinder specimen	70
Figure 45 C_d vs Re for smooth cylinder and mid-span tappings, none stagger dimpled cylinder	71
Figure 46 “matrix-type tappings, none stagger dimples” cylinder with pressure tapping matrix	72
Figure 47 Close up view of the pressure tapping matrix around one dimple	72
Figure 48 Modified dimpled cylinder (with sellotape)	74
Figure 49 Stagger dimpled cylinder	75
Figure 50 Close up view of the tapping matrix on the stagger dimpled cylinder	75
Figure 51 Schematic of the tapping matrix on the matrix-type and stagger dimpled cylinders	76

Figure 52 Comparisons of Cd for four cylinders	78
Figure 53 Quadrilateral mesh around the dimpled cylinder	85
Figure 54 Plot of drag coefficient against flow time	86
Figure 55 Schematics for measuring the pressure	93
Figure 56 Matrix-type dimpled cylinder with a small component near the top	94
Figure 57 A close up view of the component and the top of the cylinder	94
Figure 58 Cp plots with standard deviation error bar superimposed	96
Figure 59 Oil type smoke machine	102
Figure 60 Smoke machine put on top of the rig and connected to the probe	104
Figure 61 Picture showed the visualization result on the smooth cylinder when the probe was at position 65mm	105
Figure 62 Flow image when the probe was at position 85mm	106
Figure 63 Flow image when the probe was in position 105mm.....	106
Figure 64 Image showed the wake region behind the smooth cylinder.....	108
Figure 65 Flow visualization image for the dimpled cylinder.....	108

List of Tables

Table 1 Details of design I.....	44
Table 2 Details of design II.....	45
Table 3 Comparison of different sectional widths.....	45
Table 4 Calibration data for different pressure transducers.....	53
Table 5 Cd and Cd reduction for different cylinders	79
Table 6 Direction comparison between two dimpled cylinders	79
Table 7 Drag coefficient for different cases	85
Table 8 CFD results for preliminary coarse mesh cases.....	89
Table 9 Technical specification of the smoke generator	103

Nomenclature

Symbols, Abbreviations, and Acronyms

A	Reference area (m^2)
Cd	Drag coefficient (dimensionless)
CFD	Computation Fluid Dynamics
Cl	Lift coefficient (dimensionless)
Cp	Pressure coefficient (dimensionless)
D	Diameter of the pipe (mm)
d	Sphere diameter (mm)
DNS	Direct Numerical Simulation
E	Young's modulus of the pipe material
h	Length of the cylinder tube (mm)
Hz	Hertz (SI unit for frequency)
I	Moment of inertia of the structure ($\text{kg}\cdot\text{m}^2$)
k	Dimple depth (mm)
KIGAM	Korea Institute of Geoscience and Mineral Resources
LES	Large Eddy Simulation
m	Mass of the cylinder (kg)
P	Pressure at the cylinder surface (Pa)
P_∞	Static pressure in the free stream (Pa)
$P_{t\infty}$	Total pressure in the free stream (Pa)
RANS	Reynolds Average Navier-Stokes

Re	Reynolds number (dimensionless)
r.m.s	Root mean square
PIV	Particle Image Velocimetry
RPM	Revolutions per minute
S	Point of separation
S-A	Spalart-Allmaras turbulent model
SGS	Sub-grid scale
V	Velocity of the fluid (m/s)
VIV	Vortex-induced vibration
X	Stream-wise direction
x	Location along the beam (mm)
Y	Transverse direction
Z	Axial direction along the cylinder
ρ	Density of the fluid (kg/m^3)
μ	Dynamic viscosity of the fluid (N s/m^2)

Chapter 1

1. Introduction

This chapter considers the background of this research work and explains the need to conduct investigations on the application of using surface dimples on the outer surface of circular cylinders. Key questions to be answered of this research project will be stated in Section 1.1 and the significance of the project will be discussed in Section 1.3.

1.1 Project Background and Overview

Flow phenomena around bluff bodies such as golf balls and automobiles as well as circular cylinders have attracted research interests for many years. There are practical significances in civil engineering, ocean and coastal engineering, sports industries (e.g. golf, Formula 1), and so on.

Within the scope of the current research project, the investigation of the stream-wise force on a vertical mounted circular cylinder is the main purpose. And more specifically, the most important questions to be investigated and try to answer in this project are:

1. Whether is it really possible to reduce the stream-wise force by applying dimples on the outer surface of the circular cylinder?

2. If applying dimples did help to reduce the stream-wise force, can we find a best or optimum dimple design, which would give greatest force reduction?
3. Different research methods will be used in this research project, what are the roles and effectiveness of these methods? Is there any emphasis on some specific investigation techniques?

The application of this project is on the lifting pipe of the deep sea mining system, and the circular cylinder is a typical representation of the lifting pipe in this case. The vertical mounted circular cylinder is a part of the whole mining system. This mining system typically consists of a collecting system, a lifting system, and a mining platform (as indicated in Figure 1). The mining material, manganese, is firstly collected from the seabed and then transported by the lifting system upwards to the mining platform located on the ocean surface. A pipe with a circular cross section is fitted vertically and serves as a lifting pipe in this mining system. Sea water coming from the normal direction (cross-flow) to the pipe interacts with this pipe, and stream-wise force (drag) will be generated as a result.

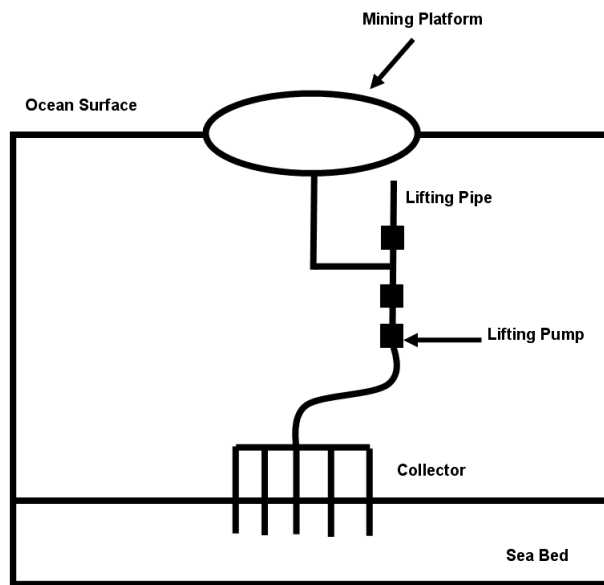


Figure 1 Schematics of the lifting system for manganese nodules from the seabed

The practical engineering need of reducing the stream-wise force on the lifting pipe can help to alleviate some useful engineering issues in this mining application. For example: reducing the force on the holding of the pipe, potential bending deformation of the pipe, and even structure failure. Different reduction techniques could be found in the literature and will be discussed in more details later in the literature review section. These include surface dimples, helical cables around the cylinder, perforated shroud outside the cylinder, applying a controlled cylinder upstream of the main test cylinder, and some other methods as well. However, it is also worth recalling that the focus of this project is to investigate exterior surface dimples in stream-wise force reduction rather than other schemes mentioned above. However, by reviewing other techniques can also provide information on the flow behaviour and hints on potential dimple designs.

Because a circular cylinder is a typical representation of the lifting pipe, therefore, a circular cylinder is used in this project to study the stream-wise force. As mentioned, the application of this piece of work is on the lifting pipe of the deep sea mining system, and it is under the sponsorship of Korea Institute of Geoscience and Mineral Resources (KIGAM).

1.2 Aims and Objectives of the Project

The three most important objectives of this project were mentioned in Section 1.1, which was also the main theme of the research work. And this thesis will try to find answers to those questions.

To achieve these goals, information on techniques for stream-wise force reduction on circular cylinders is needed in order to make useful suggestions. For example, some aspects include:

- a. Understanding the flow behaviour when a circular cylinder is placed in cross-flow. This includes different flow regimes, pressure distribution around the cylinder, flow separation, promotion of boundary layer transition, fluid–structure interaction, and so on.
- b. Researching and studying the existing literature on different techniques for stream-wise force reduction, especially key publications using exterior surface dimples.

- c. Carefully selecting the measurement instruments and components and then building the experimental facilities as well as the test rig.
- d. Experimentally testing a circular cylinder with smooth surface and comparing it with the prediction from the Computational Fluid Dynamics (CFD) method.
- e. Designing and then testing circular cylinders experimentally with different dimpled configurations (shape, number, distribution, and depth of dimples).
- f. Comparing results obtained from various designs.
- g. Conducting more simulations by CFD methods, and comparing with the experimental data.
- h. Using flow visualization technique to show the wake region behind smooth and dimpled cylinders, and hopefully support the results.
- i. Based on the results, answering the key questions clearly indicated in Section 1.1 and then giving suggestions on stream-wise force reduction.

1.3 Significance of the Project

Reducing the stream-wise force on a lifting pipe with dimples on the outer surface has both practical significance and research importance. In terms of the practical aspect, reducing this force on the lifting pipe can help to alleviate realistic engineering issues like reducing the huge force on the holding of the pipe, potential bending deformation of the pipe, and even structure failure as mentioned in the project background.

From the research point of view, this project can contribute more information to the existing literature, and it is a further investigation after the work by **Bearman and Harvey, 1993**. Not many publications were found on this topic so far; the majority of work is applying dimples on spheres rather than on cylindrical objects. From the review of the literature, it is widely accepted that applying dimples on the outer surface is an effective way of reducing the stream-wise force on bluff bodies. Researchers have tried to understand and explain the flow physics by using both experimental and computational techniques. However, an optimum value or maximum reduction has not been reported to the author's knowledge.

1.4 Summary of Introduction

The purpose of this chapter serves to give some background information on this research project. This project aims to answer several key questions. First of all, whether applying exterior dimples on the circular cylinder can reduce the stream-wise force on the cylinder? Secondly, if this was indeed effective, will there be an

optimum dimpled design, which results in the greatest force reduction? And thirdly, what are the roles and effectiveness of different research methods in this project?

The main structure and outline of this thesis are: firstly understand and analyse relevant flow physics, for example, classifications of different flow regimes, pressure distribution around a cylinder and flow separation, fluid-structure interaction, and so on. Secondly, available reduction techniques in the open literature will be reviewed, with special emphasis on dimples on cylinder. Thirdly, in the main section of the experiment, it will be divided into experimental tests in the wind tunnel, and Computational Fluid Dynamics (CFD) simulations on the computer. These two methods are not restricted to one specific cylinder. Instead, different cylinder designs, with different dimpled patterns will be considered as well. Next, results will be compared and conclusions will be drawn. After the work mentioned above, flow visualization is going to use to show the differences of the separation wake regions for smooth and dimpled cylinders and hopefully support the conclusions made in the corresponding sections.

By finishing the main work, it is intended to be able to show using dimples on the outer surface of the circular cylinder can indeed reduce the stream-wise force. At the same time, answer the question of whether it is possible to propose the best dimpled design. Also, what are the roles of the experimental and computational techniques, which will be used in this project? In the flow visualization section,

can it really show the dimpled cylinder has a smaller wake region than the smooth one, which results in a smaller pressure drag for dimpled cylinders?

Last, but by no means least, results from different sections of the research work will be summarized. And finally, some suggestions on possible future work will be given.

1.5 Thesis Structure

This thesis is divided into the following chapters:

Chapter 2 reviews the relevant flow behaviours, for example, pressure distribution around a cylinder, boundary layer theories and promotion of boundary layer transition, steady flow around a cylinder, etc. Besides, existing reduction techniques reported in the literature will be reviewed and summarized.

Chapter 3 describes different aspects of preparation for the experiments. In this chapter, dimensions for different sections/components will be defined. Suitable sensors are selected, calibrated, and also used to build the circuits. And then, data acquisition unit will be connected between the sensors and the computer. Inside the computer, LabView codes will be developed to obtain the signals.

Chapter 4 discusses both the experimental and computational results. Investigations will be done on a smooth cylinder and several different dimpled cylinders. This chapter also compares the experimental and CFD techniques,

trying to decide which one is more suitable for this research project. Furthermore, the time-mean lift coefficient will be calculated as well as checking the repeatability of the experiments.

Chapter 5 separately summarizes different aspects for implementing flow visualization in the wind tunnel test rig. And then, detailed design progress and how to obtain successful images will be described. A brief conclusion on flow visualization will be given at the end of this section.

Chapter 6 quickly reminds the readers about the aims and objectives of this project, and then re-emphasizes various conclusions made in previous chapters.

Chapter 7 outlines possible directions for further investigation in the future.

Chapter 2

2. Background on the Flow Physics and Literature Review

There are some similarities when flow passes around spheres and circular cylinders, especially dimpled spheres and dimpled cylinders. For example, in the case of golf ball dimples, it is believed that small scale longitudinal vortices are generated at the edge of the dimples and these propagate back as trailing vortices to energize the boundary layer, thus delaying separation (**Bearman and Harvey, 1976**). This behaviour is considered to be comparable to the dimpled flow in circular cylinders.

This project and thesis concentrate on the stream-wise force on cylinders. However, this particular chapter will start with reviewing phenomena related to smooth spheres and then dimpled spheres before extending to cylindrical objects. Reduction techniques related to both spherical and cylindrical objects can offer information on the flow physics as well as reduction mechanism.

Therefore, in this chapter, various reduction methods will be summarized and then analyse the mechanisms.

2.1 Flow Physics Analysis

2.1.1 Assumptions and Flow Regime Classifications

A few assumptions will be made before further analysis of the flow interaction between the flow and the lifting pipe:

- a. The method of fixing the lifting pipe is assumed to be held at both ends of the pipe.
- b. Assuming the ocean current near the surface is steady, the pipe does not experience significant wakes or oscillatory flows.
- c. The average depth of the ocean around the world is reported less than 4,000 metres. In some cases, deep sea mining can go deeper than that. For the present studies, it is preliminarily suppose a mining depth from the ocean surface of 1,000 metres and length of the straight lifting pipe equals to 500 metres.
- d. Take the western-flowing currents for example. It is shown by **Pidwirny et al., 2006**, the surface current is generally restricted to the upper 100 to 200 metres of the ocean, which is in the normal direction (the X direction as shown in Figure 2) to the lifting pipe.

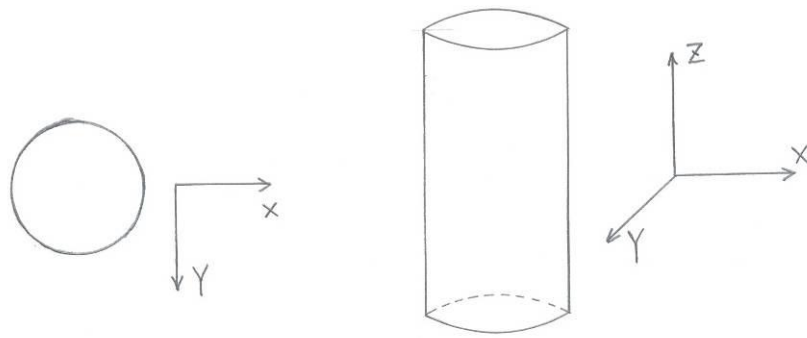


Figure 2 Top view and side view of the cylinder

- e. For simplicity, this work assumes the flow coming from the normal direction has a linear velocity profile along the vertical direction (Z direction). Therefore, a typical current speed is around 1 m/s on the ocean surface and decreases linearly downwards along the pipe. The flow is considered to be static below at 200 metres and remained at this value below 200 metres.
- f. As a result of the previous assumptions, it is indicated that the lifting pipe is not submerged in a uniform Reynolds number. It effectively covers a very wide range of Reynolds numbers.
- g. However, it is not easy to obtain a linear velocity profile in the experiments. Hence, different up-coming flow velocities will be obtained by varying the flow velocity, and in turns changing the Reynolds number. In every single experiment, the flow velocity will be set to constant.

- h. The outside diameter of the pipe is taken to be 1 metre as an initial approximation.

- i. The movement of the sea water in the lower section of the ocean is mainly driven by the differences in temperature and salinity. Hence, natural convection occurs and water travels vertically. However this force in the Z direction will be neglected as it does not contribute much to the stream-wise force in the X direction.

Experiments in this project will be conducted in a low speed wind tunnel. By contrast, in the deep sea mining application, the fluid is sea water. This implies there are two different fluid media, i.e., air and sea water. However, due to the similarity in fluid mechanics, results are applicable as long as the Reynolds numbers in the experiments are matched with those in the real-life scenario.

An important parameter, Reynolds number (Re), will be introduced at this point. Reynolds number is a non-dimensional number in fluid dynamics. If two geometrically similar flow patterns have similar values of their respective Reynolds numbers, even for different fluids and possibly different flow velocities, they are said to be fluid dynamically similar. Reynolds number is the ratio of the inertial force and friction force, which is defined as (**White, 2003**):

$$\text{Re} = \frac{\text{inertial_force}}{\text{viscous_force}} = \frac{\rho V D}{\mu} \quad \text{Equation 1}$$

where:

ρ is the density of the fluid

V is the velocity of the fluid

D is the diameter of the pipe

μ is the dynamic viscosity of the fluid

According to Equation 1 and the assumptions made previously, Reynolds number on the ocean surface equals 1×10^6 . Because all other parameters are constant except the flow velocity, Reynolds number also changes linearly downwards to zero at the depth of 200 metres, and then stays at this value (0) in deeper regions. Specific values of different parameters in the assumptions are estimated from typical values, they would not affect the actual flow physics as long as Reynolds numbers are matched.

When flow comes from the normal direction towards the cylinder, two major forces will be created: force in the stream-wise (X) direction (alternatively, this force could be called pressure drag) and lift in the traverse (Y) direction. Lift periodically alters in the positive and negative Y directions. In this project, the aim is to investigate the reduction of the time-average, integrated force in the stream-wise direction. The other drag component, fluctuation drag, is outside the scope of the current studies and it requires many complicated modifications of the

test rig to conduct the research. For example, more sensitive pressure transducers or even hot wire probes, putting the sensors much closer to the pressure tappings, and possibly developing a transfer function for the signal adjustment. Therefore, at this stage, it is confined to investigate the time-mean stream-wise force in the X direction. Furthermore, over a certain period of time, the sum of the time-mean lift in the Y direction will always equal zero. For these reasons, this project will investigate the time-mean stream-wise force in the X direction only.

Sometimes, it would be convenient to express this stream-wise force in a non-dimensional format, that is, the drag coefficient. In fluid dynamics, drag coefficient (C_d) is a dimensionless parameter which is used to quantify the drag force or resistance of an object in a fluid environment, such as air or water. It is defined as:

$$C_d = \frac{\text{Drag}}{0.5\rho V^2 A} \quad \text{Equation 2}$$

where:

ρ is the density of the fluid

V is the velocity of the fluid

A is the reference area

Drag coefficients for a smooth cylinder and a smooth sphere are plotted in Figure 3 as a function of the Reynolds number. In the region of $1 \times 10^3 < Re < 3 \times 10^5$, which is classified as subcritical region, the drag coefficient curve for cylinder stays roughly at a constant value of 1.2. As it goes through the transitional region,

the C_d curve drops suddenly and reaches a minimum value about 0.3 at around $Re = 5 \times 10^5$. Beyond this Reynolds number, in the supercritical regime, C_d gradually recovers and reaches 0.6.

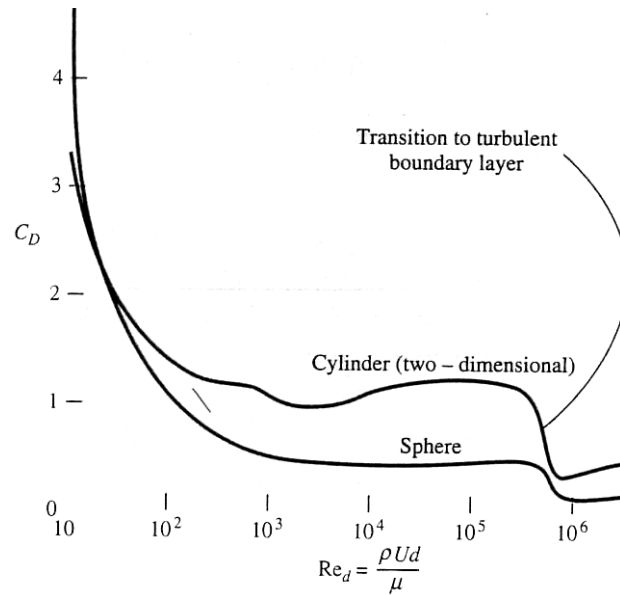


Figure 3 C_d variations with respect to Re for cylinder and sphere (White, 2003)

Transition occurs over a range of Reynolds numbers and $2 \sim 3 \times 10^5$ is a widely accepted region that ensures transition has occurred for circular cylinders. The flow region of $10^3 < Re < 10^6$ mentioned earlier covers the subcritical, transitional, and supercritical regimes classified. This range actually corresponds to the flow on the ocean surface down to 99.9% of the 200 meters along the Z direction, where it is the depth assumed the fluid has no motion in the X direction. Below this depth, effects from the fluid flow can then be neglected, even it is still possible to further categorize different flow regimes into creeping flow, vortex pairs in wake, and von Karman Vortex Street at lower Re ranges (Schlichting and

Gersten, 2000, Sumer and Fredsoe, 1999). These effects are not significant in the scale of this project.

2.1.2 Concepts of Boundary Layer

In classical fluid mechanic theories, it is assumed that the flow is inviscid, which leads to the well-known D'Alembert's paradox (1752) (**Anderson, 2001**). It predicts that there is no drag force on a body placed in incompressible and inviscid flow. However, experiments show that a drag force really exists. In 1904, Ludwig Prandtl posed the idea known as the boundary layer (**Schlichting and Gersten, 2000**).

The boundary layer concept indicates that flows can be divided into two unique regions. In the majority of the flow region, effects due to viscosity can be neglected, and the flow corresponds to the inviscid solution. This is called the inviscid outer flow. The second region is the very thin boundary layer immediately next to the bounding surface, where the viscosity effect must be taken into account. This boundary layer theory explains the present of drag force on a body experimented in a real flow.

2.1.3 Laminar and Turbulent Boundary Layers

Normally, there are two types of boundary layer, i.e., laminar boundary layer and turbulent boundary layer. Generally speaking, a boundary layer starts to grow from laminar behaviour, and then undergoes a transition region before reaching

the turbulent boundary layer status (Figure 4), where the drag coefficient drops suddenly. These two types of boundary layer have physical significances.

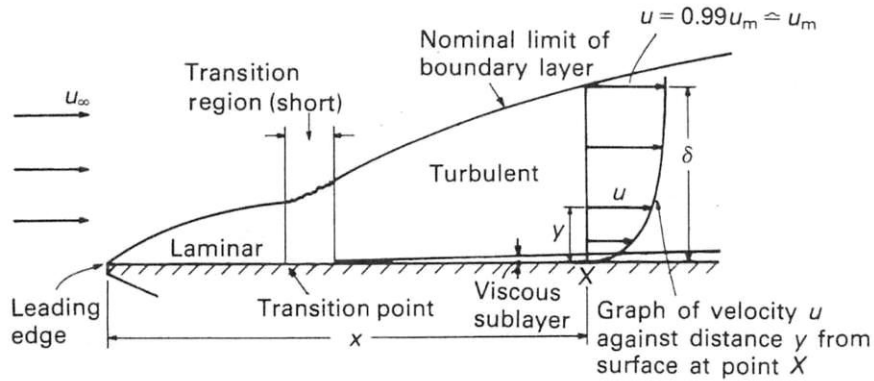


Figure 4 Boundary layer on a flat plate (Massey, 2005)

2.1.4 Separation of Boundary Layers

Figure 5 demonstrates two different flow patterns in different cases around a two-dimensional (2D) cylinder. When the laminar boundary layer develops, flow detaches and leaves the surface at about 80 degrees forming a large wake region. The position at which the flow detaches is called the point of separation (point S). It is given by the condition that the velocity gradient in the normal direction to the wall distinguishes; that is, the wall shear stress τ_w vanishes:

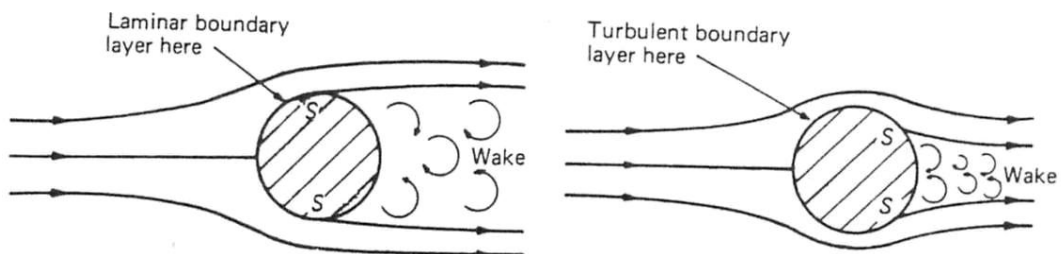


Figure 5 Flow separations around a cylinder (Massey, 2005)

$$\tau_w = \mu \left(\frac{\partial u}{\partial y} \right)_w = 0 \quad \text{Equation 3}$$

For the scenario with a turbulent boundary layer, the separation point moves backwards to about 120 degrees. This results in a smaller wake region. This region represents a section of low pressure. The pressure drag is the main source of the drag force on the cylinder in the X direction. The wake region at the back of the cylinder plays an important role in the total drag force. In the case with the turbulent boundary layer, this wake region is smaller than the one in the laminar boundary layer. Therefore, the pressure difference between the front and back surfaces is smaller compared with the laminar boundary layer case. According to Equation 4, the force is smaller when the turbulent boundary layer occurs.

$$\text{Force} = \text{pressure} \times \text{area} \quad \text{Equation 4}$$

Boundary layer separation occurs when static pressure increases in the flow direction, which is called an adverse pressure gradient. As shown in Figure 6, when an adverse pressure gradient slows down the flow parallel to the surface in the boundary layer, this velocity component eventually becomes zero at point S. The flow then separates from the surface and a wake region is created beyond the separation point. Downstream of the separation point, there is a region of flow reversal because static pressure keeps increasing. The fluid also re-circulates in

the opposite direction to the free-stream, and the low pressure on the surface of the body is not able to recover.

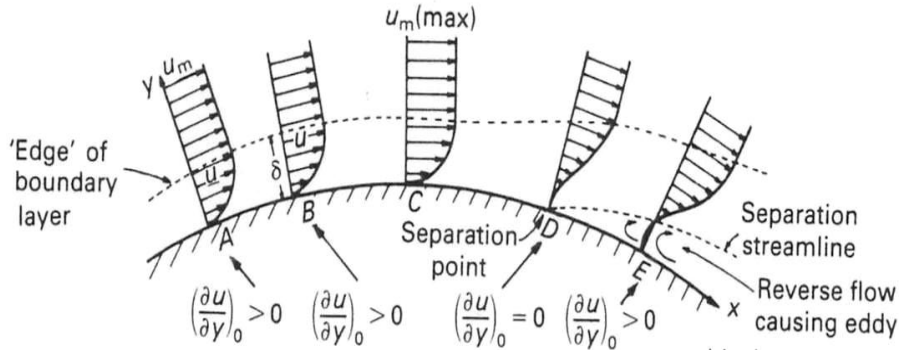


Figure 6 Velocity profile during separation (Massey, 2005)

2.1.5 Promotion of Boundary Layer and Significance

Surface roughness affects the behaviour of boundary layers and hence the drag coefficient considerably. **Achenbach, 1974**, carried out measurements of the drag coefficient for spheres with different ratios of average diameter (k) of the sand grain to sphere diameter (d). In his studies, sand paper was used to obtain the roughness and he investigated over the Reynolds number range of $5 \times 10^4 < Re < 6 \times 10^6$. Results were reproduced by **Bearman and Harvey, 1993**, and shown in Figure 7. The critical Reynolds number decreases as roughness parameter (k/d) increases, but the drag coefficient rises rapidly after a minimum value approaching a maximum value of 0.4 in the supercritical regime. **Bearman and Harvey, 1993**, indicated the increased C_d with increased surface roughness (Figure 7 and Figure 8) in the supercritical regime was thought to be mainly due to the roughness effect on the development of the turbulent boundary layer growing on the sphere. Therefore, the transition point moved forward.

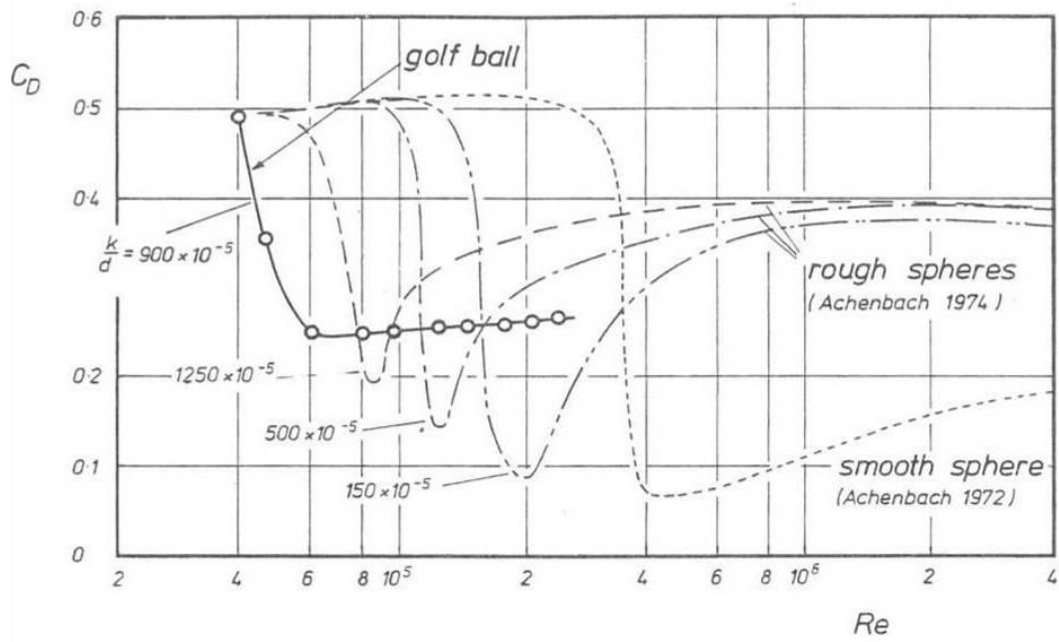


Figure 7 C_D variations for spheres with different surface roughness (Achenbach, 1974)

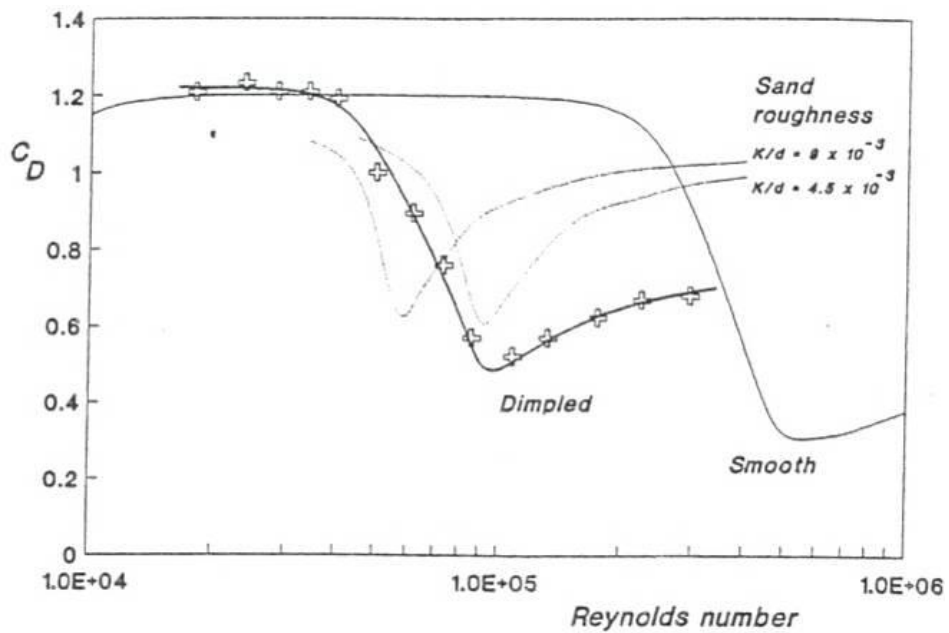


Figure 8 Variation of C_D with Re for smooth, sand-roughened, and dimpled cylinders (Bearman and Harvey, 1993)

Bearman and Harvey, 1976, Bearman and Harvey, 1993, compared the variation of drag coefficient with Reynolds number for a dimpled golf ball with Achenbach, 1974, for sand-grained spheres. The comparison is shown in Figure 7. The depth of golf ball dimples corresponded to the average sand grain diameter (k). Data showed that C_d increased with increasing surface roughness beyond the transition region on sand-grained spheres (Figure 9). This was mainly due to the effect of the roughness when the turbulent boundary grew on the sphere. It also indicated that dimples caused the drag coefficient to drop at a lower Reynolds number than for sand-roughened spheres.

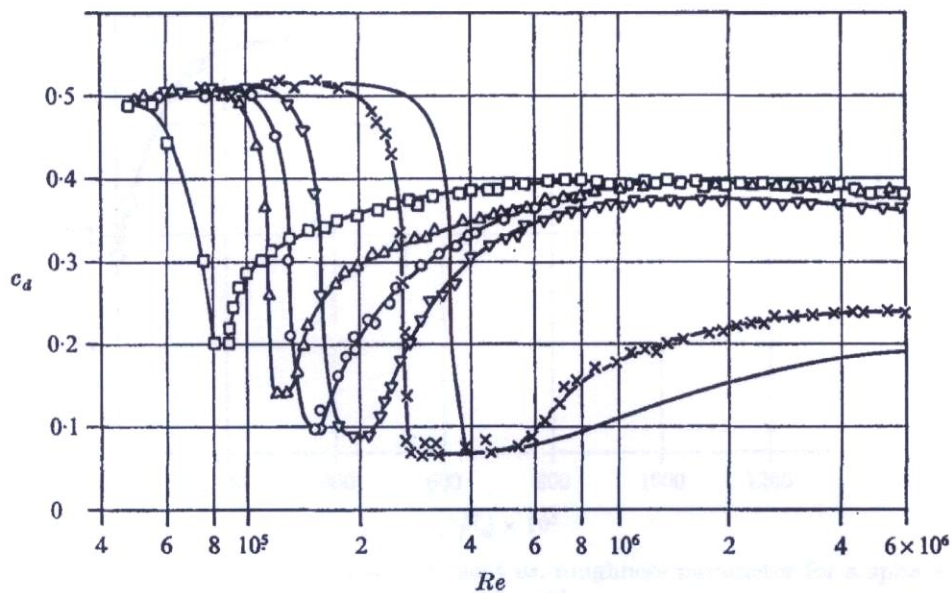


FIGURE 2. Drag coefficient c_d vs. Reynolds number for a sphere. Parameter: surface roughness. —, smooth (Achenbach 1972); \times , $k/d_s = 25 \times 10^{-5}$; ∇ , $k/d_s = 150 \times 10^{-5}$; \circ , $k/d_s = 250 \times 10^{-5}$; \triangle , $k/d_s = 500 \times 10^{-5}$; \square , $k/d_s = 1250 \times 10^{-5}$.

Figure 9 Figure scanned from Achenbach, 1974

For the golf ball with dimples, it was also shown that the drag coefficient curve remained at about 0.25 beyond the critical region, whereas it would rise rapidly after the minimum value and then approached to the C_d value of about 0.4. This implied the dimples were very effective in promoting the boundary layer transition as well as maintaining the C_d curve in a constant low value in the supercritical regime compared with the sand-grained spheres. Therefore, **Bearman and Harvey, 1993**, concluded that dimples were more beneficial than sand roughness.

Comparing the work by **Bearman and Harvey, 1993**, **Bearman and Harvey, 1976**, and **Achenbach, 1974**, it appeared dimples caused the critical regime for the dimpled cylinder to occur at a lower Reynolds number than that for a smooth cylinder (Figure 7 to Figure 9). **Bearman and Harvey, 1993**, also concluded the values of drag coefficient were very close in the supercritical regime for smooth and dimpled cylinders. Furthermore, they would not approach to the high values as those for sand-roughened cylinders beyond the minimum drag coefficient point.

It is known that separation would be delayed by the presence of dimples. However, there are not many research publications available that have successfully explained the process of generating a turbulent boundary layer by dimples. Therefore, **Bearman and Harvey, 1993**, offered a conjecture suggesting that dimples generated discrete vortices, which added more forward momentum to the boundary layer flow. However, no experimental data could be obtained to verify this conjecture because it was very difficult to measure the three-dimensional flow

around these dimples. For the same reason, the almost constant drag coefficient over a certain range of Reynolds numbers beyond the critical value were not explained very well. It was believed that dimples fix the position of transition a long way upstream in this range of Reynolds numbers, and keep the separation angle constant, leading to an almost constant drag coefficient (**Bearman and Harvey, 1976**). However, no experimental measurement data are available to support this.

The almost constant drag coefficient at the supercritical regime was also found for other kinds of surface modifications on a sphere by other researchers. For example, **Maxworthy, 1969**, observed this characteristic by putting a trip wire on the surface of a sphere. In his experiments, the trip wire was put in different locations as well as testing under various Reynolds numbers (Figure 10). The almost constant drag coefficient beyond the minimum value was confirmed throughout his experiments. **Nakamura and Tomonari, 1982**, obtained the same behaviour when they attached narrow roughness strips on the cylinder surface (Figure 11). They carried out experiments on a smooth cylinder with roughness strips attached. This specimen was tested in a wind tunnel capable of producing flow at high Reynolds numbers into the supercritical regime. It was intended to simulate the supercritical flow behaviour when pasting a smooth cylinder by promoting the boundary layer because of the roughness strips.

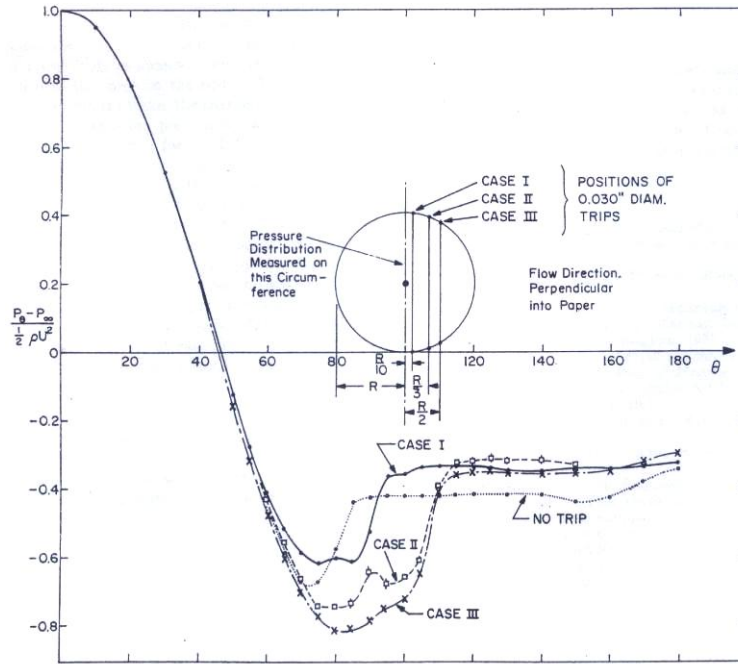


Fig. 13 Effect of side trip location for fixed size (0.030 in.) and $R = 2 \times 10^5$

Figure 10 Figure scanned from Maxworthy, 1969

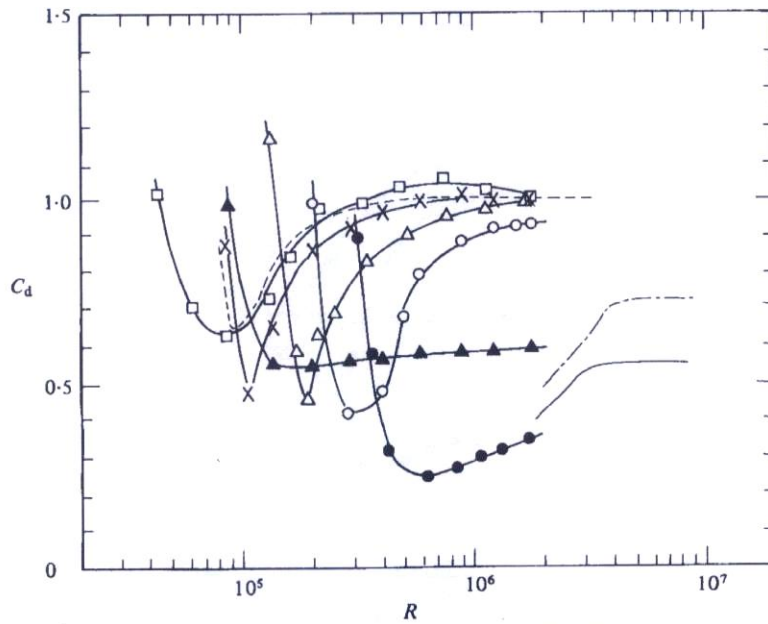


FIGURE 2. Drag coefficient. Smooth cylinders: - - - - - , Roshko (1961); — , Jones *et al.* (1969); ● , present experiments. Cylinders with distributed roughness: - - - - - , Achenbach (1971), $r/D = 881 \times 10^{-5}$ ($k_s/D = 450 \times 10^{-5}$); □ , present experiments, $r/D = 1000 \times 10^{-5}$; × , 516×10^{-5} ; △ , 226×10^{-5} ; ○ , 90×10^{-5} . Smooth cylinder with 3.2 mm diameter roughness strips at $\theta = 50^\circ$: ▲ , present experiments.

Figure 11 Figure scanned from Nakamura and Tomonari, 1982

After all these efforts, however, there was still no successful explanation why the drag coefficient remained almost constant for these surface modifications. A reasonable explanation of the mechanism by which dimples generate turbulence and why the drag coefficient remains almost constant over a range of Reynolds numbers was recently provided by **Choi et al., 2006**.

Choi et al., 2006, measured the stream-wise velocity above a dimpled surface (Figure 12) and provided an explanation for the drag reduction mechanism. In their paper, profiles of time-averaged stream-wise velocity as well as the root mean square (r.m.s) stream-wise velocity functions were shown for smooth and dimpled spheres for different Reynolds numbers (Figure 13), which could help to support their judgement on the almost constant drag coefficient over a wide range.

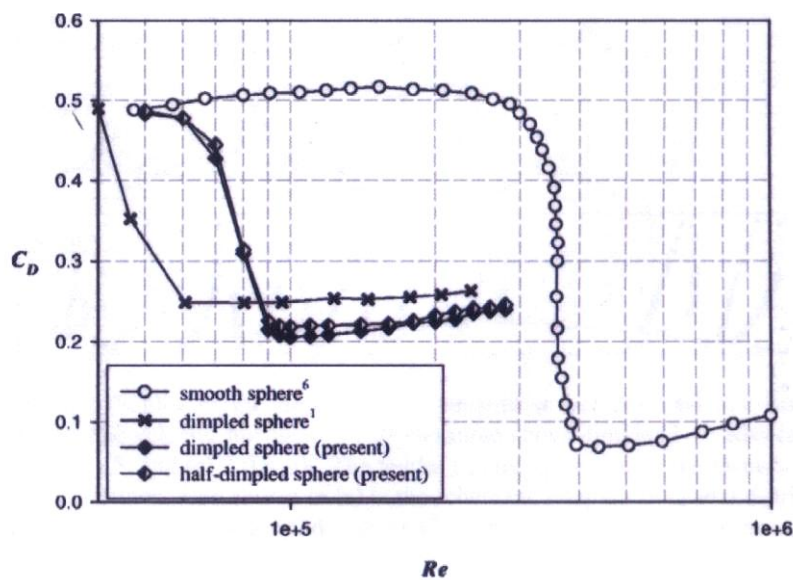


FIG. 1. Variations of the drag coefficient for smooth and dimpled spheres with the Reynolds number, together with the present result from a half-dimpled sphere.

Figure 12 Figure scanned from **Choi et al., 2006**

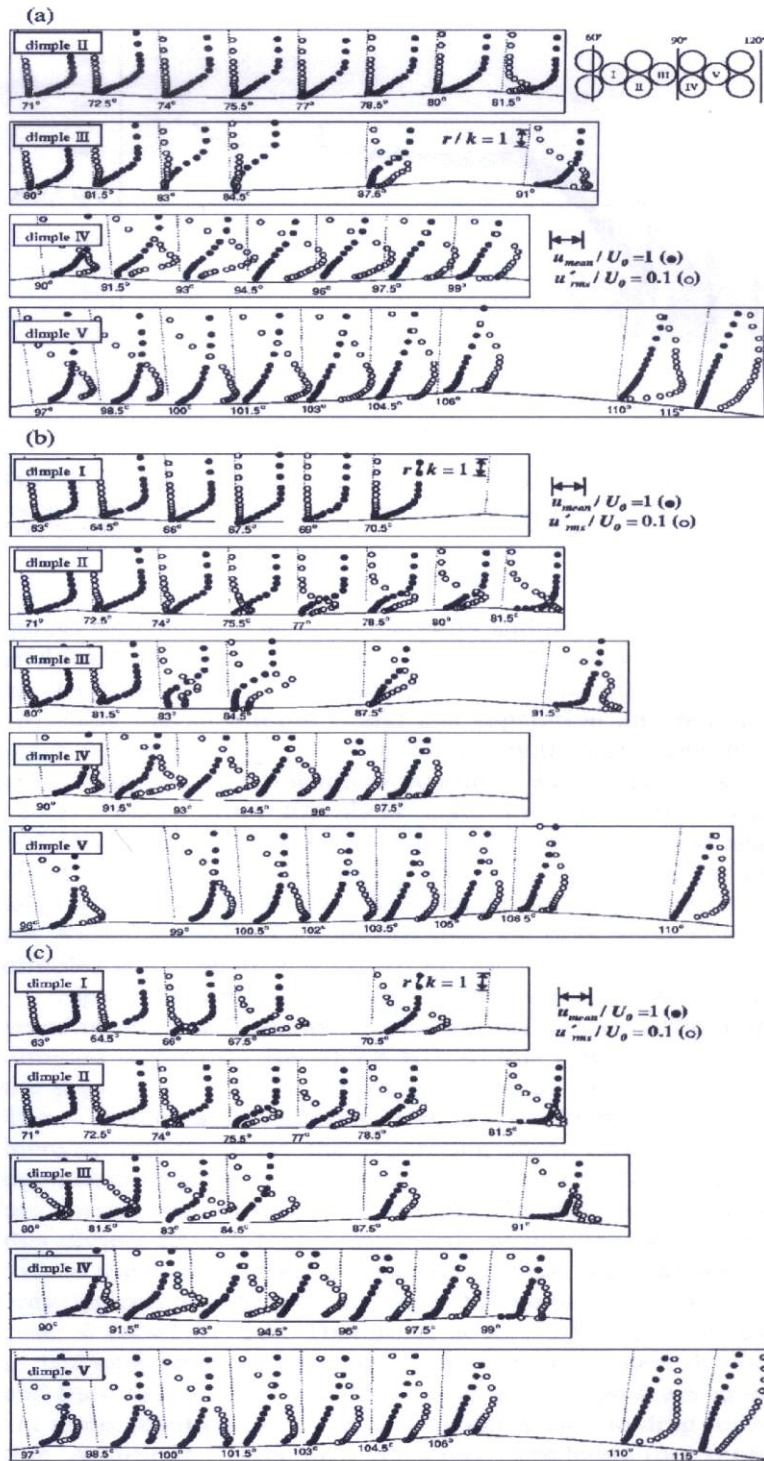


FIG. 3. Profiles of the time-averaged streamwise velocity (●) and rms streamwise velocity fluctuations (○) measured above dimples I–V: $Re =$ (a) 1.0, (b) 1.5, and (c) 2.0×10^5 . The angles in this figure denote the measurement locations. Also shown in (a) is the schematic diagram of spatial distribution of dimples I–V located at $\phi \approx 64^\circ - 106^\circ$ at which hot-wire measurements are conducted.

Figure 13 Figure scanned from Choi et al., 2006

They concluded dimples caused local flow separation as well as triggering the shear layer instability along the shear layer. This increased the turbulent intensity. Because the turbulence was increased, the flow reattached to the surface with a high momentum near the wall and was able to overcome the strong adverse pressure gradient generated on the rear sphere surface. Therefore, dimples delay the flow separation and reduce the drag considerably. Furthermore, they also pointed out reattachment happened at the same location along the flow regardless of the Reynolds number, which maintained a nearly constant drag coefficient at a wide range of Reynolds numbers. Their study also suggested that generating a separation bubble (a closed-loop streamline consisting of separation and reattachment) on a body surface is an important flow-control strategy for reducing the drag on bluff bodies (Figure 14).

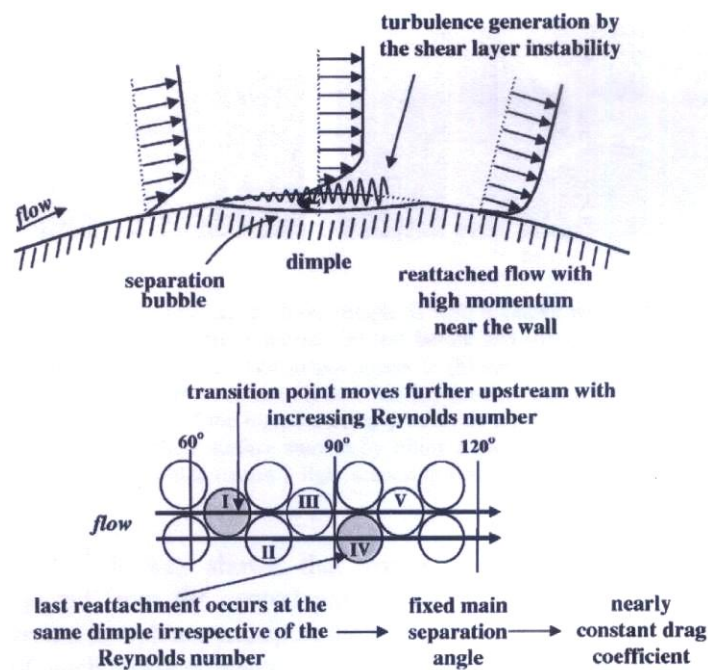


Figure 14 Schematic diagram of drag-reduction mechanism by dimples (Choi et al., 2006)

2.1.6 Forces and Effective Phenomena in the Stream-Wise Direction

In the stream-wise direction, a significant force will be created when the flow approaches the cylinder. This force mainly consists of two components: pressure drag perpendicular to the structure surface, and friction drag caused by the shear stress, which is tangential to the pipe. Figure 15 (Achenbach and Heinecke, 1981, Achenbach, 1968) shows that the relative friction coefficient contributes to the total mean drag coefficient as a function of the Reynolds number. The figure shows that when the Reynolds number is higher than 10^4 , friction drag contributes less than 2~3% of the total drag force. With the assumptions made previously in this project, $Re = 10^4$ is literally in the bottom 1% of the 200 metres, where there is still fluid flow in the stream-wise direction. This means at the upper 99% of the 200 meters, friction drag contributes very little to the total force, which could be neglected. And the total stream-wise force is, therefore, assumed to consist of only one component – pressure drag.

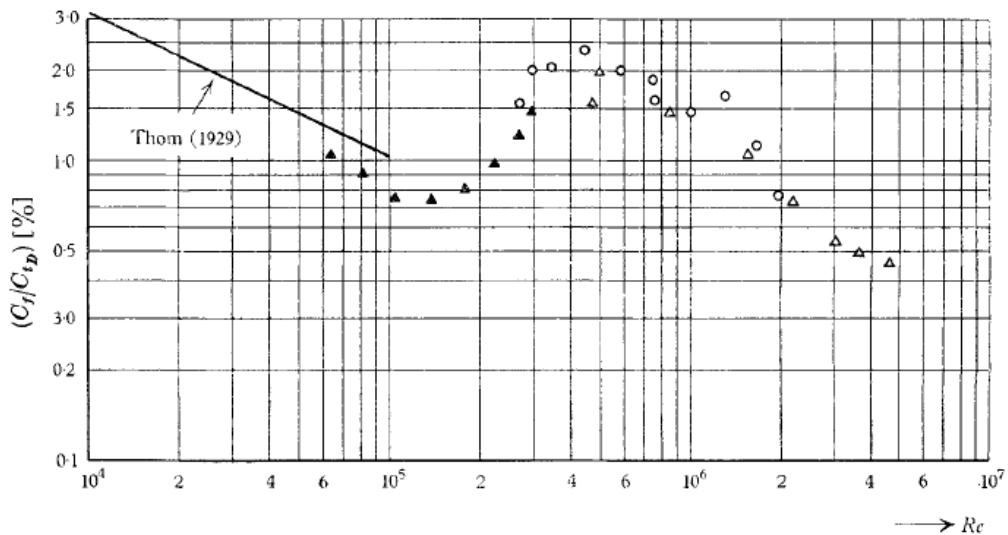


Figure 15 Friction coefficient with respect to total drag coefficient (Achenbach, 1968)

2.2 Definition and Key Parameters of a Dimple

In this project, the definition of a dimple would be some kind of indentation on the circular cylinder surface. To describe a dimple design, there are several key parameters: dimple diameter, dimple depth, distribution of the dimples on the cylinder, and dimple shape. A non-uniform dimple distribution might offer another direction. However, in the real life application of this project, sea water does not always come from a specific direction. It is very likely that ocean current moves in one direction in some seasons and travels in other directions during other times of the year. When there is a hurricane, for example, this would affect the flow that approaches the lifting pile. For this reason, a uniform distribution of dimples on the cylinder surface will avoid this complicated issue and also simplify this study considerably.

2.3 Review of the Open Literature

The effect of surface roughness, concept of boundary layer, and phenomena including boundary layer separation and promotion of the boundary layer transition were discussed in previous sessions. Reduction of stream-wise force on a circular cylinder has attracted research interests for a long time. This project intends to reduce this force by using exterior surface dimples. Apart from this method, various techniques have been developed by other researchers and reported in the open literature. These can offer useful insights and suggest ideas for this project. Some reduction techniques are summarized below:

- a. Circular cylinder with different surface roughness (**Achenbach, 1974**) (mainly applicable in the subcritical region). Mechanism: increasing the roughness will decrease the critical Reynolds number. In some Reynolds number regimes (mainly subcritical), drag coefficient is lower than that for the smooth cylinder.

- b. Dimples on a circular cylinder. Mechanism: dimples promote the transition of the boundary layer from laminar to turbulent, and the turbulent boundary layer can resist the adverse pressure gradient longer. Hence the flow separates later from the cylinder surface and results in a lower stream-wise force. Dimples can be used to control the flow on a sphere as discussed before. **Bearman and Harvey, 1993**, researched circular cylinders and tried to determine whether dimples were able to affect the flow as well as reducing the stream-wise force on cylinders in a similar way as on a sphere. They used parameters found from a typical golf ball, scaled up dimple parameters proportionally, and applied on a circular cylinder. Their experimental results showed that dimples caused a lower critical Reynolds number than the smooth case. However, they did not investigate other dimple configurations in the studies and only conjectured that other dimple designs and arrangements might lead to a bigger drag reduction. Furthermore, no other publications have been found after the paper by **Bearman and Harvey, 1993**, regarding applying dimples on circular cylinders to reduce the stream-wise force.



Figure 16 A circular cylinder with dimples (**Bearman and Harvey, 1993**)

- c. Key parameters for dimple designs include: dimple shape, diameter, depth, and distribution on the surface. Research on the combinations of these parameters for golf ball dimples has attracted a lot of attention because the performance and sales of golf balls relate to these parameters closely. The competition is so severe that 750 US patents were registered from 2001 to 2005, even more than the total number of US patents (500) for other sports during this period. This source of different dimple signs offers a good guidance for the project as well.
- d. A small control cylinder placed in the shear layer near the circular cylinder (**Strykowski and Sreenivasan, 1990, Igarishi and Tsutsui, 1992**). Mechanism: the control cylinder placed in the shear layer near the main cylinder will force the flow to reattach on the test cylinder, causing the flow to separate later from the cylinder surface. As a result, there will be a smaller wake region at the back and smaller stream-wise force as well. However, this method has a problem when applying to the lifting pipe on the mining application. In a real life situation, flow does not always approach the cylinder from the same direction. Therefore, the correct location for the small control cylinder is difficult to determine.

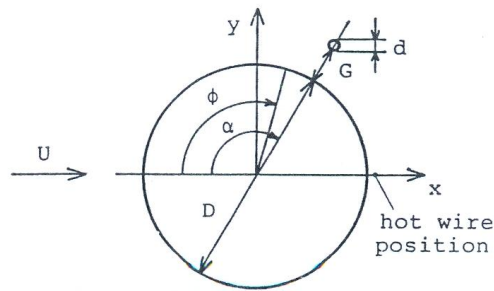


Figure 17 A small cylinder in the shear layer of the test cylinder (**Igarashi and Tsutsui, 1992**)

- e. Setting up a small control cylinder upstream of the main test cylinder (**Tsutsui and Igarashi, 2002**). Mechanism: essentially similar to the mechanism that C_d of a cylinder decreases with increased turbulence in the flow. The small cylinder upstream promotes the transition of the upcoming flow. Hence, the turbulent flow has more forward momentum, which can resist the adverse pressure gradient longer, resulting in a later separation as well as smaller stream-wise force.

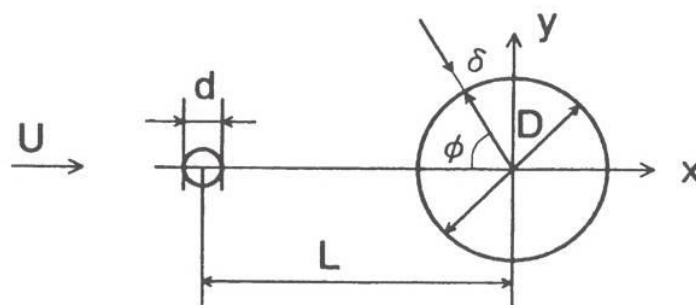


Figure 18 A control cylinder placed upstream of the main cylinder (**Tsutsui and Igarashi, 2002**)

- f. Application of a small flat plate upstream of the cylinder (**Prasad and Williamson, 1997**). Mechanism: similar to putting a control cylinder

upstream. With the best configuration, the pressure coefficient (C_p) curve is nearly symmetrical, which makes the forces on the front and back surfaces of the cylinder very close and causes them to balance out.

- g. Rotation of the cylinder (**Anagnostopoulos, 2002**). Mechanism: making the upper section of the cylinder rotate at the same speed as the flow to eliminate the velocity difference between the fluid and the wall. Hence, the boundary layer does not separate. However, at the bottom half of the cylinder, certain amount of lift force will be produced depending on the speed of rotation.
- h. Boundary layer suction (**Chang, 1970, Chang, 1976**). Mechanism: the flow is sucked artificially in the normal direction of the surface near the flow separation region, which delays the flow from separating.
- i. Boundary layer blowing (**Chang, 1970, Chang, 1976**). Mechanism: the flow is blown in a direction roughly tangential direction to the surface. This adds more energizing momentum to the flow and makes it attach to the surface for longer.
- j. **Owen et al., 2001**, experimentally investigated and measured the drag and vortex-induced vibration (VIV) amplitudes of three objects. They were a circular cylinder, a circular cross-sectional body with a sinuous axis (Figure 19), and a circular cylinder with hemispherical bumps (Figure 20).

The body with a sinuous axis was observed to exhibit suppression of vortex shedding and 47% drag reduction. Drag reduction of about 25% and suppression of vortex shedding have also been recorded for the cylinder with bumps.

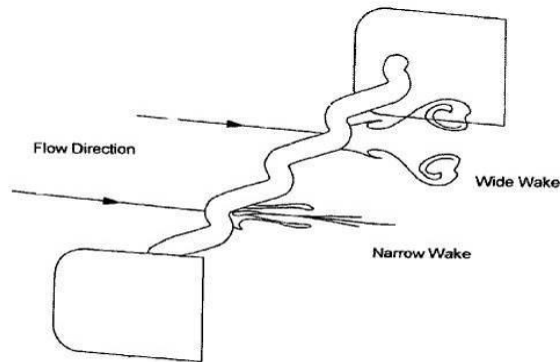


Figure 19 Schematic of circular cylinder with sinuous axis (Owen et al., 2001)

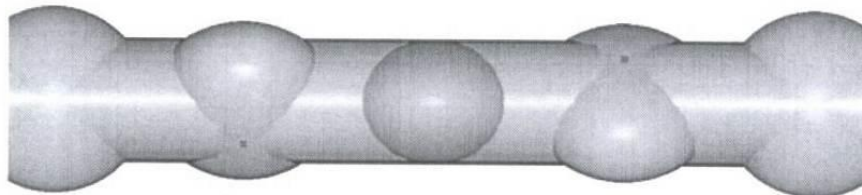


Figure 20 Circular cylinder fitted with surface control bumps (Owen et al., 2001)

- k. Wake splitter plate at the back of the cylinder (Schlichting and Gersten, 2000). Mechanism: this reduces the vortex shedding at the back of the cylinder, and hence decreases the drag.

- l. Streamlining the cylinder at the back. Mechanism: the flow tends to follow the streamlined body and separate later from the object. Drag on the cylinder could be reduced significantly.

- m. **Chung and Whitney, 1993, Chung et al., 1994**, applied a perforated shroud and helical strake cables (Figure 21) around the test cylinder and proposed pipes of about 6,000 metres long for deep sea mining. The data showed encouraging results that these configurations could alleviate the vibrations induced by vortex shedding and possible flow-induced detorquing of the pipe. However, **Bearman and Harvey, 1993, Owen et al. 2001**, argued that perforated shroud was able to reduce the C_d at subcritical region but had a higher value at post-critical regime compared with the smooth cylinder. The key drawback of applying helical cable was that it induced a higher drag force in the stream-wise direction compared with the smooth cylinder especially in the post-critical regime.

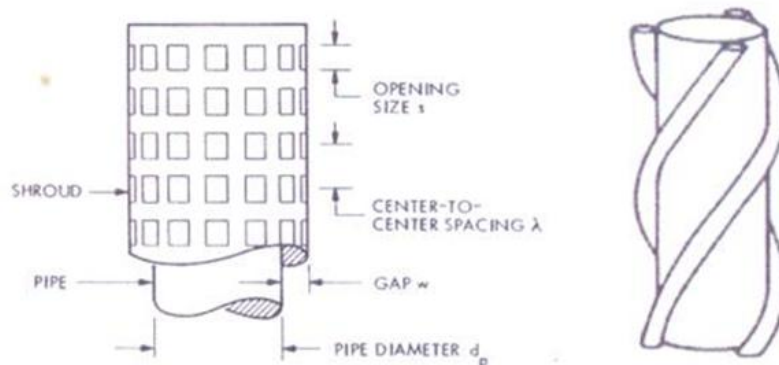


Figure 21 Schematic of perforated shroud and helical cables around the cylinder (**Chung and Whitney, 1993**)

2.4 Summary of Literature Review

To sum up, there are not many publications regarding flow phenomena and stream-wise force reduction by using dimples on circular cylinders. Only a few key papers on dimple effects on circular cylinders were found and summarized in the previous sections. For example, **Nakamura and Tomonari, 1982, Bearman and Harvey, 1976, Bearman and Harvey, 1993, .**

From the analysis of flow physics and literature review in previous sections, it can be preliminarily concluded that applying surface dimples is an important technique for reducing the stream-wise force on cylinders. It could be also seen the main mechanism by which dimples reduce the drag force is the promotion of the boundary layer. The boundary layer would have an earlier transition from laminar to turbulent, which has more forward momentum. Hence it resists the adverse pressure gradient longer and the flow would separate later from the cylinder surface.

After a review on the available literature, publications can be found regarding dimple effects on spheres as well as on circular cylinders. Even though there are some similarities on flow behaviour between these two bluff bodies, better understanding on the circular cylinder is needed to provide answers for the key questions of this project. These questions include: whether dimples can reduce the stream-wise force on cylinders? Is it possible to suggest an optimum dimpled design, which results in greatest force reduction? How do experimental and

computational methods contribute to the research of this project? And can we capture different wake regions for smooth and dimpled cylinders in the flow visualization experiments? These questions will be the main theme throughout this project and as well as this thesis.

Chapter 3

3. Preparations and Experimental Setups

In order to tackle this project, it involved two main approaches. Firstly, conducting experiments in the test facilities and secondly, modelling the flow behaviour with CFD simulations. Experimental method is a traditional and effective way in engineering studies. Because the high Reynolds number could not be matched in the test rig, therefore, the Reynolds number in this project will be scaled down in the test facilities. In the experiments, conditions like inlet flow speed, cross-sectional area can be controlled. As a result, measurements closely reflect the flow behaviour under these settings.

On the other hand, computational simulations served as an alternative research approach in the last decades. It could alter the geometries and then solve the model on a computer without changing anything in the test facilities. Sometimes, it can provide quick answers for a specific modification and guide the design or research. The extensive use of CFD in Formula 1 nowadays is a good example. Besides, flow details within the domain can be shown in post-processing. These are benefits of applying computational methods.

Both methods will be used in this project. Their exact roles will be investigated further as well as their effectiveness. As a result, this project involved two different aspects: experimental and computational studies. For this reason, this chapter will firstly describe all the preparations for experimental setups. And then,

Chapter 4 will discuss different results from both experiments and computational simulations. After that, it will compare and give judgements on the methods and results. All the work related to flow visualization will be described separately in Chapter 5.

3.1 Experimental Objectives and Proposal

In the experiments, it is intended to study different aspects in the test rig, which includes measurements of pressure distribution for smooth and different dimpled cylinders. Furthermore, these experiments will be done under different Reynolds numbers as well.

The total stream-wise force actually consists of the time-mean force and a fluctuating component. In this project, the stream-wise force is a time-average phenomenon that has a long-term action on the lifting pipe and then transmits to other components of the mining system. Fluctuating force is an indicator used to evaluate the turbulence of the flow. To measure it, design of the wind tunnel is different from that used to measure only the time-mean force. For example, high frequency sensors are also required, which are much more expensive than normal low frequency pressure transducers. A transfer function to convert the signals that picked up at the tappings is also needed. Therefore, the long-term and time-mean force is the main contribution to the total force at the current stage of the project.

In order to measure the time-mean force, it is planned to design and construct a test rig and then carry out experiments. This includes designing the wind tunnel

contraction and straight working section, cylinder diameter and cylinder aspect ratio, data acquisition system, PCB circuits, and sensor calibrations will be done as well. Details of these areas will be included in this chapter. After these preparations, experiments can then be conducted. Chapter 4 will also summarize test results of the fan capacity and also tests on a smooth cylinder with different Reynolds numbers. After that, it will describe experiments on different dimpled cylinder designs under various Reynolds numbers, and repeatability of experiments as well. CFD settings and results will also include in Chapter 4 in proper sections. As mentioned earlier, Chapter 5 will describe experiments on flow visualization.

3.2 Design and Construction of Experimental Facilities

3.2.1 Design of the Wind Tunnel and Test Rig

After reviewing some flow phenomena and different techniques reported in the literature, The design and build the experimental test rig was started. Detailed design of different components will be described in this section.

The whole facility had to be constructed from scratch except for an existing blower, which could produce a flow rate of 5 cubic metres per second ($5\text{m}^3/\text{s}$) at 1,460 RPM.

Experiments will be conducted in a low speed wind tunnel, with normal air as the working fluid. Due to fluid dynamic similarity, results obtained from these

experiments are valid as long as the Reynolds numbers match the practical situation, even with different fluid media. This was mentioned when introducing the definition of the Reynolds number in Section 2.1.1.

There is an existing blower with a speed controller in the lab (Figure 22). A convergent section and working section with appropriate dimensions was needed. **Szepessy and Bearman, 1991**, reported that the aspect ratio (length over cylinder diameter, L/D) of the cylinder had a big impact on the time-mean drag coefficient, especially when it was less than 5, due to the 3D effect (as shown in Figure 23). Therefore, the aspect ratio of the cylinders in this project was chosen to be not less than 5 for this reason.



Figure 22 A blower with a convergent section fitted behind

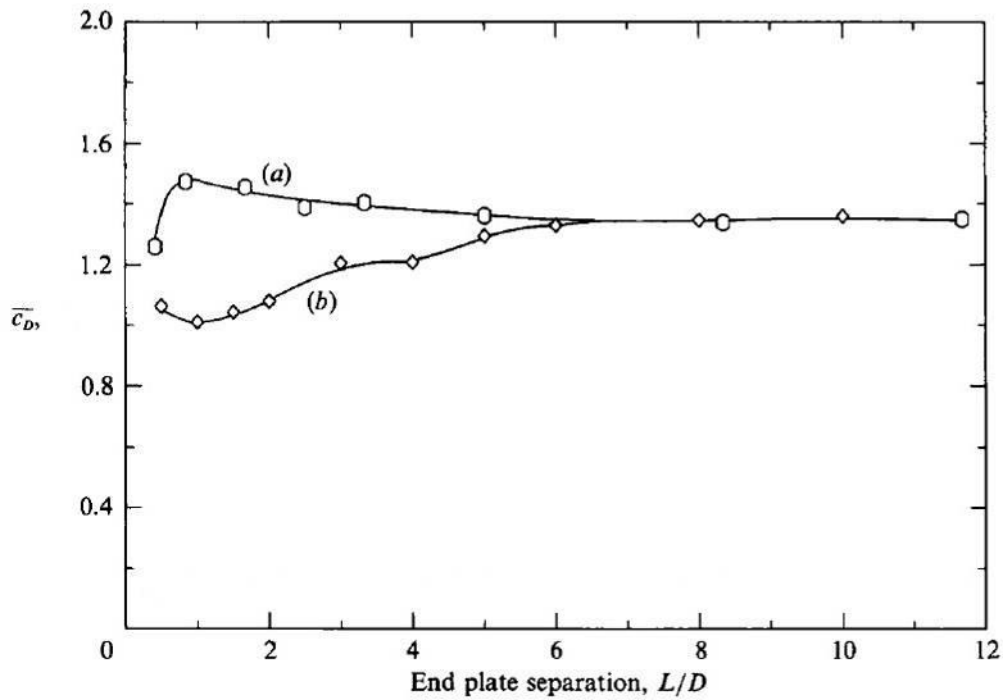


Figure 23 Mean drag coefficient vs cylinder aspect ratio: (a) $Re = 4.3 \times 10^4$, (b) $Re = 1.3 \times 10^6$ (Szepessy and Bearman, 1991)

Figure 24 also shows the whole rig after assembling different sections like: convergent section, straight working section, traverse systems, test cylinders, etc. Details of the design process for various sections will be discussed later. A pitot-static probe mounted on the traverse system, and the distance between the probe and the entrance of the working section is 1200 mm. Distance between the probe and the cylinder axis is 300 mm. Internal dimensions of the working section are: $600 \times 250 \times 4000$ mm (width \times height \times length).

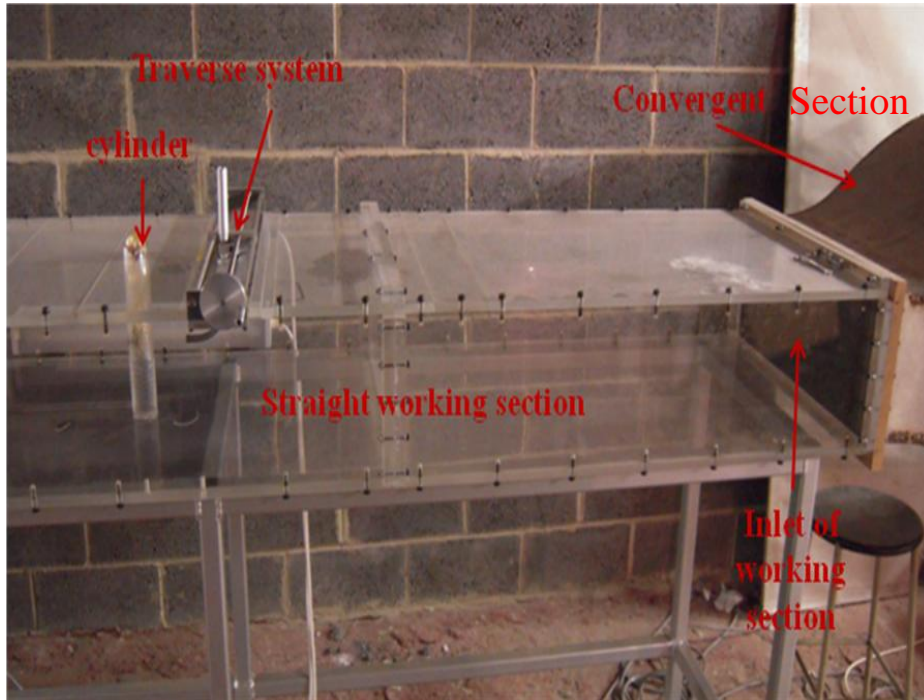


Figure 24 Picture showing the convergent section, straight working section, traverse system, and test cylinder

The first step for designing the rig was the cylinder diameter. As mentioned earlier, the aspect ratio was kept to 5. Different configurations were simulated with CFD methods, and two selected cases of the preliminary designs are shown in Tables 1 and 2.

Cylinder outside diameter	50 mm
Width of wind tunnel	500 mm (10D)
Height of wind tunnel	250 mm
Volume flow rate	5 m ³ /s
Fluid velocity	40 m/s
Velocity pressure	980 Pa
Resultant Reynolds number	1.36 × 10 ⁵

Table 1 Details of design I

Cylinder outside diameter	25 mm
Width of wind tunnel	400 mm (16D)
Height of wind tunnel	250 mm
Volume flow rate	4 m ³ /s
Fluid velocity	40 m/s
Velocity pressure	980 Pa
Resultant Reynolds number	6.81 × 10 ⁴

Table 2 Details of design II

Comparing different designs, the outside diameter of the cylinder was finally chosen to be 50 mm with cylinder height equal to 250mm (aspect ratio = 5). CFD calculations also helped to determine the width of the straight working section. A model with aspect ratio equals to 40 was simulated first and then taken as the reference infinite case. Then different cases for 20D, 15D, 12D, and 10D were modelled computationally and values of pressure coefficient (C_p, taken from the area weighted average values of FLUENT) were compared with the reference infinite value, as shown in Table 3. The 15D and 12D cases were highlighted in the table. Finally, the 12D case was chosen and will be explained in the following sections in more details.

Test case	Percentage difference in static pressure around cylinder
40D	Reference (N/A)
20D	0.43%
15D	3.53%
12D	6.22%
10D	11.29%

Table 3 Comparison of different sectional widths

Next, with values given in Tables 1 and 2, distributions of the pressure coefficient around the cylinder were plotted in MATLAB and shown in Figure 25. Twelve different pressure tappings at various locations (every 10 degrees apart) measuring the static pressure were also superimposed on one of the curves. From the figure, it can be seen that the pressure coefficient on the green curve gave a higher negative pressure at around 80 degrees at the stagnation point. This was due to the boundary layer was less turbulent on the cylinder surface, which resulted in an early separation of the flow. And finally, this caused a higher negative pressure (suction on the back of the cylinder).

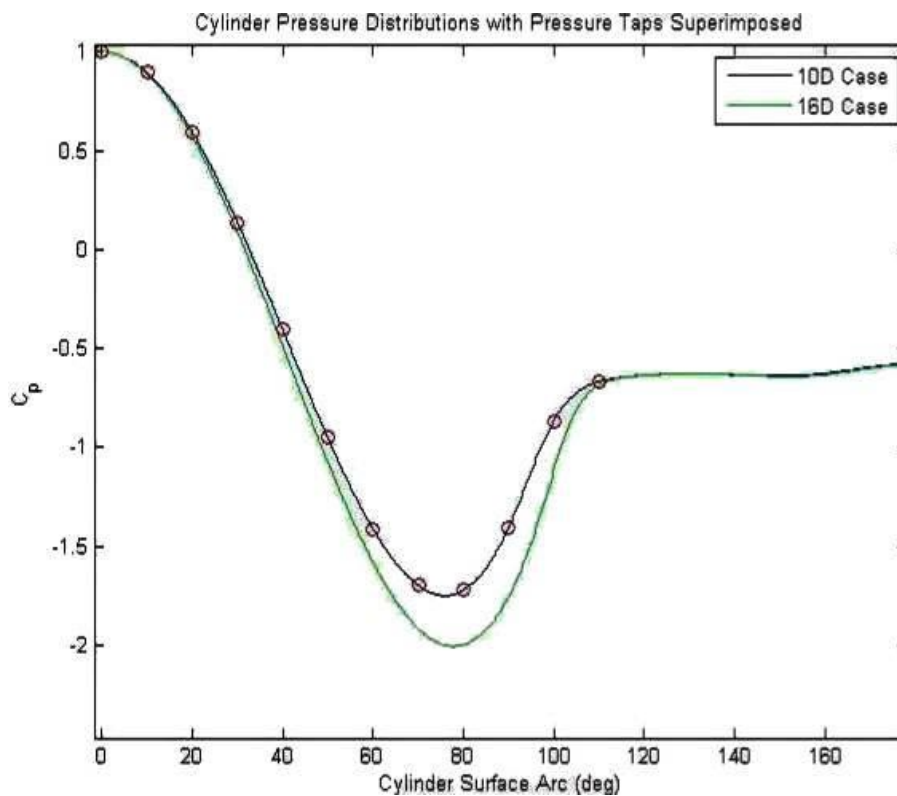


Figure 25 Cp distributions for two different cases

Inside the test section (Figure 26), a pitot-static probe (Figure 27) was installed upstream of the test cylinder and used to measure the static pressure and total pressure. Static pressure measurement was for the velocity calculation of the upstream flow, while the total pressure was for later calculations of the pressure coefficient (Equation 5). In order to prevent this pitot-static probe from disturbing the flow when approaching the cylinder, the pitot-static probe was deliberately set up off the centre line, while the cylinder was installed in the middle of the test section.

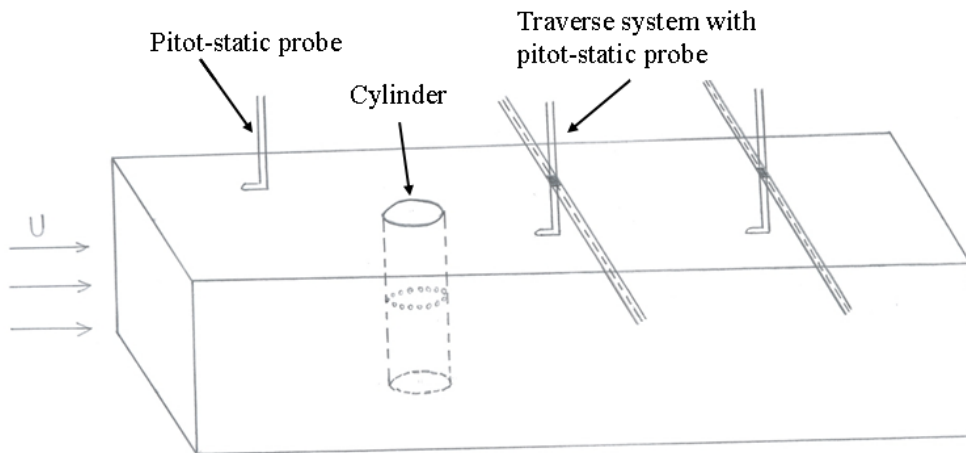


Figure 26 Schematic diagram of the test section

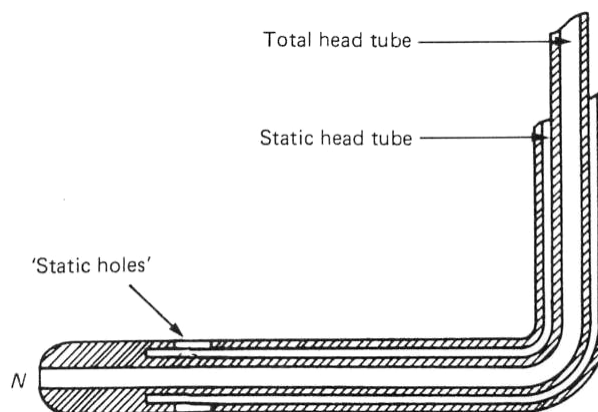


Figure 27 Schematic of a pitot-static probe (Massey, 2005)

$$C_p = \frac{P - P_\infty}{P_{t\infty} - P_\infty} \quad \text{Equation 5}$$

where:

P is the pressure at the cylinder surface

P_∞ is the static pressure in the free stream

$P_{t\infty}$ is the total pressure in the free stream

The 12D case was compared with the 15D case in Table 3. As indicated earlier, the 12D case was finally selected also because it allows a bigger range of flow speed (max: 30 m/s) than the 15D design (max: 20 m/s) and hence more freedom in experiments. Furthermore, the tunnel causes an acceptable 6% difference in static pressure around the cylinder compared with the reference 40D case. Traverse systems were installed at the back of the test cylinder. These traverse systems can move in the Y direction and measure the pressure distributions at the back of the cylinder. Hence, parameters like the boundary of the wake region and values of pressure in various locations could be evaluated.

Finally, as shown in Figure 28, the exit of the blower (800 mm × 800 mm) was connected to a convergent section which converges to 250 mm in height and 600 mm in width. These were also the inside dimensions of the straight working section located right after the convergent section. One honeycomb screen was fitted in the exit of the blower, just before the inlet of the convergent, and another

one was installed in the exit of the convergent section. These can help to reduce the turbulent intensity of the upcoming flow significantly. The cylinder's outside diameter is 50 mm and installed 1500 mm from the inlet of the straight section to its axis.

With this configuration, the aspect ratio of the cylinder is 5, following the guideline of **Szepessy and Bearman, 1991**. Also, from previous analysis, a width of 600 mm equals to 12 times the diameter of the cylinder. This would allow a bigger range of Reynolds numbers in experiments. The maximum speed of the blower can reach 1,500 RPM, which produces a maximum flow velocity of around 30 m/s. With this flow rate, Reynolds number can reach 1×10^5 in the test rig. Also, the Reynolds number can be linearly controlled from $Re = 2 \times 10^4 \sim 1 \times 10^5$. However, the high Reynolds numbers in the real life around $Re = 1 \times 10^6$ could not reach in the experiments. In the test rig, the maximum Reynolds number could only reach around $Re = 1 \times 10^5$ due to restrictions from the equipment. Therefore, experiments will be tested below $Re = 1 \times 10^5$.

Along the circumferential line of the test cylinder at mid-span, a certain number of static pressure tappings were installed, and then the pressure distribution around the whole cylinder at different locations could be obtained. The drag coefficient and drag force per unit length could then be calculated according to Equations 6 and 7. These pressure tappings were connected to pressure transducers and then connected to a data acquisition unit made by National Instruments Ltd.

$$Cd = \int_0^{2\pi} Cp(\theta)\cos(\theta)d\theta \quad \text{Equation 6}$$

$$Drag = 0.5\rho V^2 SCd \quad \text{Equation 7}$$

Some specifications of the data acquisition unit (model: NI USB-6218) are summarized in the following Table 4

Instrument Name	NI USB-6218
Single-Ended Channels	32
Differential Channels	16
Resolution	16 bits
Sample Rate	250 kS/s
Maximum Voltage Range	-10V, 10V
Maximum Voltage Range Accuracy	2.69mV
Maximum Voltage Range Sensitivity	91.6μV
Minimum Voltage Range	-200mV, 200mV
Minimum Voltage Range Accuracy	0.088mV
Minimum Voltage Range Sensitivity	4.8 μV

Table 4 Specifications of the data acquisition unit (model: NI USB-6218)

The time-mean average pressure was the parameter measured in the experiments. It would be derived from measurements by the pressure transducers. The output signals would then pass to the data acquisition unit before logging the values in the LabView program.



Figure 28 Picture of the blower, convergent, and straight working section

Equipment involved in the test rig:

- Straight working section: inner dimensions 250 mm × 600 mm
- Test cylinder: 50 mm × 250 mm
- Pitot-static probe: from United Sensor, USA
- Pressure transducer: from Sensortech, Germany
- Data acquisition unit: from National Instruments, UK
- Traverse system: made in the workshop, Oxford University
- Tubes used to connect the pressure tapings, diameter 1.6 mm
- Software package: LabView by National Instruments Ltd, codes written by the author

3.2.2 Design of the PCB Circuits and Sensor Calibrations

Next, several pressure transducers were calibrated by a pressure calibrator and multimeter as shown in Figure 29. Some specifications of the pressure transducers are given in Table 5. Good co-relationships between the input pressure and output voltage (Table 6) were found. All R^2 values were close to 1, which indicated that they could be used to measure other experiments very well. One of these sensors, the one with smallest range, also gave a very linear relationship and good R^2 value (Figure 30).

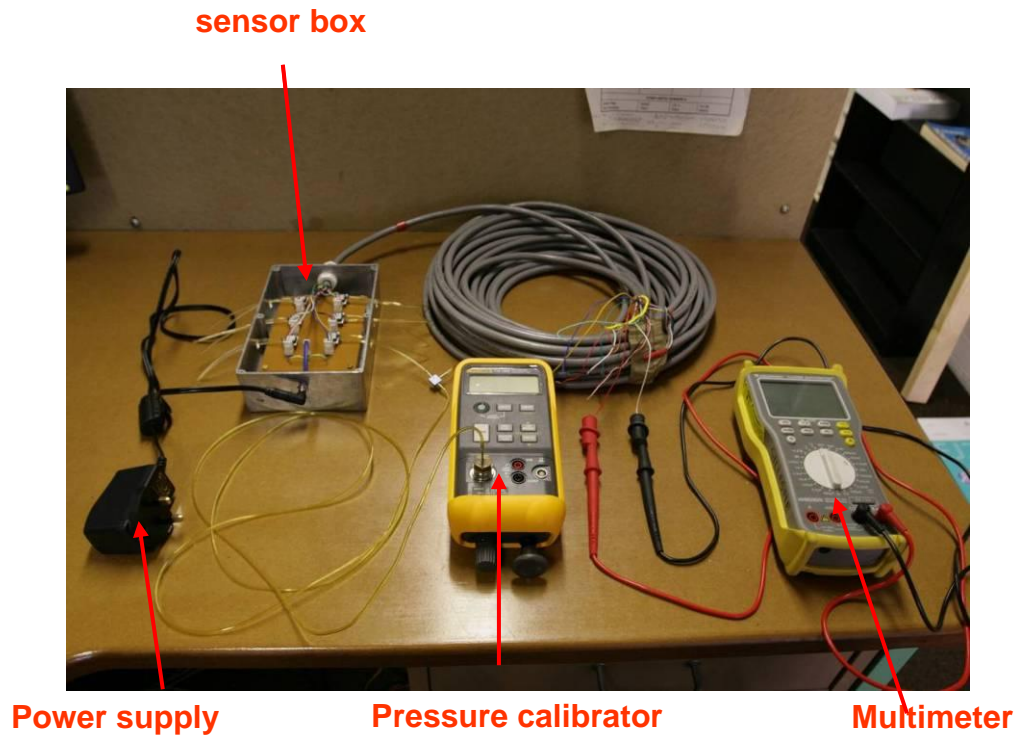


Figure 29 Equipment used to calibrate the pressure transducers

Sensor Type	Sensortechcnics HCLA Series
Supply Voltage	4.5 ~ 5.5V
Operating Pressure	0 ~ ±2.5mbar or 0 ~ ±12.5mbar
Output Signal	2.25±2V
Zero Pressure Offset	2.15 ~ 2.35V

Table 5 Specifications of the pressure transducers

Sensor	Range	Calibration Equation	R ² Value
1	+/- 25 mbar	Y = 0.0819x + 2.3145	1.0002
2	+/- 25 mbar	Y = 0.0820x + 2.3124	0.9997
3	+/- 2.5 mbar	Y = 0.8141x + 2.3661	0.9995
4	+/- 12.5 mbar	Y = 0.1637x + 2.3219	1.0001
5	+/- 12.5 mbar	Y = 0.1642x + 2.3085	1.0002
6	+/- 12.5 mbar	Y = 0.1634x + 2.3067	1.0001

Table 6 Calibration data for different pressure transducers

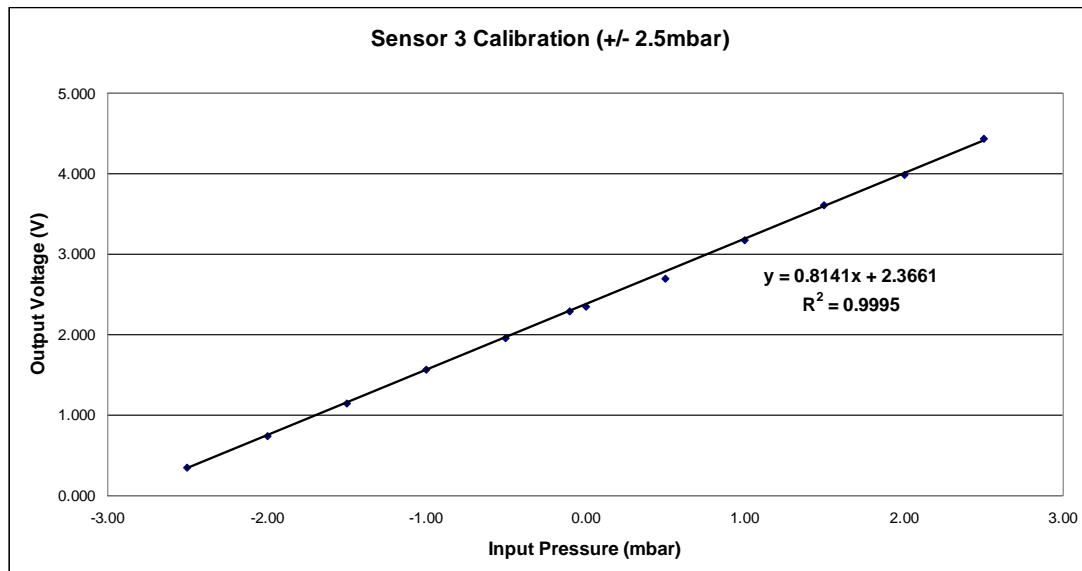


Figure 30 Calibration graph for +/- 2.5 mbar pressure transducer

Then these pressure transducers were soldered on PCB boards along with some pins and capacitors. The circuits were powered by 5.0 volt adapters and the other ends of the circuits go to the data acquisition unit manufactured by National Instruments Ltd, which picked up the voltage data and display in LabView codes. And these codes were written by the author. Whether or not to pick up a specific signal from a transducer could be easily controlled by these circuits as well. Capacitors were used to smooth the DC power input and reduced the noise. After soldering all the components on the PCB board, a multimeter was used to check the connectivity and ensured different rows on the PCB boards were not connected together by mistake.

3.2.2 Design of the Data Acquisition Unit

After finishing the circuit, the next task was to write the LabView code. An example of the code is attached in Appendix I. This code set the sampling rate to 1,000Hz, and takes 5,000 samples (sampling time = 5 seconds). It picked up two output signals from two pressure transducers. More channels could be easily added to the acquisition system. In this system, the first channel was for the static pressure on the cylinder, while the other one was for the total pressure up-stream. Time-mean average pressures as well as standard deviations were reported. This code was capable of picking up the voltage signals from different sensors. Furthermore, some other parameters, e.g., sampling rate, number of samples, and more sensor channels could be defined by the user in this code as well. By using this code, the output voltages as well as standard deviations could then be reported.

3.2.3 Performance of the Fan

After these preparations, the blower was ready to switch on and conduct some experiments in the wind tunnel. The fan RPM was firstly plotted against different Reynolds numbers as shown in Figure 31.

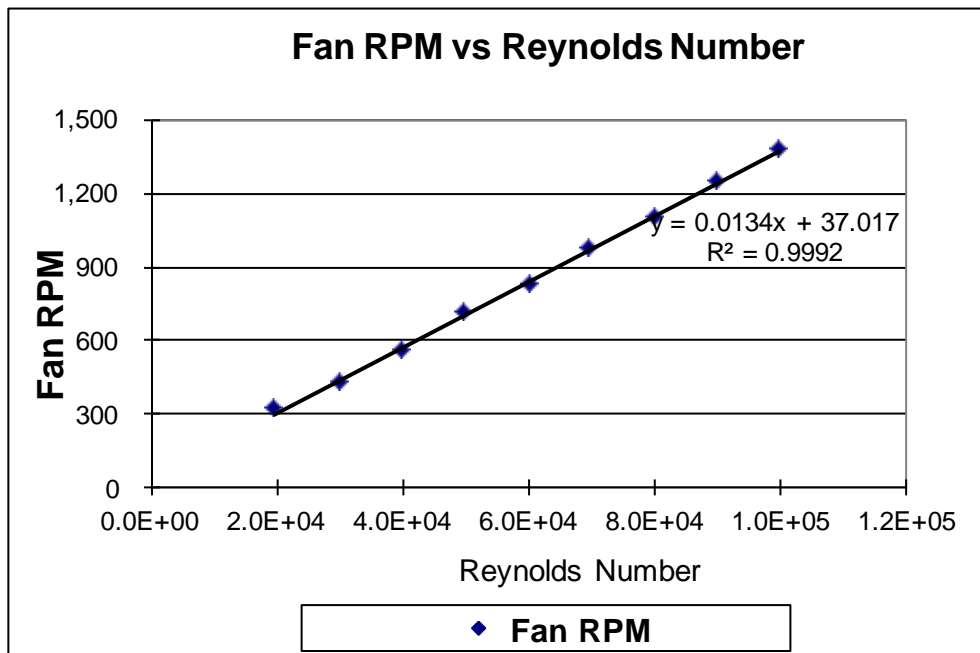


Figure 31 Graph showing a linear relation between fan speed and Re

To sum up, from the preparations discussed in this section, high repeatability of experiments could be seen. Calibrations of the pressure transducers were also good. Outputs of the blower showed very good linear relationships as well. R^2 values of the calibrations and standard deviations of the measurements were of high quality. These results increased the confidence of the experiments, as well as demonstrating the high repeatability, which was desirable.

Chapter 4

4. Results and Discussion

After the design, construction, and different preparations on the experimental facilities, the wind tunnel was ready to run. This chapter will start with experiments on the smooth cylinder, and then moves to dimpled cylinders with different designs and also discussions. The repeatability of experiments will also be investigated as well as discussing the CFD settings and results in suitable sections.

4.1 Results and Discussion on the Smooth Cylinder

4.1.1 Design of the Smooth Cylinder and Measurements

Due to the height of the test cylinder (250 mm), it would be very difficult to put in the pressure tappings if the cylinder was made in one long piece. Therefore, the test cylinder was broken down into a solid section and a hollow part as shown in Figure 32. Thirty-six pressure tappings around the smooth cylinder would give a good enough resolution of the pressure distribution. This was a better approach than having less tappings and rotating the cylinder during the experiments. Because the gaps between the cylinder and the top and bottom walls were very tight and sealed very well, it was not easy to rotate the cylinder precisely. Also, the tappings were put in carefully and fixed on the cylinder to make sure the

tapping inlets were in line with the cylinder outer surface as much as possible (Figure 33).



Figure 32 Smooth cylinder fitted with 36 pressure tapings

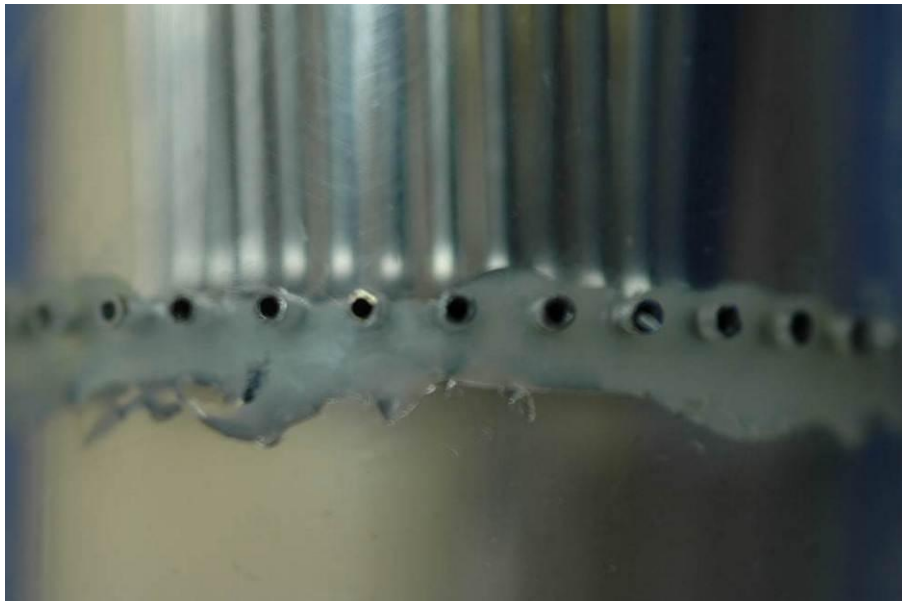


Figure 33 Close up view of the pressure tapings on the smooth cylinder

There were 36 pressure tappings in the mid-span of the smooth cylinder as shown in Figure 32. The gap between each two tappings was 10 degrees. To measure the pressure on each tapping, the sampling rate was set to 1,000Hz, and it took a period of 5 seconds. Therefore, there were 5,000 samples in the measurements for the first test. Before going further, the repeatability of the experiment was also examined. The second test kept the same conditions, i.e., sampling rate of 1,000Hz and measured data for 5 seconds. The third test kept the same sampling rate but extended the sampling period to 1 minute. These three sets of data agreed very well and plotted together in Figure 34. Besides, the standard deviations were found to be very small compared with the values of the output signals and close to zero. This indicated that the measurement errors were reasonably small. A set of the raw data is attached in Appendix II.

Next, a series of experiments were carried out for different Reynolds numbers. These varied from 0.2 to 1×10^5 , with an increment of 0.1×10^5 . The Reynolds number could not set to very low because the blower required a minimum RPM to ensure it worked properly. Besides, pressure transducers used could not give small enough resolutions when conducting low Reynolds number experiments. These results were plotted in Figure 35 and Figure 36.

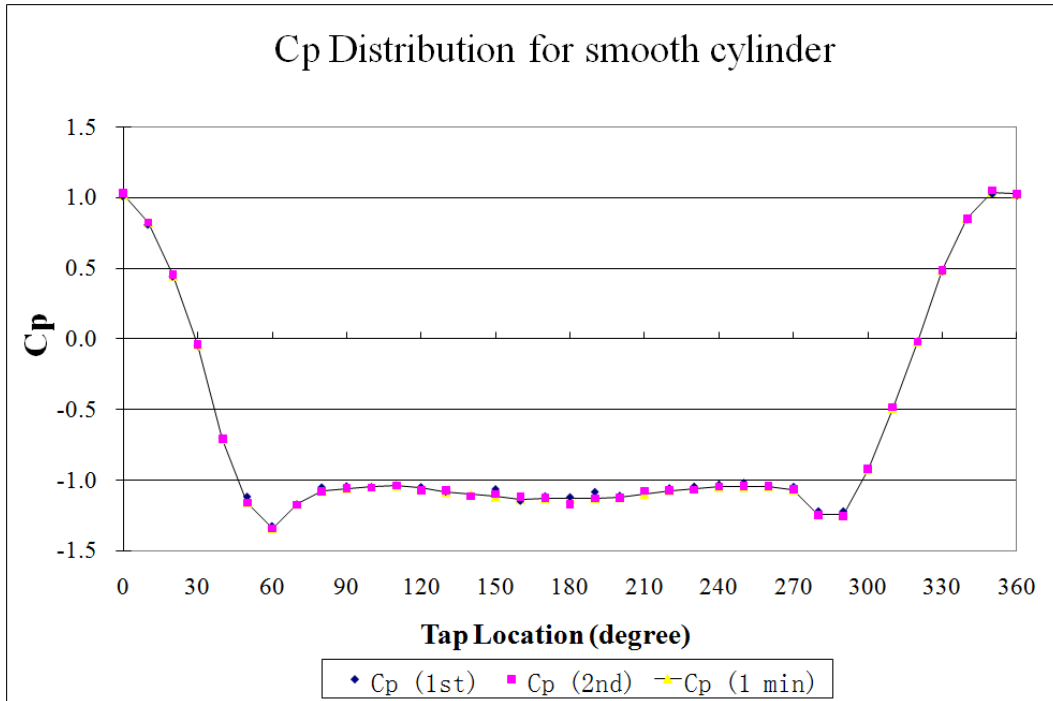


Figure 34 Three different cases for measuring the pressure distribution around the cylinder

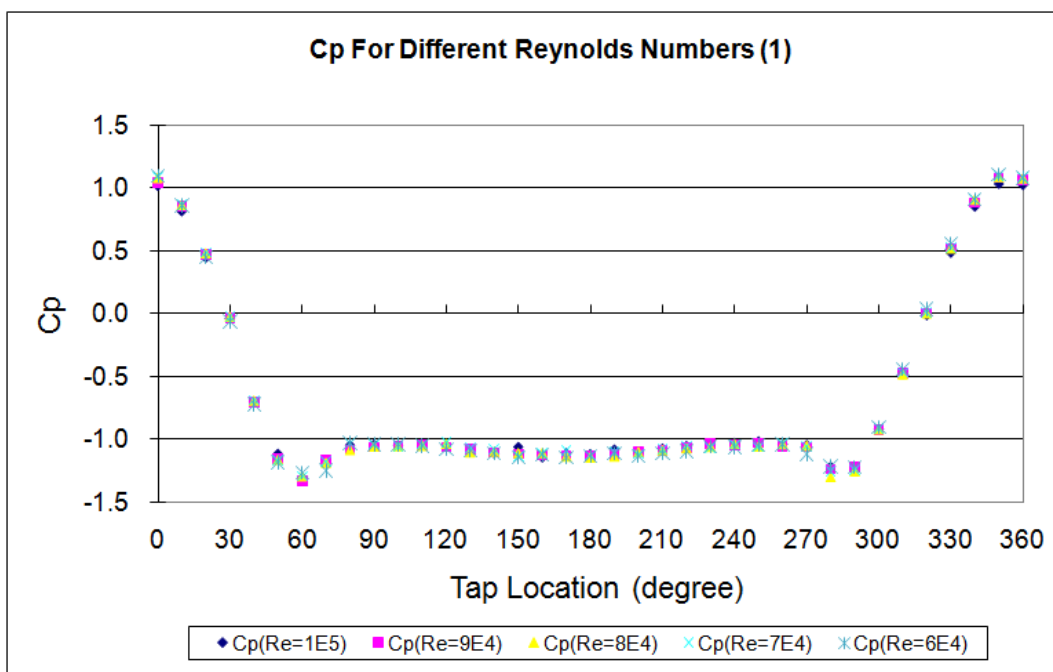


Figure 35 Pressure coefficient plot against different Reynolds numbers (part one)

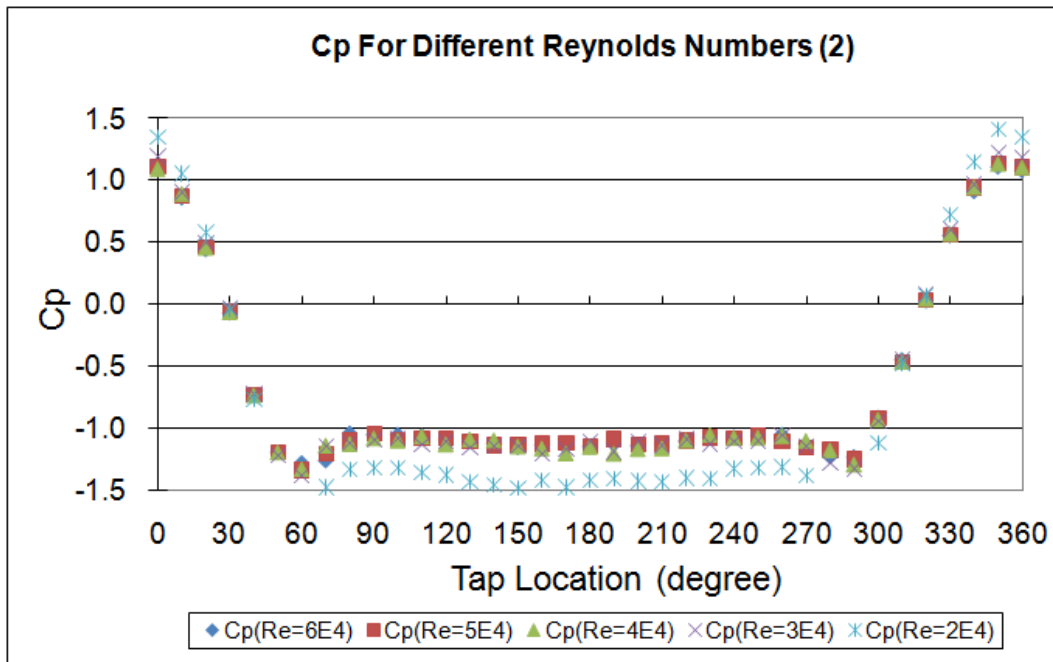


Figure 36 Pressure coefficient plot against different Reynolds numbers (part two)

From Figure 35 and Figure 36, we can see that the pressure coefficients were distributed quite close together for different Reynolds numbers, except for the case when the Reynolds number dropped down to 0.2×10^5 . It had a higher negative value of C_p , which indicated that the drag coefficient was higher at this specific Reynolds number. This higher negative value of C_p implied the earlier separation of the flow from the cylinder surface, which in turn resulted in a higher pressure drag. On the other hand, as we know, a lower Reynolds number corresponds to a higher drag coefficient on the smoother cylinder because the flow is closer to the laminar separation side.

The author would also like to make another comment on Figure 34 to Figure 36. In some of the cases, it could be seen that the C_p values are higher than 1, which is not expected in the ideal case. However, the experiments are not ideal, and C_p values were calculated from Equation 5. $C_p > 1$ indicates the determination of total pressure in the free stream tend to a bit low. And the total pressure was measured by the pitot probe as discussed before. Furthermore, this pitot probe was not located at the centre line in the traverse Y direction. Therefore, some measurement error was reasonable.

4.2 CFD Modelling of a Smooth Cylinder

After the experimental tests on the smooth cylinder, a series of tests by computational methods were then carried out. The main simulation software involved were FLUENT, Gambit, FieldView. Geometries were created and meshed in Gambit, and then FLUENT was used as the solver. FieldView, a third-party software, was sometimes used to produce better post-processing images, or videos than the basic functionalities in FLUENT.

Initially, simulations were run on a smooth cylinder. The cylinder is facing a 1m/s upstream. In this case, $Re = 150$, and the flow is laminar. Therefore, no turbulent model was applied. There are about 11,000 cells in the domain. It was a 2D unsteady simulation. The time step size was 0.2 second. Here is some more details on choosing the time step size.

The Strouhal number for flow past cylinder is roughly 0.2. In order to capture the shedding correctly, at least 20 to 25 time steps in one shedding cycle are needed.

$$Sr = 0.2 = \frac{f \times D}{U}$$

In this case,

$$D = 1, U = 1$$

Therefore,

$$f = 0.2$$

Cycle time,

$$t = \frac{1}{f} = \frac{1}{0.2} = 5 \text{ sec}$$

Therefore,

$$\text{time - step - size} = \frac{5}{25} = 0.2 \text{ sec}$$

The periodic vortex shedding was demonstrated, and the lift coefficient versus flow time was plotted in Figure 37. As a result, the plot history is quite smooth.

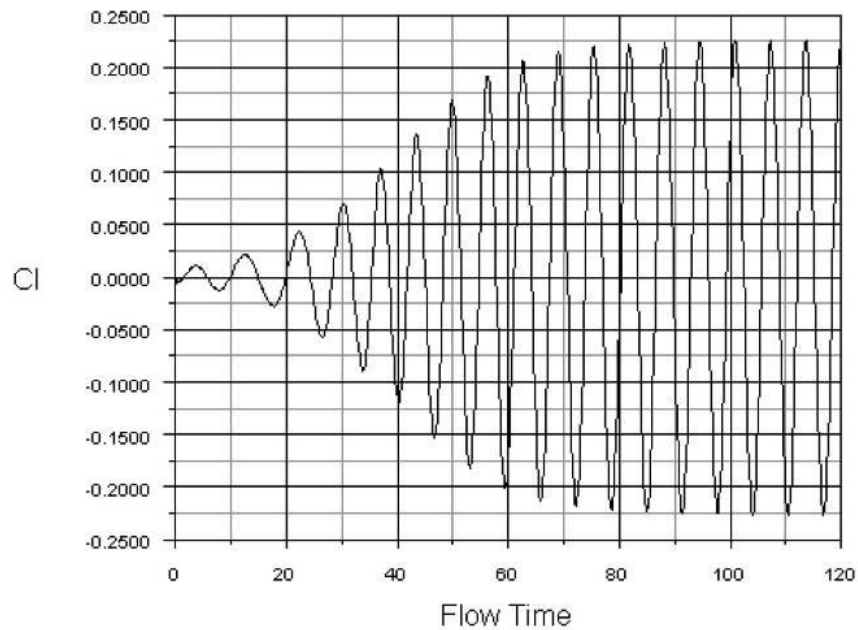


Figure 37 Lift coefficient vs flow time of a smooth cylinder in laminar flow

Next, a domain closely representing the wind tunnel was created in Gambit and solved in Fluent in order to obtain the pressure distribution on the smooth cylinder. This CFD model matched the diameter of the cylinder (50mm). The width was 600 mm, same as the wind tunnel inside diameter. Suitable values of the inlet and outlet of the domain were chosen that would not affect the up-coming flow and create back flow. And the decision was made according to the initial plot of the static pressure distribution inside the domain. The section where the pressure contour didn't change much was omitted and therefore a smaller domain, as shown in Figure 38, was selected. Figure 38 showed this CFD domain. It was a 2D model and the cylinder was surrounded by quadrilateral cells in the boundary layers as shown in Figure 39. Far away from the boundary of the cylinder, the size of the quadrilateral cells increased in order to save the CPU time. There were about 110K cells inside the domain.



Figure 38 CFD domain for smooth cylinder simulation

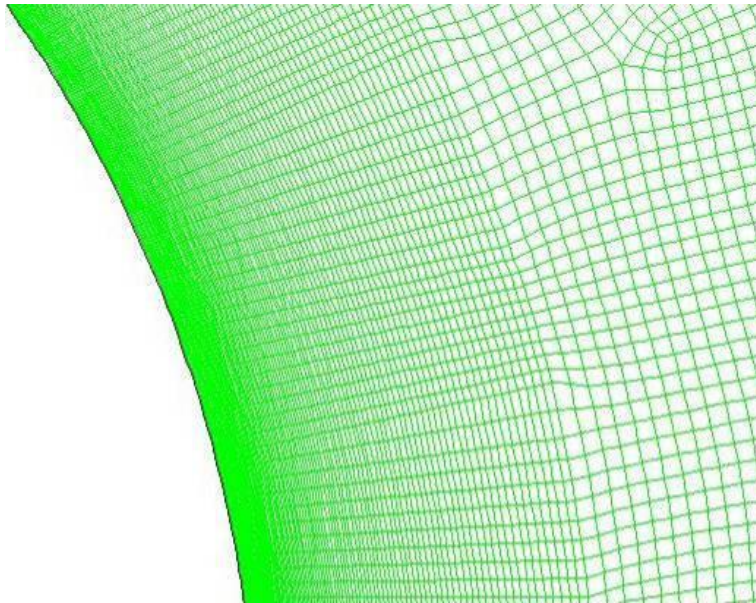


Figure 39 Schematics of the mesh around the smooth cylinder

The computational model with the maximum Reynolds number in the experiments ($Re = 1 \times 10^5$), was initially tried on a Realizable K-Epsilon (RKE) turbulent model with enhanced wall treatment. Vortex shedding behind the cylinder was

shown in Figure 40. It was clear that the vortices started to form right behind the cylinder and passed downwards along the flow direction (flow came from left hand side). At the same time, the width of the vortex region also increased in the stream-wise location.

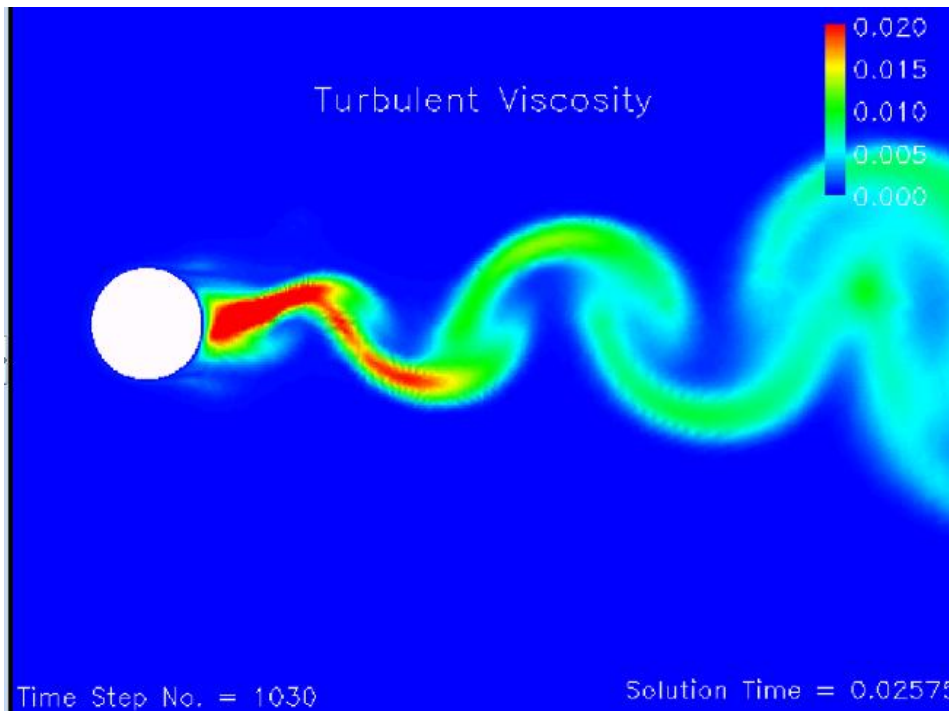


Figure 40 Vortex shedding behind a smooth cylinder

However, with the RKE turbulent model, the drag coefficient (C_d) was found to be around 0.5~0.6. It neither agreed well with the value of about 1.2 for a smooth cylinder at this Reynolds number reported in the literature nor was it close to the experimental data. After careful consideration, it was believed that the flow was close to the transition region at $Re = 1 \times 10^5$, as shown in Figure 3. Transition normally starts at around $Re = 2\sim 3 \times 10^5$, and this is a region difficult to examine. Hence, forcing the model with some kinds of turbulent model may not be

appropriate. As a result, it was decided to apply the laminar model for the later simulations. The laminar model could still pick up the turbulent behaviour in the flow under certain conditions, and will be discussed in more detail later in the section when comes to dimpled cylinders.

Next, two sets of pressure coefficient data, one from experiments and the other from CFD simulation, were plotted together in Figure 41. In this figure, these two curves were very close together. From the integration method in Equation 7, the Cd value obtained from the experiment was 1.152, and that from CFD calculations was 1.164. There was a small difference of 1.04% between these two values. Because the small difference between these two values, it would add more confidence on the values.

Another point that can be seen in Figure 41 is that the minimum pressure coefficient did not go beyond -1.5 , which seems do not agree with what those plotted in some fluid mechanics references, for example, Figure 42. This was because with the experimental and simulation conditions in these conditions, the Reynolds number of the flow was at 1×10^5 , where the boundary layer was still laminar before transition to turbulent boundary layer. Therefore, it agreed with the laminar separation curve in Figure 42, and if compared with Figure 3, the well accepted Cd around these Reynolds numbers is 1.2. There was only a difference about 4.2%. So the results were actually consistent.

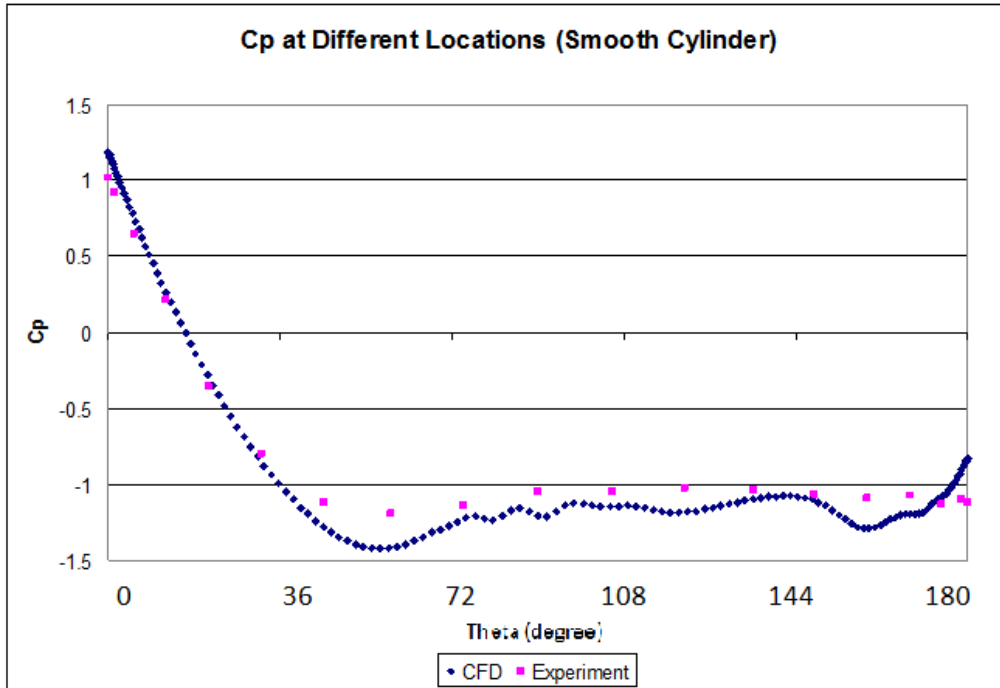


Figure 41 Pressure coefficients from experiment and CFD prediction at 1×10^5

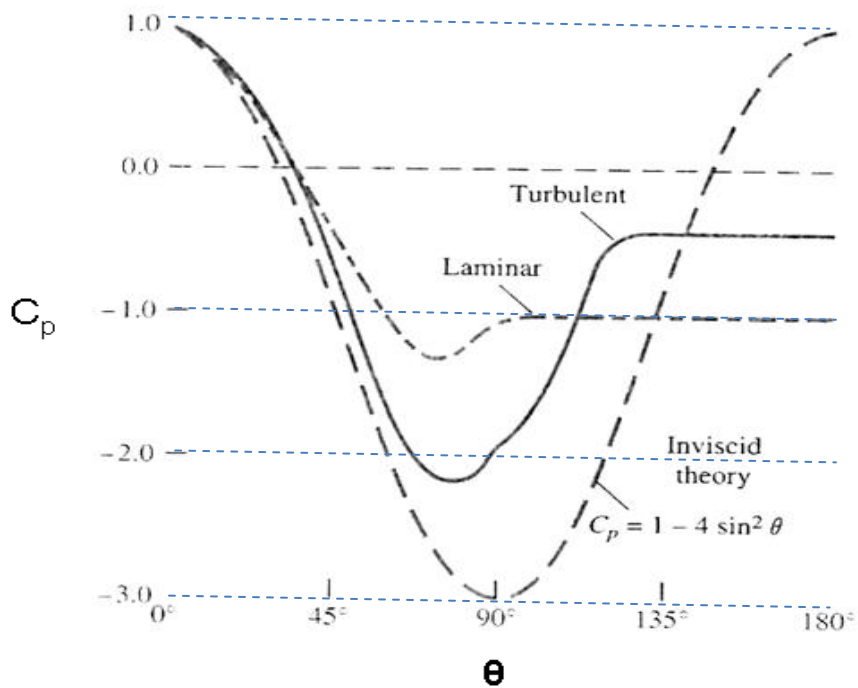


Figure 42 C_p around a cylinder for laminar BL, turbulent BL, and theoretical prediction (Massey, 2005)

Nevertheless, there were still a number of reasons for the error. For example, in some other experiments, researches may have been conducted in very well controlled environments and the cylinders may also have been installed in a much bigger wind tunnel with bigger cross sectional area compared with the relatively confined and not ideal environment in the current experimental rig. Also, temperature, moisture, and other factors could also slightly affect the flow density and up-coming flow velocity and hence the dynamic head when conducted the experiments at different time and different days. Some error are unavoidable. However, there is about 4% difference and it is well acceptable in typical engineering problems.

4.3 Results and Discussion on Different Dimpled Cylinders

When trying to design the dimple pattern for the first dimpled cylinder, it was decided to adopt the typical pattern from a golf ball. In the research paper by **Bearman and Harvey, 1993**, it showed the experimental results and plotted the C_d against Reynolds numbers as in Figure 43. In this figure, we can see that in the range where we were able to conduct the experiments in the wind tunnel, that is, $Re = 0.2 \times 10^5$ to $Re = 1 \times 10^5$, their dimpled cylinder could indeed reduce the C_d significantly. From $Re = 4 \times 10^4$, C_d started to fall from 1.2 to a minimum value about 0.5 at around $Re = 1 \times 10^5$. A maximum reduction of around 50% of C_d was reported.

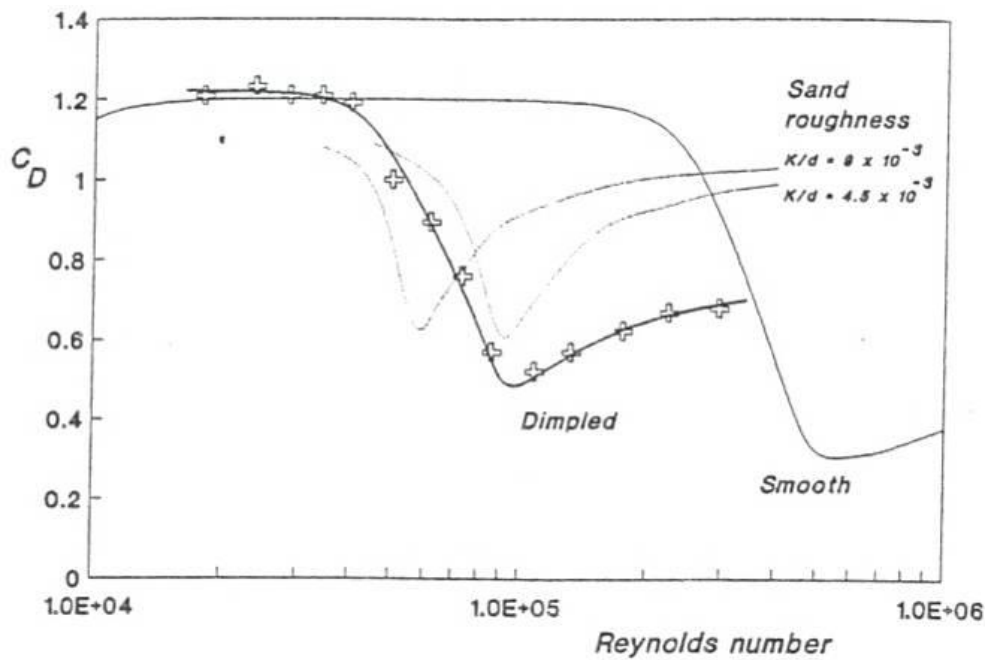


Figure 43 Variation of C_d with Re for smooth, sand-roughened, and dimpled cylinders (**Bearman and Harvey, 1993**)

The dimples used by **Bearman and Harvey, 1993**, were scaled from a typical golf ball. Therefore, the first dimpled cylinder in our studies followed the similar philosophy. There were 20 dimples around the cylinder with dimple depth equalled to 0.45 mm. It was used to test inside the wind tunnel and to measure how pressure was distributed around it; then the C_d was calculated before comparing with other results. This design was shown in Figure 44. In this design, 20 dimples were equally distributed around the circumferential direction of the cylinder. In the axial direction, different dimples were lined up along the axis; no staggered patterns were involved in this design.

Dimples were made/cut by using a spherical cutter with diameter of 20 mm ($r = 10$ mm). The dimple depth was 0.45 mm and the depth ratio (dimple depth/cylinder diameter) was 0.009. Because the dimples were cut by a spherical ball cutter on the cylindrical surface, actual shapes of the dimples on the cylinder surface would be elliptical as a result and the dimensions were roughly 5×6 mm.



Figure 44 The dimpled cylinder specimen

Next, experiments were conducted on this dimpled cylinder under the same Reynolds numbers as those on the smooth cylinder. Details of the measurements remained unchanged as well. Figure 45 showed a comparison of the drag coefficient against different Reynolds numbers for the smooth and the dimpled cylinder. From this figure, it could be seen that under the same Reynolds numbers, this dimpled cylinder could indeed reduce the C_d significantly. The percentage of reduction depended on different Reynolds numbers ranging from 13% to 48%.

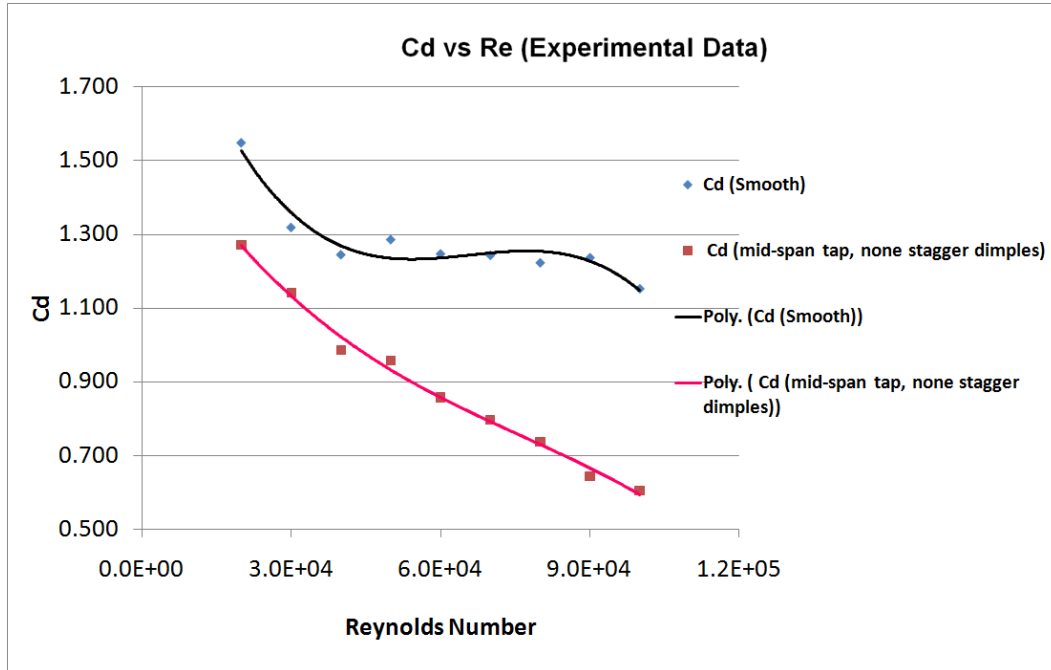


Figure 45 Cd vs Re for smooth cylinder and mid-span tapings, none stagger dimpled cylinder

For the dimpled cylinder, pressure tapings were only installed on the mid-span of the cylinder, therefore, measurements were only done at the mid-span of the test cylinder. In order to obtain the drag coefficient along the axial direction of the cylinder, dimples along the vertical Z direction were also needed. Even though the Cd was not measured along the whole length, a certain length in the axial direction would be essential.

In order to measure the pressure both in the mid-span and along the axial directions, a 5×5 matrix for the pressure tapings was created around a dimple located in the mid-span for the “maxtrix-type tapings, none stagger dimples” cylinder as shown in Figure 46. A close up view of the tapping matrix was also shown in Figure 47.

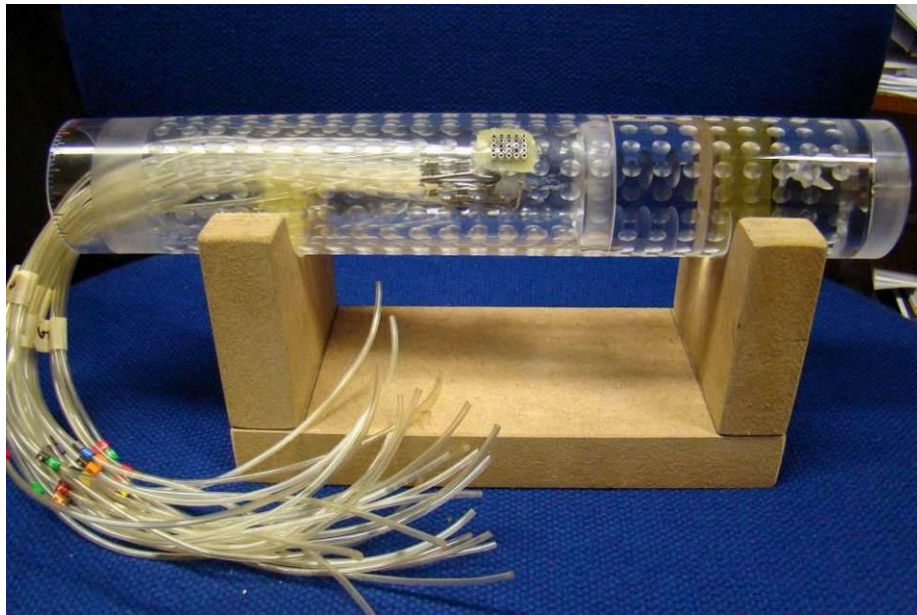


Figure 46 “matrix-type tappings, none stagger dimples”cylinder with pressure tapping



matrix

Figure 47 Close up view of the pressure tapping matrix around one dimple

However, before making the “maxtrix-type tappings, none stagger dimples” dimpled cylinder as shown in Figure 41, some sellotape was used to stick on the dimpled cylinder as shown in Figure 48. This was because putting dimples on the whole cylinder required a lot of technician time. Therefore, a small experiment was done and put some sellotape on both ends of the dimpled cylinder. It was intended to see with only a few rows of dimple around the mid-span of the cylinder, but leave other sections smooth, can whether give acceptable drag coefficient. And if it could, this method can save a lot of technician time and also reduce the cost for making cylinders for experiments. As shown in Figure 48, there were three more rows of dimples on each side of the mid-span of the cylinder. Therefore, there were seven rows of dimples in total including one row in the mid-span.

Experiments were then conducted on this modified dimpled cylinder (with sellotape) and the results were compared with the results obtained previously. However, it was found that the difference between the original and modified dimpled cylinder (with sellotape) was too big. For example, at $Re = 1 \times 10^5$, $Cd = 0.82$ for the modified cylinder. There was a difference of 34.6% between the original and modified cases. As a result, it was concluded that dimples had to put on the whole cylinder (as shown in Figure 46) in order to obtain better results with the pressure tappings. The pressure tapping matrix shown in Figure 47 was a 5×5 matrix which surrounded a dimple. And this dimple was located in the mid-span of the cylinder as well as the centre of the matrix. Different tappings were in different locations, some of them inside the dimple area, some of them on the

dimple edges, and others on the smooth surface of the cylinder between different dimples.



Figure 48 Modified dimpled cylinder (with sellotape)

In the stagger dimpled cylinder design, dimples were not simply aligned on the cylinder surface in a row-to-row, column-to-column format as in the mid-span tappings and matrix-type dimpled cylinders. In this design, dimples were in a staggered format, similar to those on a golf ball (Figure 49). A close up view of the matrix on the stagger cylinder was shown in Figure 50.

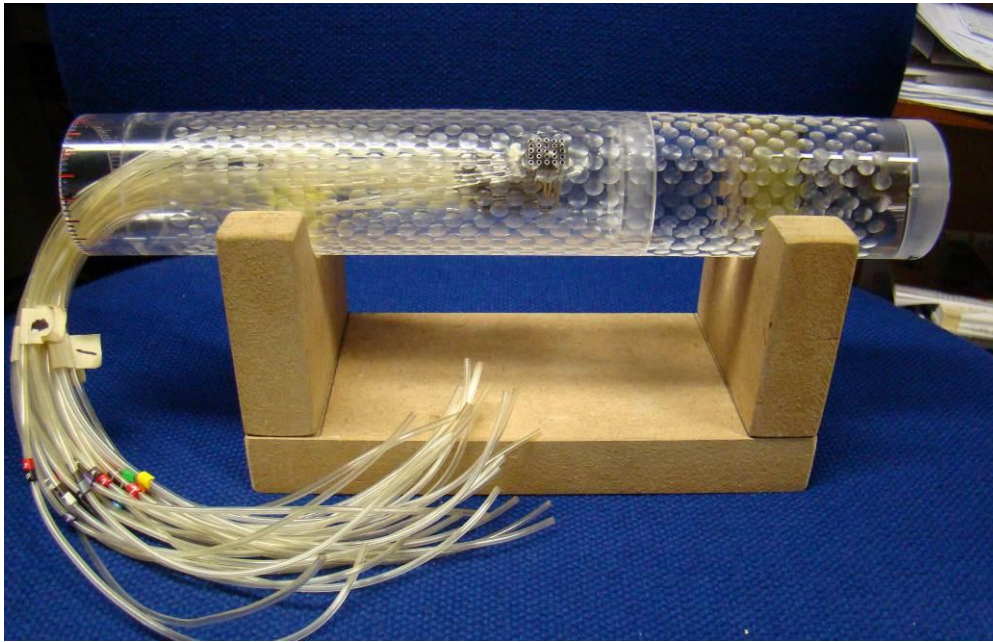


Figure 49 Stagger dimpled cylinder

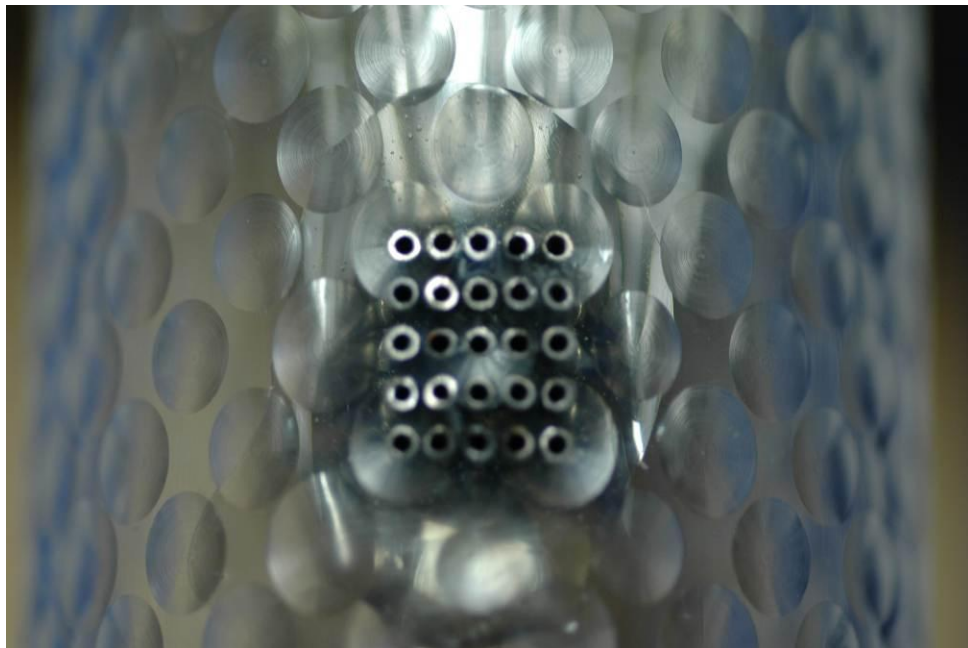


Figure 50 Close up view of the tapping matrix on the stagger dimpled cylinder

Figure 51 below showed the schematic drawings of the tapping matrix on the “matrix-type tappings, none stagger dimples” and the stagger dimpled cylinders. In this figure, the ellipses represented the dimples on the cylinder surface, and the 5×5 circles in a matrix format corresponded to the pressure tapping holes.

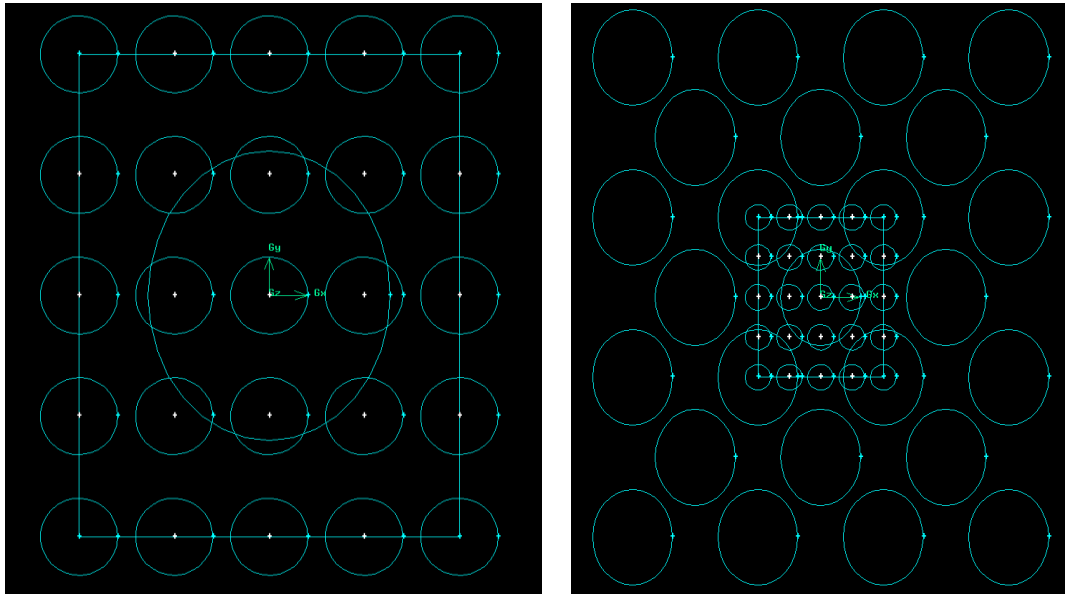


Figure 51 Schematic of the tapping matrix on the matrix-type and stagger dimpled cylinders

To measure the pressure distribution around the “matrix-type tappings, none stagger dimples” and stagger dimpled cylinders, the cylinders were rotated 20 increments (each 18^0) after each measurement. All five pressure tapping values in a row that lined up horizontally were connected to five pressure transducers with the same specifications, and the data from the LabView program was logged at each rotation. After measuring the first row from the top, then moved downward to the second, third, fourth, and finally the fifth row. Also, each row was rotated 20 increments to obtain the full pressure distribution around the circumference of

the cylinder at that height. After a full rotation for the cylinder, an equivalent of 80 pressure tapping measurements around the cylinder was obtained.

The C_d values obtained from the experiments for all four cylinders were plotted together in Figure 52. These four cylinders were:

1. A smooth cylinder with 36 pressure tappings (each 10 degrees apart) in the mid-span, which was taken as the reference.
2. The mid-span tappings, none stagger dimpled cylinder, with dimples along both the circumferential and axial directions and 60 pressure tappings around the mid-span.
3. The “maxtrix-type tappings, none stagger dimples”dimpled cylinder, with the same dimple design as the mid-span cylinder but with a 5×5 pressure tapping matrix around one dimple in the mid-span (Figure 51, left hand side). This was intended to test the effect in the span-wise direction as well.
4. The stagger dimpled cylinder, which has a staggered dimple configuration as well as using the same 5×5 matrix for measuring the pressure values (Figure 51, right hand side).

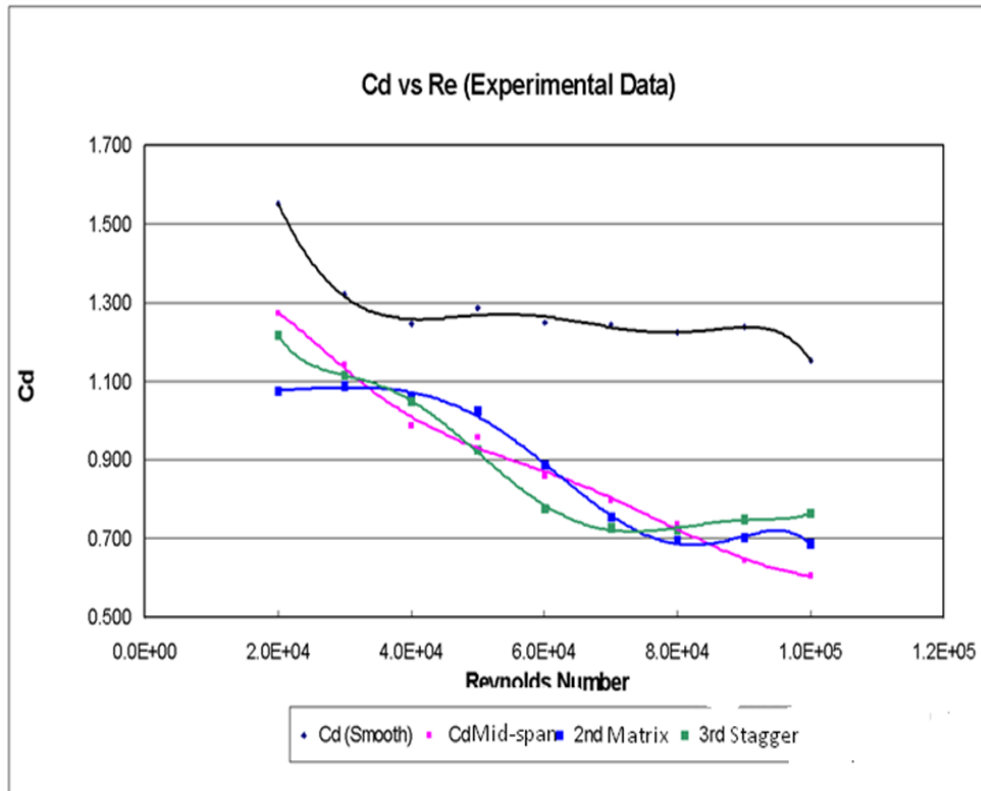


Figure 52 Comparisons of Cd for four cylinders

In Figure 52, the Cd variation was plotted against the Reynolds number for four different cylinders. Detailed Cd values and percentage reduction for different designs were also summarized in Table 7 and Table 8. The lowest Cd for each Reynolds number was highlighted in red in Table 7. It is shown that there was not a specific dimpled cylinder among the three designs that reduced the Cd most for all Reynolds numbers. The lowest Cd actually depended on different Reynolds numbers. As a result, each design had both pros and cons when tested under different Reynolds numbers.

Re	Cd (Smooth)	Cd (1st Dim)	Cd Reduction	2nd Dim Avg	2nd Dim R3	Cd Reduction	3rd Dim Avg	3rd Dim R3	Cd Reduction
2.0E+04	1.550	1.272	17.94%	1.075	1.064	30.67%	1.217	1.209	21.49%
3.0E+04	1.319	1.142	13.49%	1.088	1.080	17.52%	1.115	1.126	15.47%
4.0E+04	1.245	0.986	20.79%	1.060	1.033	14.88%	1.047	1.061	15.90%
5.0E+04	1.286	0.958	25.51%	1.023	1.036	20.44%	0.926	0.948	28.04%
6.0E+04	1.247	0.858	31.25%	0.886	0.861	28.95%	0.776	0.782	37.81%
7.0E+04	1.244	0.796	35.99%	0.753	0.709	39.46%	0.728	0.741	41.45%
8.0E+04	1.223	0.736	39.82%	0.694	0.652	43.25%	0.723	0.740	40.89%
9.0E+04	1.237	0.643	48.02%	0.703	0.698	43.21%	0.748	0.762	39.55%
1.0E+05	1.152	0.605	47.48%	0.686	0.693	40.49%	0.763	0.783	33.76%

Table 7 Cd and Cd reduction for different cylinders

Re	Cd (Smooth)	Cd (1st Dim)	2nd Dim Avg	2nd Dim R3	2nd Avg vs R3	1st vs 2nd Avg
2.0E+04	1.550	1.272	1.075	1.064	0.94%	15.52%
3.0E+04	1.319	1.142	1.088	1.080	0.78%	4.67%
4.0E+04	1.245	0.986	1.060	1.033	2.51%	-7.46%
5.0E+04	1.286	0.958	1.023	1.036	-1.28%	-6.80%
6.0E+04	1.247	0.858	0.886	0.861	2.85%	-3.34%
7.0E+04	1.244	0.796	0.753	0.709	5.78%	5.42%
8.0E+04	1.223	0.736	0.694	0.652	6.09%	5.71%
9.0E+04	1.237	0.643	0.703	0.698	0.71%	-9.26%
1.0E+05	1.152	0.605	0.686	0.693	-1.08%	-13.32%

Table 8 Direction comparison between two dimpled cylinders

Table 8 compared between the mid-span tappings and the matrix-type dimpled cylinders. They had the same dimpled configurations except for using different designs for the pressure tappings. The mid-span tappings, dimpled cylinder had 60 tappings around the mid-span of the cylinder, and pressure measurements were taken one by one without rotating the cylinder. The matrix-type dimpled cylinder had a 5×5 pressure tapping matrix around one dimple located in the mid-span. Five static pressure measurements for five tappings in a row were taken at the same time from five sensors. These sensors were of the same specifications and

had been calibrated. Then the cylinder was rotated 20 increments to get the full measurement of the static pressure around the cylinder. This resulted in 80 measurements of pressure on the cylinder.

The values in the column “2nd Dim Avg” in Table 8 referred to the average Cd for five different locations along the span on the cylinder. Static pressures at these five locations were measured by the five rows in the tapping matrix. Row 1 (R1) was on the top, followed by row 2 (R2), and finally row 5 (R5) at the bottom.

Table 8 also showed the Cd of the matrix-type cylinder in row 3 (R3). This row located in the mid-span of the cylinder, the same location as the pressure tappings in the mid-span tappings dimpled cylinders. The average Cd value in R3 were reasonably close, within a small range of 2–3%, except for $Re = 7 \times 10^4$ and 8×10^4 , which had differences of around 5%. However, when the differences between the mid-span tappings dimpled cylinder and the matrix-type one (average value) were examined, there were quite big discrepancies varying from +/- 3 to 15%. Some of the reasons might be:

1. Because the high cost of making perfectly circular cylinders, material with affordable and realistic price was used to make the cylinders, which would result in slightly non-circular.
2. It was difficult to maintain the pressure tapping holes in precise locations, both in the direction perpendicular to the cylinder surface and in locations

on the circumferential line of the cylinder. These small differences in the tapping locations would therefore influence the flow on the cylinder surface and in turns the static pressure.

3. Some of the tapping holes in the matrix of the matrix-type dimpled cylinder were inside the dimple region or on the dimple edges; others were on the smooth surface of the cylinder between different dimples and also along the axial direction. In this sense, the C_d value of the mid-span tappings dimpled cylinder was more representative for the mid-span, which also in the middle of the row of dimples in the mid-span, while in the matrix-type dimpled cylinder, the matrix covered a much wider region along the span, and then the average of the five rows along the span was taken. This C_d value obtained was much closer to the realistic case, because it not only reflected the drag coefficient for the mid-span of the cylinder (at a specific height), but along the span-wise direction as well.

Comparing all four cylinders, adding dimples on a cylinder can indeed reduce the drag coefficient on a circular cylinder for every Reynolds number in the experiments. However, no single specific dimpled cylinder among these three was found to be the best design under all the Reynolds numbers. Each of these three dimpled cylinders had both pros and cons. Therefore, different dimpled cylinders resulted in the lowest C_d for different Reynolds numbers. A universal best design was not practical and not likely to be found.

From another point of view, it indicated that specific designs themselves were not the key factor in determining the optimum design. Drag coefficients for different dimpled cylinders were reasonably close compared with the smooth case. Therefore, it could be concluded that the level of drag reduction was found to be insensitive to different dimpled patterns. This was also a benefit for not necessarily to decide which design would be the best for different cases.

Moreover, Figure showed the results reported by **Bearman and Harvey, 1993**. From $Re = 4 \times 10^4$, C_d started to fall from around 1.2 to a minimum of about 0.5~0.6 at around $Re = 1 \times 10^5$. A reduction in C_d of roughly 50% was reported at $Re = 1 \times 10^5$. According to their results, a lower C_d was obtained at $Re = 1 \times 10^5$ than any of the three dimpled cylinders in the current studies. However, at other Reynolds numbers, for example $Re = 2 \times 10^4$ to 5×10^4 , their design was not better than the dimple configurations investigated in the current test facilities. Furthermore, they only studied one dimple design and it had fewer dimples (12 dimples on a 100mm diameter cylinder in Bearman's design versus 20 dimples on a 50 mm diameter cylinder in the current cases) in the circumferential direction. It would be sensible to believe that some designs perform better and others may result in lower drag coefficients, depending on different Reynolds numbers. There was not a single design that was absolutely the best for all different Reynolds numbers so far.

The author would like to give a quick reminder regarding the difference in the Reynolds number between the experiments and the realistic applications. In the

real life, the Reynolds number could go up to $Re = 1 \times 10^6$, which covers all three subcritical, critical, and supercritical regions. The critical and supercritical regions cannot be matched in the current experiments. These regions are also very difficult to predict and the results are extremely sensitive to experimental conditions, especially the critical regime. There are a lot of uncertainties in the predictions and extrapolations if only based on the subcritical results.

4.4 CFD Simulations and Results on Different Dimpled Designs

Besides using experimental methods, computational simulations on various dimpled cylinders have also been tested. In the following sections, modelling techniques and results obtained from the simulations will be discussed.

As mentioned in the previous section, a laminar modelling in CFD could also provide valuable information even when the flow involves turbulence. Reynolds Average Navier-Stokes (RANS) equations are the oldest and classical approach to turbulent modelling. However, they do not solve the Navier-Stokes equations explicitly; instead, they approximate. To really understand the flow behaviour inside dimples, especially three-dimensional dimples, better simulation techniques have to be considered. Therefore Large Eddy Simulation (LES) and Direct Numerical Simulation (DNS) came into consideration. However, with the current computer power and the high Reynolds number involved in this project, DNS is not practical. By contrast, LES might be a better alternative choice.

The model was firstly run with a 2D laminar model in FLUENT in a relatively coarse mesh with around 100K quadrilateral cells. It was believed that if the grids were continually refined and the step size decreased within each shedding cycle, at some point, the curve, for example, the drag coefficient would not show a smooth pattern any more as shown in Figure 37. It was expected that if the accuracy of simulation improved both in time (smaller time step size) and space (refining the grids), the model would finally pick up some turbulence (large eddies), and it would behave what is normally called “LES calculation without a sub-grid model” or “coarse grid DNS”.

The general concept of LES is that large eddies of the flow are dependent on the flow geometry, while smaller eddies are similar to one another and have a universal character. For this reason, it became a practice to solve only the large eddies explicitly and to model the effect of the smaller and more universal eddies. Thus, in LES, the large scale motions of the flow are calculated, while the effect of the smaller universal scales (the so called sub-grid scales) is modelled using a sub-grid scale (SGS) model. Therefore, in our modelling approach, it was intended to solve the large scale eddies only by using laminar calculations.

An example to demonstrate this is as follows. A 2D case with 20 dimples around the circumferential line of the cylinder (dimple depth = 0.45 mm) was simulated in the same domain as before. The inlet flow velocity was 30 m/s, which resulted in $Re = 1 \times 10^5$. An example of the mesh around the dimpled cylinder in the

coarse case was shown in Figure 53. Quadrilateral cells were meshed around the cylinder surface and also extended to the whole domain.

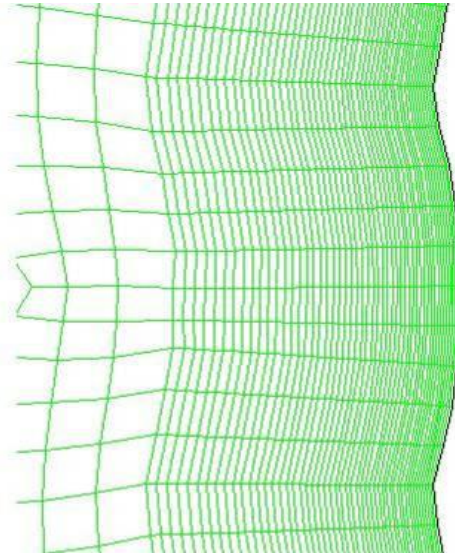


Figure 53 Quadrilateral mesh around the dimpled cylinder

Table 9 showed the results for different meshes.

Case	Cell number	Time steps in one cycle	Time step size (s)	Cd
Case01	110K	30	0.00025	1.573
Refine01	$110K \times 4$	$30 \times 1/4$	$0.00025 \times 1/4$	1.829
Refine02	$110K \times 16$	$30 \times 1/16$	$0.00025 \times 1/16$	0.619
Refine03	$110K \times 64$	$30 \times 1/64$	$0.00025 \times 1/64$	~ 0.5

Table 9 Drag coefficient for different cases

Higher values of Cd in Case01 and Refine01 could be due to the laminar model was still not able to capture the flow behaviour properly, which resulted in the accumulation of relatively more computational error and caused higher drag

coefficient values. However, in the next two cases, i.e., Refine02 and Refine03, the drag coefficient dropped down significantly and showed promising results. These values firstly confirmed that dimples could indeed reduce the drag coefficient on the cylinder, and also agreed with the studies by **Bearman and Harvey, 1993**. Figure 54 plotted the C_d vs flow time for the Refine03 case listed in the table. From Figure 54, it can be seen that the C_d curve was a “saw-tooth” curve. The main trend was similar to the smooth curve shown in Figure 37, but with small “saw teeth” superimposed on top of the smooth curve as well. These saw teeth indicated the small turbulent behaviour had been picked up in the laminar simulation. Therefore, this clearly confirmed that down to this resolution of time and space, the laminar calculation could indeed pick up the turbulence and behaved similarly to an LES calculation without a sub-grid model.

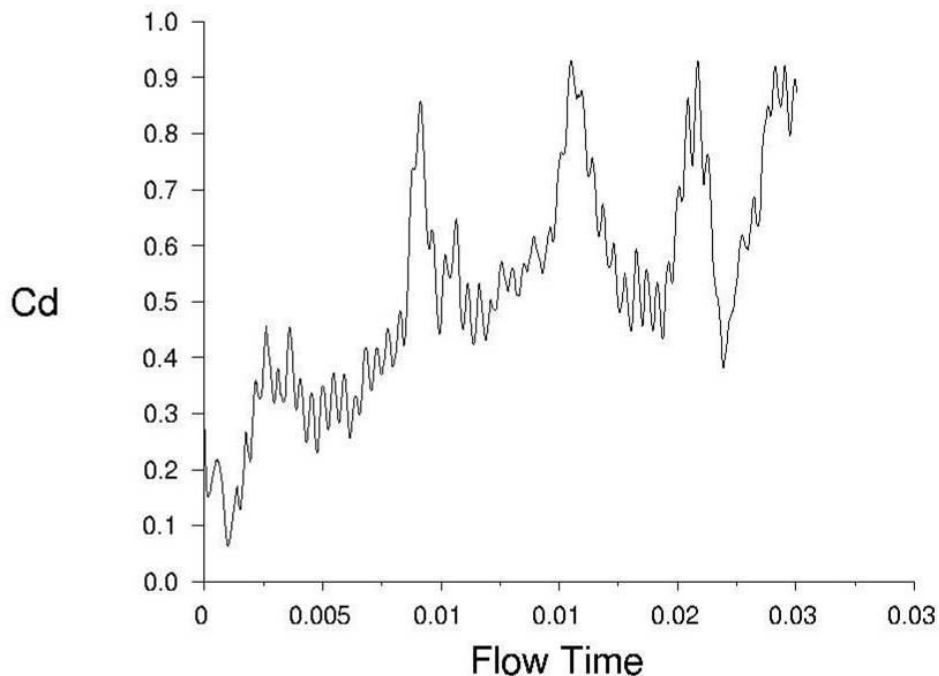


Figure 54 Plot of drag coefficient against flow time

However, another important factor must be pointed out. There were nearly seven million cells in the domain in the previous “coarse grid DNS” model, which meant it was very computationally expensive and required significant CPU time to obtain solutions. For example, the case of Refine03 required about ten gigabytes of RAM during simulation, and the time step size needed to go down to a very small value of 0.000004 seconds, with 30 iterations per time step. To reach 0.02 seconds of solution time (flow time), it took over 10 days to solve the model on the computer cluster with 24 CPU nodes. Therefore it was very time-consuming and computationally expensive.

When the mesh quality is quite coarse, the C_d value was around 1.5 to 1.8. According to the data in the literature and experiment, C_d value was expected to be around 0.4 to 0.6. Therefore, it is expected that C_d will drop when refining the mesh. However, according to the trend of the drag coefficient shown in Table 8, it did not display this trend when changing from case01 to refine01. This implied that the results relied on the meshes of the model and the turbulence. In turns, these factors had big impacts on the solutions. On the other hand, the CFD method did not predict very well when using coarse meshes. Keep refining the mesh requires great computational effort, but the low value of C_d could only be obtained from very fine models and small time step sizes inside each shedding cycle. As mentioned, this required about seven million cells and took over ten days to reach 0.02 seconds from a computer cluster with 24 CPUs. It may not be wise and practical to run many cases for these kinds of big simulations. An alternative approach was to run small simulations, and then compared these

preliminary results to find out which ones seemed to give lower drag coefficients, and then conducted the refinements.

At the end of the research paper by **Bearman and Harvey, 1993**, they suspected that bigger drag reductions might be obtained with other dimple designs or with a different arrangement of dimples. However, they did not offer more information on those possible designs. So far, not many publications on this topic could be found.

With some basic understandings of fluid mechanics, some pilot tests on other dimple designs were carried out. Key parameters in dimple designs include dimple depth, dimple diameter, shape of dimples, and dimple distributions. Within these parameters, the dimple shape would remain the same as on a traditional golf ball, and dimples would be made by cutting with a spherical cutter. As we can imagine, fluid mechanically, spherical dimples have the advantage of allowing the flow to go inside and leave nicely. With suitable depth, flow separation may be avoided. At the same time, the flow will be easier to reattach back on the cylinder surface again. It is quite natural that this shape would be better than some others.

Regarding the dimple distributions, at the current stage, a full 3D CFD simulation may not be very suitable because it requires even more computer power than 2D simulations. In 2D models, distribution will then mean the number of dimples around the circumferential line of a 2D cylinder.

For the reasons mentioned above, several cases with different dimple parameters were run with 2D CFD methods, and the results were listed in Table 10.

Case	Number of dimples	Dimple depth (mm)	Cd
Case02	15	0.30	1.412
Case03	15	0.45	1.491
Case04	15	0.60	1.554
Case05	20	0.30	1.549
Case06	20	0.45	1.668
Case07	20	0.60	1.642
Case08	30	0.30	1.466
Case09	30	0.45	1.448
Case10	30	0.60	1.481

Table 10 CFD results for preliminary coarse mesh cases

Case02, case03, and case04 in Table 10 shared the same number of dimples, which was 15, around the 2D cylinder. Compared with other cases with more dimples, fewer dimples could cause less flow interference between each other. For example, the flow leaving the trailing edge of the mid-span tappings dimple would have more distance to travel before reaching the leading edge of the matrix-type dimple. From this aspect, the flow had a higher chance of reattaching on to the cylinder surface. Further examination of the values of the drag coefficient in case02, case03, and case04 showed that the trend of reducing the depth of dimples would result in a lower drag coefficient. This actually reflected the fact reported in the literature that the surface roughness was an important

factor in drag reduction studies, and dimple depth could be considered to be a form of surface roughness.

However, when all the C_d values in Table 10 were examined, it could be seen that they were in the range of 1.4 ~ 1.7, a lot higher than the C_d for the smooth cylinder. This implied that dimples caused the drag force to increase rather than decrease at first glance. Nevertheless, it is necessary to keep two things in mind. First of all, this was a two-dimensional simulation. Researchers like **Bearman, 2009**, argued that in the case of a golf ball, the complicated three-dimensional small-scale longitudinal vortices which are normally believed to develop around the edge of the whole dimple geometry could not be captured in two-dimensional simulations. As a result, those vortices could not fully propagate back as the trailing vortices and energize the boundary layer. Hence, flow separation cannot be reflected in two-dimensional simulations as in three-dimensional full modelling.

However, the experimental results (three-dimensional) of the mid-span tappings dimpled cylinder and two-dimensional CFD simulations, refine02 and refine03 seemed to be relatively close. This may indicate that even results from two-dimensional simulations can also be used for comparisons with three-dimensional experimental data. They may only offer a rough guide anyway. However, the significant computer power required in these simulations, even in two-dimensional, should not be underestimated. Secondly, from the previous discussion, results in Tables 9 and 10 indicated the close relationship between the

meshes and the simulation results. All the cases in Table 10 were obtained from low quality meshes with around 100K cells in the domain. Therefore, it was not surprising to find higher drag coefficients in these cases. And the Cd values found from these coarse simulations should not have high reliability.

4.4.1 Conclusions on CFD Side

To sum up, the computational method could be useful to provide information on the flow passing around dimples. However, this technique highly depended on the mesh of the geometry and grid quality. Applying any turbulence model with the RANS method did not seem to be appropriate. Using LES calculation without a sub-grid model was promising. However, great computer power was needed to obtain valuable results.

4.5 Comparison between Experimental and Computational Methods

In the experiments, flow behaviour was dominantly three-dimensional. However, in the pilot tests of those CFD simulations, even two-dimensional calculations were very CPU expensive. It would be much worse for three-dimensional CFD simulations. Wind tunnel testing was used as the main investigation technique and it was a quicker way to obtain results compared with computational simulations in this project. Therefore, experimental technique will serve as the main research approach in these studies. Compared with the experimental technique, computational simulation would not be suitable for seeking good answers to this

project's objectives. By contrast, the experimental method would be more appropriate.

4.6 Checking the Time-Mean Lift Coefficient

The lift coefficient (Cl) values were also checked from the experimental data. Integrated values of Cl were quite small and close to zero, in the range of 0.06 to 0.09, depending on different designs and different Reynolds numbers. This indicated that the time-mean average lift on the cylinder was roughly cancelled out on the upper and lower halves of the cylinder (top view, along the axial direction). These results could also help to improve the confidence of the experimental data as well.

4.7 Uncertainty and Repeatability of the Experiments

Connections for experimental measurements were relatively simple (Figure 55). Tubes connected different pressure tapings to sensors, and then outputs of the sensors (voltage signal) were picked up by the data acquisition unit. Finally the signals were sent to the computer. In this whole process, only the voltage signals were measured by the data acquisition unit, which was a high accuracy device. When the full scale was set to ± 5 V, the absolute accuracy of the device was 1.41 μ V. This corresponded to 5.6×10^{-5} %, which was a very small value and indicated the high accuracy of the measurement system (**Moffat, 1982, Kline and McClintock, 1953**).

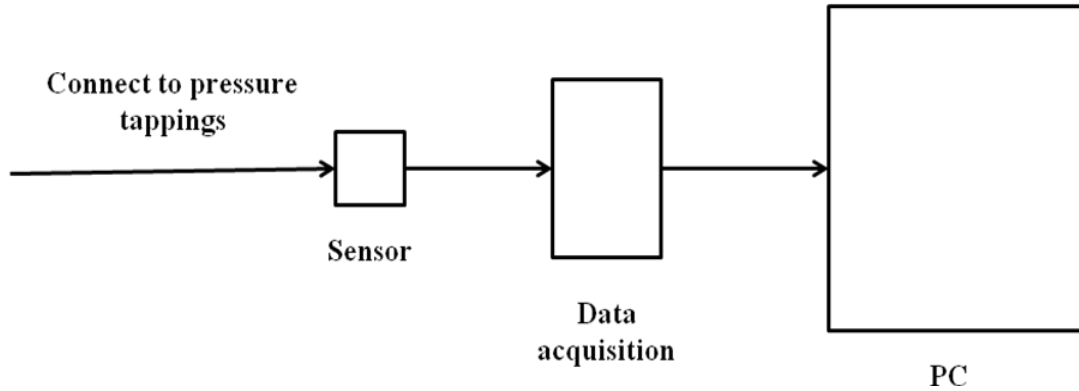


Figure 55 Schematics for measuring the pressure

Some of the experiments were also repeated. Differences between C_d values under the same Reynolds numbers were found to be very small and within 2%, which reflected the high reliability and repeatability of the experiments.

$$C_d = \int_0^{2\pi} C_p(\theta) \cos(\theta) d\theta \quad \text{Equation 6}$$

Drag coefficient (C_d) was obtained from Equation 6. Therefore, uncertainty of C_d also came from this integration. Figure 56 showed the matrix-type dimpled cylinder and a component used to fix on the top panel of the wind tunnel for indicating the rotation of cylinders. A close up view was shown in Figure 57. The cylinders were rotated 20 times during experiments. When the red line on the cylinder lined up with the red line on the small component, the cylinder stopped and started to take the measurements. There are 20 red lines on the cylinder in total, therefore, divided the cylinder into 18-degree sections. The width of the red lines was approximately 0.5mm.



Figure 56 Matrix-type dimpled cylinder with a small component near the top

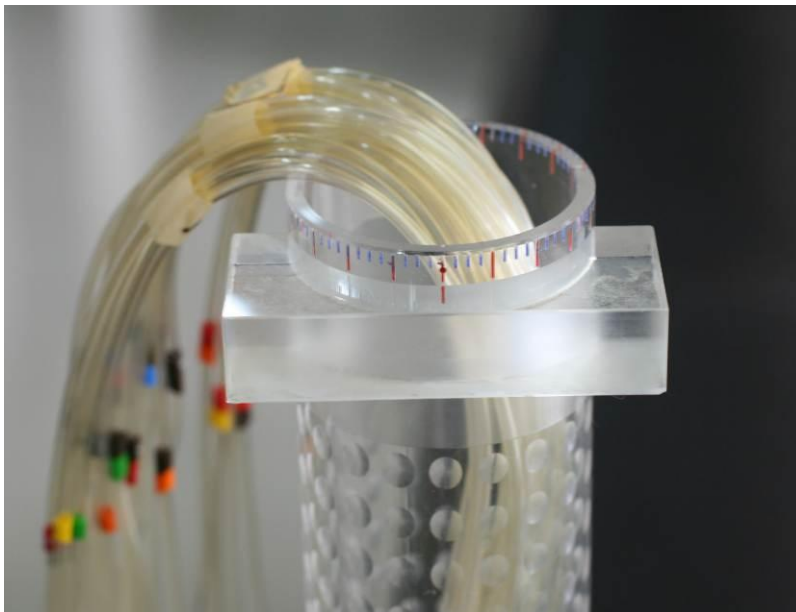


Figure 57 A close up view of the component and the top of the cylinder

Some uncertainty occurred when using the cylinder. First of all, those red lines may not strictly be on the exact places where they were supposed to be due to manufacture error. Secondly, when rotating the cylinder, it was difficult to guarantee the red line on the cylinder lined up with the red line on the small component perfectly. Thirdly, as mentioned previously regarding the accurate location of the pressure tapings, it was also a challenge to put the tapings on the exact locations on the cylinder surface (both in the span-wise and circumferential directions). These factors were relatively difficult to estimate. For these reasons, they would be neglected at the moment and only the pressure coefficient (C_p) contributed to the uncertainty of drag coefficient.

C_p comparison with standard deviation error bars superimposed for two different Reynolds numbers was also done. Results were plotted in Figure 60. It could be seen that the error bar was obviously bigger in the case of $Re = 2 \times 10^4$ than in the case of $Re = 8 \times 10^4$. This result helped to explain the increase of drag coefficient around $Re = 2 \times 10^4 \sim 3 \times 10^4$ in Figure 61. Previously, it was mentioned that the fan had to operate at a certain range of RPM. Even though the maximum was around 1500 RPM, the lower limit for the operational condition was around 300 RPM, where it resulted in $Re = 2 \times 10^4$. In fact, at around 350~400 RPM, the noise from the fan would increase noticeably compared with mid-range values like 700~800 RPM. At low speed, fan noise would go up. Furthermore, the sound was not stable and remained constant, as if there were some kind of vibration inside.

This, together with the bigger error bar in $Re = 2 \times 10^4$ shown in Figure 58, helped to explain the C_d values increased at low Reynolds numbers.

- a. Firstly, the standard deviation in Figure 58 refers to the unsteadiness and electric noise of the measurement system.
- b. Secondly, the bigger error bar indicated that the uncertainty was bigger. Hence the confidence of the results was not as good as in the case of $Re = 8 \times 10^4$, which also plotted in Figure 58.

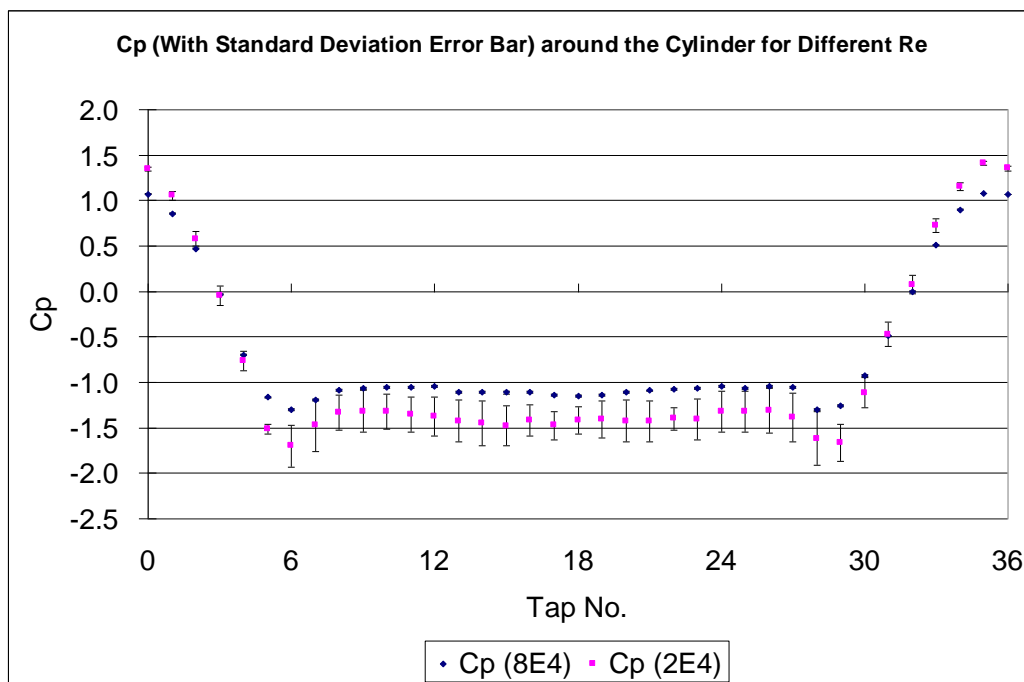


Figure 58 Cp plots with standard deviation error bar superimposed

Drag coefficients were calculated from Equation 6, and the uncertainty was also derived from this method. Table 11 to Table 14 summarized the standard deviations for different cylinders under different Reynolds numbers.

		Std. deviation range of Cp	Std. deviation value of Cd
Smooth	Re = 1E5	0.032 ~ 0.375	0.323
	Re = 9E4	0.027 ~ 0.367	0.215
	Re = 8E4	0.021 ~ 0.291	0.227
	Re = 7E4	0.016 ~ 0.200	0.173
	Re = 6E4	0.011 ~ 0.142	0.121
	Re = 5E4	0.007 ~ 0.077	0.068
	Re = 4E4	0.005 ~ 0.044	0.042
	Re = 3E4	0.004 ~ 0.026	0.020
	Re = 2E4	0.003 ~ 0.012	0.012

Table 11 Standard deviations of Cp and Cd for smooth cylinder

		Std. deviation range of Cp	Std. deviation value of Cd
Mid-span tappings dimpled cylinder	Re = 1E5	0.026 ~ 0.160	0.064
	Re = 9E4	0.018 ~ 0.150	0.062
	Re = 8E4	0.016 ~ 0.149	0.065
	Re = 7E4	0.013 ~ 0.117	0.058
	Re = 6E4	0.009 ~ 0.067	0.031
	Re = 5E4	0.006 ~ 0.030	0.017
	Re = 4E4	0.005 ~ 0.022	0.019
	Re = 3E4	0.003 ~ 0.016	0.010
	Re = 2E4	0.002 ~ 0.010	0.007

Table 12 Standard deviations of Cp and Cd for mid-span tappings dimpled cylinder

		Std. deviation range of Cp	Std. deviation value of Cd
Matrix-type dimpled cylinder	Re = 1E5	0.031 ~ 0.223	0.088
	Re = 9E4	0.026 ~ 0.194	0.084
	Re = 8E4	0.028 ~ 0.195	0.087
	Re = 7E4	0.022 ~ 0.186	0.076
	Re = 6E4	0.017 ~ 0.108	0.053
	Re = 5E4	0.012 ~ 0.064	0.035
	Re = 4E4	0.011 ~ 0.042	0.039
	Re = 3E4	0.009 ~ 0.056	0.034
	Re = 2E4	0.007 ~ 0.025	0.022

Table 13 Standard deviations of Cp and Cd for matrix-type dimpled cylinder

		Std. deviation range of Cp	Std. deviation value of Cd
Stagger dimpled cylinder	Re = 1E5	0.036 ~ 0.228	0.091
	Re = 9E4	0.027 ~ 0.190	0.083
	Re = 8E4	0.026 ~ 0.192	0.081
	Re = 7E4	0.021 ~ 0.178	0.072
	Re = 6E4	0.015 ~ 0.097	0.048
	Re = 5E4	0.013 ~ 0.070	0.036
	Re = 4E4	0.013 ~ 0.071	0.035
	Re = 3E4	0.007 ~ 0.049	0.029
	Re = 2E4	0.008 ~ 0.023	0.021

Table 14 Standard deviations of Cp and Cd for stagger dimpled cylinder

From these tables, we can see that the standard deviations of Cd were nicely fall between the minimum and maximum values of pressure coefficient (Cp), within one maximum standard deviation of the Cp measurements. Estimations of these values also supported the conclusions made previously. Measurements from the

experiments were reliable and with good repeatability. Standard deviations of pressure coefficient and drag coefficient were small. Furthermore, standard deviations of C_d were within one maximum standard deviation of C_p as well.

4.8 Conclusions on Results and Discussions

The targets set in Section 3.1 were met. Components of the wind tunnel were designed and built, and then cylinder parameters were determined. Next, PCB circuits and the data acquisition system were constructed and the pressure transducers were calibrated. In Chapter Four, wind tunnel experiments were carried out for four cylinders (one smooth and three dimpled cylinders) under various Reynolds numbers. Finally, values of the lift coefficient and uncertainty were also checked. Different aspects proposed at the beginning of this chapter were discussed in details in the experimental sections of this chapter.

Following the investigations, answers to the key questions posed in Chapter One are:

- a. It was found that applying dimples on the outer surface can significantly reduce the stream-wise force on the cylinder, by 17% to 48% depending on different Reynolds numbers. However, C_d values for different dimpled designs at the same Reynolds number were reasonably close when compared with the smooth case. Therefore, it could be concluded that changing the level of drag reduction was found to be insensitive to different dimpled patterns and specific dimpled design was not the key

factor in determining the optimum design. A universal best or optimum design was not likely to be found. In other words, drag coefficient was not sensitive to different dimple designs. This is also a benefit for not necessarily deciding which design is the best for different cases.

- b. Regarding the CFD method, because it required significant computer power to obtain solutions. Therefore, compared with the experimental technique, computational simulation would not be suitable for seeking answers to this project. By contrast, the experimental method would be more appropriate to provide answers.

4.9 Differences between Experiments and Real Life Situations

Some differences between the methods used in this project and real life deep sea mining environment cannot be avoided. With the available time and resources, the author could only try his best to simplify the project with some assumptions. Some discrepancies are listed below.

- a. Different fluid media. The experiments could only be conducted in the subcritical regime. This difference may also result in different fluid–structure interaction behaviours.
- b. In real life scenarios, flow also covers the critical region, which is commonly regarded as a regime that is very difficult to predict and verified by experiments. Estimation of the flow behaviour could only base

on the results obtained in the subcritical region and some other empirical data.

- c. The non-uniform velocity profile along the lifting pipe mentioned at the beginning. It was assumed that the surface current is generally restricted to the upper 200 metres of the ocean, which is in the stream-wise direction (X direction) to the lifting pipe. For simplicity, a linear variation of the velocity profile was assumed. Typical speed of the ocean current would be around 1 m/s on the ocean surface, then decrease linearly and vertically downwards in the span-wise direction (Z direction). The flow was considered to be static below 200 metres.

- d. Two-dimensional CFD simulations in FLUENT always assume an infinite aspect ratio of the model. This means infinite length inside the screen, and it would affect the flow behaviour as well.

Chapter 5

5. Flow Visualization

In this chapter, it is intended to show the wake regions for smooth and dimpled cylinders. And support the conclusion that the stream-wise force is smaller for the dimpled cylinder. Therefore, different components for flow visualization will be outlined in detail. And then, various designs of the components and process of the experiments will be described.

5.1 Introduction of the Smoke Generator

Key equipment involved in this investigation was a smoke generator and a CO₂ vapour cylinder, which used to supply CO₂ and then mix with the smoke oil in the oil tank inside the smoke machine. The smoke generator was made by Concept Smoke Systems as shown in Figure 59.



Figure 59 Oil type smoke machine

The smoke machine was an oil type smoke generator. The smoke effect was actually a fog or aerosol comprising millions of tiny liquid spheres. The refraction and diffraction of light through these particles created an effect of smoke.

The mechanism of producing smoke was the smoke oil would be heated above its boiling point and then turn into vapour inside the smoke generator. When the vapour exited the heat exchanger and exposed to the colder atmospheric air, it expanded and cooled rapidly, and then condensed to produce the aerosol particle. A general specification of the smoke machine was listed in Table 15.

Specification	Model: Vicount oil based
Size (cm)	41 × 18 × 37
Weight (kg)	12
Power supply	230v, 50Hz
Warm up time from cold (mins)	4
Particle size (micron)	0.2-0.3
Heat exchanger wattage (W)	1100
Running time at maximum output (min)	40
Smoke output (m ³ /min @ 1.0m visibility)	0-150
Smoke oil consumption (ml/hr)	2000

Table 15 Technical specification of the smoke generator

5.2 Successful “L-shape” Probe

After a lot of effort to find suitable method to produce acceptable smoke stream in the working section, it was found that the “L-shape” probe with diameter of 10mm. The probe was mounted on one of the traverse systems, and setup in front of the cylinder, location of the probe along both the stream-wise direction(X direction) and traverse direction (Y direction) could be adjusted. This was shown in Figure 60.

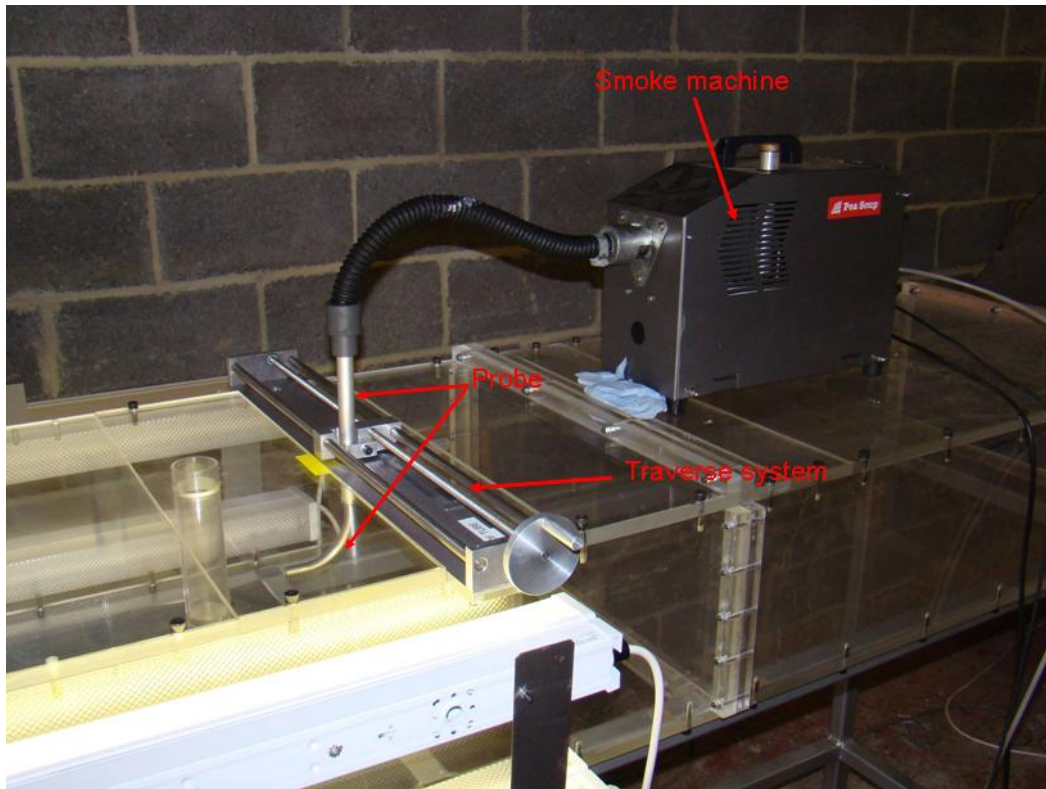


Figure 60 Smoke machine put on top of the rig and connected to the probe

5.2.1 Results on Flow Visualization

When the probe was held and tried to determine a starting point for the location (as shown in Figure 60) of the fixed probe, i.e., distance between the probe exit and the front of the cylinder. It was found roughly between 60~110mm would give relatively good quality of results. Therefore, the exit of the probe was decided in three different locations ahead of the cylinder. They were 65mm, 85mm, and 105mm from the probe exit to the front of the cylinder. Also, these three locations were donated as “position 65mm”, “position 85mm”, and “position 105mm”.

Figure 61 to Figure 63 showed the images when moved from position 65mm to position 85mm and finally to position 105mm for the same Reynolds number ($Re \sim 3 \times 10^4$). The smooth cylinder was used in these three tests.



Figure 61 Picture showed the visualization result on the smooth cylinder when the probe was at position 65mm

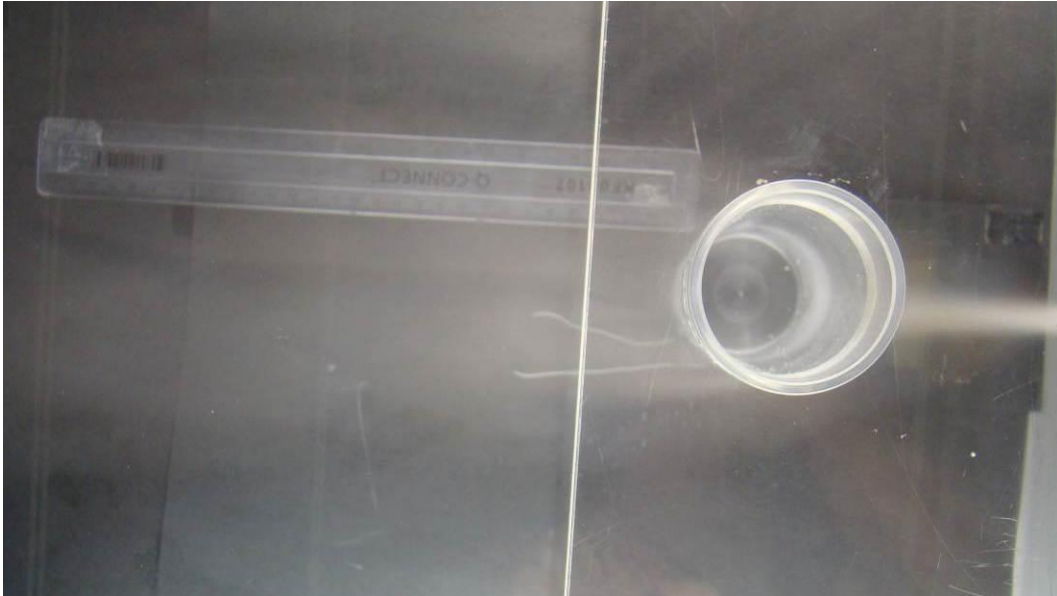


Figure 62 Flow image when the probe was at position 85mm

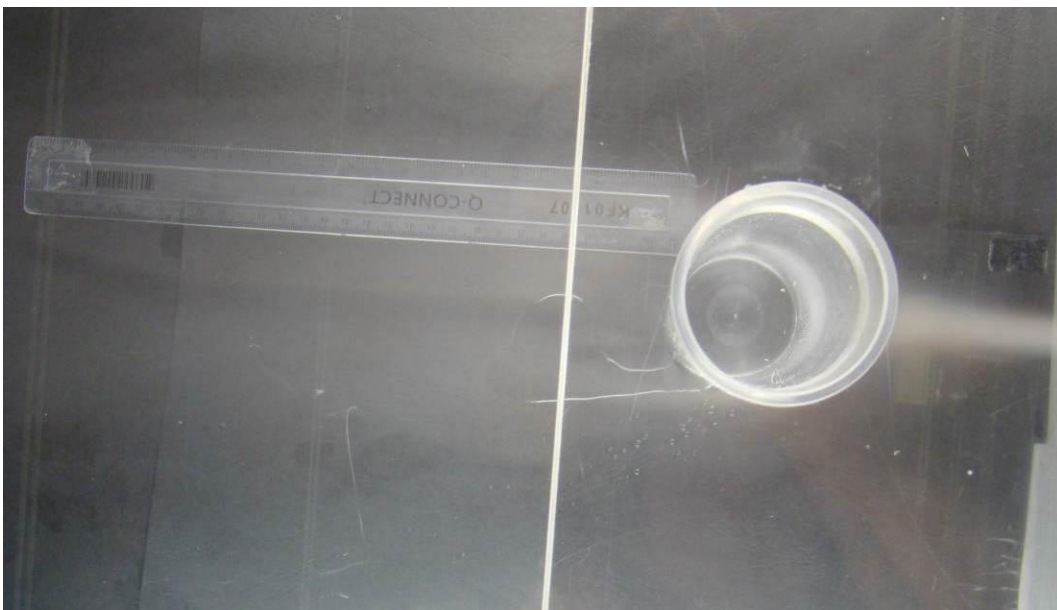


Figure 63 Flow image when the probe was in position 105mm

From these three figures, it was clear that when the probe was at position 65mm, the smoke was the thickest, and then the smoke became thinner and thinner when the probe moved to position 85mm and finally to position 105mm.

There were mainly two reasons for the phenomenon mentioned in the previous paragraph. Firstly, when the distance between the probe and the cylinder increased, the smoke came out from the probe exit had a longer distance to travel before it reached the cylinder. Therefore, the smoke would dissipate more, and became thinner. Secondly, moving from position 65mm gradually to position 105mm was actually towards the blower, i.e., in the opposite direction of the wind produced by the blower. In this case, some of the wind may get into the probe exit from the rim of probe. Hence, back pressure was increased inside the probe. This could be confirmed by another observation when moving the probe from position 65mm to position 105mm. At position 65mm, the exit pressure from the smoke machine was in the right value and not much back pressure was produced. However, at position 105mm, the back pressure became higher. Certain amount of smoke was actually leaking from the side panels of the smoke generator. By contrast, hardly any leakage could be seen when the probe was at position 65mm.

Figure 64 and Figure 65 directly compared the flow pattern for a smooth and a dimpled cylinder. It was clear that the wake region was much smaller behind the dimpled cylinder than in the smooth one. The wake region for the smooth cylinder formed within a region roughly between eleven o'clock and seven o'clock. The slight non-symmetrical pattern was because the figure was an instantaneous image, periodic vortex shedding pattern would occur behind the cylinder and therefore the non-symmetrical pattern in this instantaneous shot. However, when examined the wake behind the dimpled cylinder, it was obviously smaller. Within a region

roughly between ten o'clock and eight o'clock, and it is also instantaneous image as well.

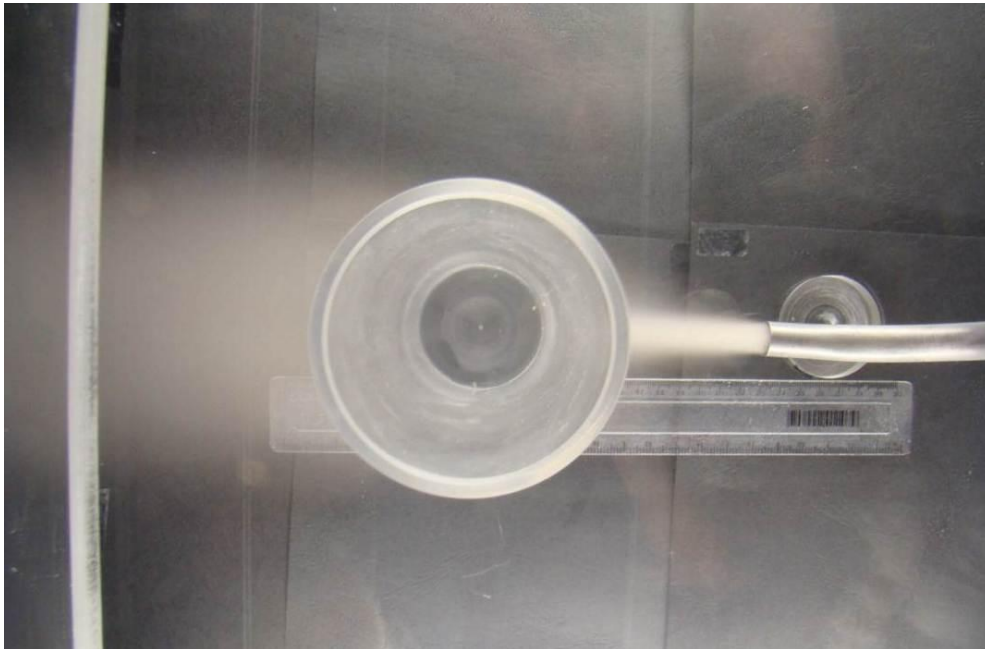


Figure 64 Image showed the wake region behind the smooth cylinder

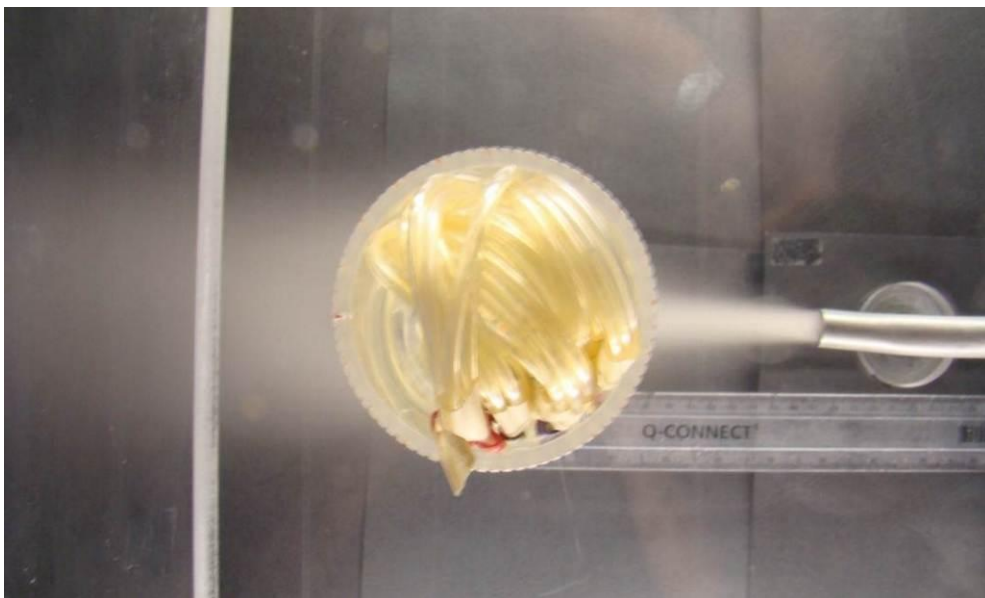


Figure 65 Flow visualization image for the dimpled cylinder

5.3 Conclusion on Flow Visualization Experiments

In this chapter, it showed the setups and different components used during flow visualization. The smoke machine, CO₂ vapour cylinder, and different kinds of smoke exits were essential. Furthermore, the centrifugal fan was also used as an optional component at some stages.

Direct injection of smoke to the fan intake did not give good results. Then a smoke rake connected behind the centrifugal fan was tested. Due to the small diameter of the tube, which created a high back pressure, this idea was later replaced by a single probe. However, it still needed to find a suitable diameter for this probe. Firstly, 6mm in diameter was studied, back pressure was high and there was leakage from the side panels of the smoke machine. When increased the diameter to 10mm, it gave reasonably good results even without the centrifugal fan.

And then it was started to test where the best location for the probe was in the rig. Three locations for the probe were experimented. Different locations gave different thickness of the smoke because different pressure of the wind as well as smoke dissipation.

At the best location, good images for the wake region for both smooth and dimpled cylinders were captured. It was clear that wake region behind the dimpled cylinder was much smaller than the one behind the smooth cylinder. It

also confirmed experimental data in Chapter 4 that applying dimples on the cylinder surface can indeed reduce the stream-wise force.

Chapter 6

6. Summaries and Conclusions

The arguments, methodologies, and conclusions in previous chapters will be briefly summarized in this chapter. Basically, objectives for different sections, methods of investigation, results and discussions, and finally conclusions will be re-emphasized in this chapter.

6.1 Preparations and Experimental Setups

Considering the friction force only contributes to less than 3% in the Reynolds number region interested. The investigation would mainly focus on the time-averaged pressure drag.

An existing blower, a speed controller and other components were included in the experiments. Other components like: proper convergent section, straight working section, test cylinders, as well as dimensions of these components were designed carefully. After these parameters were determined, suitable pressure transducers were chosen. And then, these sensors should be calibrated before an input pressure could be properly converted to a voltage signal. These pressure transducers were next connected to a data acquisition unit, which was then connected to the computer through a USB interface. In order to obtain the voltage signals from the sensors, extra LabView codes had to be written. By using these LabView codes, different parameters could be changed and obtained easily, for

example, sampling rate, number of samples, and number of sensor channels as well as standard deviations.

6.2 Results and Discussions of Smooth Cylinder

Experiments on the smooth cylinder was set to test the different sampling rates and the numbers of samples for $Re = 1.0 \times 10^5$. Results were plotted together and the curves were very close. There was not much discrepancy found and the results indicated the high accuracy of the measuring system.

The second round of experiments were carried out for different Reynolds numbers, varying from $Re = 0.2 \times 10^5$ to 1×10^5 . Pressure coefficients around the mid-span of the smooth cylinder were plotted, the curves came out to be quite close together even under different conditions of Reynolds numbers, except for $Re = 0.2 \times 10^5$. In Section 4.1, it was mentioned that this was because the earlier separation of the flow from the cylinder surface. Therefore, it resulted in the pressure coefficient curve at $Re = 0.2 \times 10^5$ deviated from other curves for different Reynolds numbers, and also caused the highest drag coefficient in the whole experiments.

Other than experimental method, a computational technique was also used to calculate the drag coefficient. ANSYS FLUENT was used as the main CFD tool. At the beginning of this section, different turbulence models in FLUENT were studied to see whether they could give decent results when comparing with the accepted data in the open literature. Unfortunately, CFD only predicted C_d around 0.5~0.6 at $Re = 1 \times 10^5$, only half of the accepted value of 1.2. Therefore, it would

not be suitable to force the simulation with turbulent models when the flow condition was close to the transition regime. An alternative approach applied in the investigation was to use laminar simulation, because it could still pick up the turbulent behaviour. The laminar calculations finally predicted a drag coefficient with about 4% difference to those measured from experiments, which was quite a good agreement.

6.3 Results and Discussions on Dimpled Cylinders

Three dimpled cylinders were tested in the experiments. The mid-span tappings was scaled from golf ball dimples with 60 pressure tappings in the mid-span of the cylinder. The matrix-type cylinder had the same dimpled distribution as the mid-span tappings design but with the pressure tappings in a 5×5 matrix. Measurements were done after taking the 25 readings from the matrix and then rotated the cylinder to measure the pressure at other surface locations of the cylinder. This matrix could measure the pressure along the circumferential line of the cylinder, as well as along the cylinder span (Z direction). The stagger design for the dimpled cylinder was similar to the previous one with the exception of the stagger-dimple distribution. It also applied the 5×5 matrix to obtain the measurements in two directions.

By comparing the smooth and all three dimpled cylinders, adding exterior dimples could indeed reduce the drag coefficient of the cylinder at each Reynolds number studied in the experiments. However, no single specific dimpled cylinder among these three was found to be the best under all the Reynolds numbers investigated.

Each of the three dimpled cylinders had both pros and cons. Therefore, different dimpled cylinders resulted in the lowest C_d at different Reynolds numbers. An optimum design which gives the lowest C_d at every Reynolds number was not practical and not likely to be found at current research stage.

From another point of view, it indicated that specific dimpled design was not the key factor in determining the optimum design. Compared with the smooth case, drag coefficients for different dimpled cylinders were reasonably close to each other. It was suggested that the level of drag reduction was found to be insensitive to different dimpled patterns.

CFD method was also used to calculate the drag coefficient for dimpled cylinders. However, this technique highly depended on the mesh of the geometry and grid quality. Therefore, any turbulent model from the RANS method did not seem to be appropriate. It then led to some pilot tests by using LES calculation without a sub-grid model, which seemed to be promising. But the main disadvantage was it required tremendous computer power to obtain valuable results.

In the experiments, flow behaviour was predominantly three-dimensional. However, in the pilot tests of CFD simulations, even two-dimensional calculations were very CPU expensive. It would be much worse for three-dimensional simulations. Wind tunnel testing was used as the main investigation technique and it served as a quicker way to obtain results compared to computational simulations in this project.

Therefore, compared with the experimental technique, computational simulation would not be suitable for seeking good answers to this project. By contrast, the experimental method would be more appropriate.

6.4 Time-Average Lift Coefficient and Repeatability of Experiments

From the experimental data, lift coefficient were also checked. Integrated values of C_l were very small for various Reynolds numbers. It helped to give more confidence of the experimental data because the time-average lift on the cylinder would be roughly cancelled out on the upper and lower halves of the cylinder.

Selected experiments were repeated, results were close to the original set, within the range of about 2%. Furthermore, some of the results were plotted with the error bar superimposed on the pressure coefficient curve. It also confirmed that the lower the Reynolds number, the bigger the drag coefficient. For example, near the region of $Re = 2 \times 10^4 \sim 3 \times 10^4$. At these Reynolds numbers, the error bars were found to be bigger than at other value of Reynolds number, e.g., $Re = 8 \times 10^4$. Besides, due to the high accuracy measurement and relatively simple circuit, the uncertainty level of the data was very good as well.

6.5 Flow Visualization

In the flow visualization part of the experiments, smoke generator, probes, and some other components were implemented in the original test rig. Suitable probe dimensions and mounting location were finally determined.

And then, wake regions behind smooth and dimpled cylinders were shown in the experiments. It was clear that the wake region was smaller behind the dimpled cylinder than that behind the smooth cylinder. Therefore, it supported conclusions drawn in previous chapters regarding dimpled cylinder could indeed reduce the stream-wise force on the cylinder.

Chapter 7

7. Suggestions on Possible Further Work

The following are a few recommendations concerning possible future work on this topic:

1. The experiments could be conducted at higher Reynolds numbers and the supercritical regime could be covered. Possible methods include carrying out experiments in a water tunnel and using bigger diameters of cylinders to achieve higher Reynolds numbers.
2. The flow could be simulated in both two and three-dimensional full Large Eddy Simulation (LES) when computer power allows.
3. The Particle Image Velocimetry (PIV) technique could be implemented in the flow visualization section. Therefore, closer and clearer images could be obtained of the flow inside dimples and on the dimple edges.
4. The cylinder tubes could use some more perfect circular cylinders, in order to obtain more accuracy pressure measurements.
5. As we can see in Figure 47 and Figure 50, even though the pressure tapplings have been tried to match dimple and cylinder on the curved outer surface due to the difficulties in machining two materials (cylinder tube

and pressure tappings). However, it was still not perfect. Future work can try to improve this aspect.

6. Make the dimples on the cylinder surface to be more uniform. For example, dimple diameter, depth, exact locations of dimples, etc. This could be achieved by making the tubes more carefully in the workshop or send the tubes to some commercial companies.

References

Achenbach, E. (1968), 'Distribution of local pressure and skin friction around a circular cylinder in cross-flow up to $Re = 5 \times 10^6$ ', *Journal of Fluid Mechanics* **34(4)**, 625–639

Achenbach, E. (1971), 'Influence of surface roughness on the cross flow around a circular cylinder', *Journal of Fluid Mechanics* **46(2)**, 321–335

Achenbach, E. (1974), 'The effects of surface roughness and tunnel blockage on the flow past spheres', *Journal of Fluid Mechanics* **65**, 113-125

Achenbach, E and Heinecke, E. (1981), 'On vortex shedding from smooth and rough cylinders in the range of Reynolds number 6×10^3 to 5×10^6 ', *Journal of Fluid Mechanics* **109**, 239–251

Anagnostopoulos, P. (2002), 'Flow-Induced Vibrations in Engineering Practice', published by WIT

Anderson Jr., J. D. (2001), 'Fundamentals of Aerodynamics' **third edition**, published by McGraw Hill

Batchelor, G. K. (2000), 'An Introduction to Fluid Dynamics', published by Cambridge University Press

Bearman, P. W. and Harvey, J. K. (1976), 'Golf Ball Aerodynamics', *Aeronautical Quarterly*, 112–122

Bearman, P. W. and Harvey, J. K. (1993), 'Control of circular cylinder flow by the use of dimples', *AIAA Journal* **31**, 1753–1756

Bearman, P. (2009), Personal email contacts with Professor Peter Bearman (p.bearman@imperial.ac.uk), Professor of Imperial College, UK, August 2009

Bloor, M. S. (1964), 'The transition to turbulence in the wake of a circular cylinder', *Journal of Fluid Mechanics* **19**, 290–304

Chang, P. K. (1970), 'Separation of Flow' **first edition**, published by Pergamon Press

Chang, P. K. (1976), 'Control of Flow Separation: Energy Conservation, Operational Efficiency, and Safety', published by Hemisphere Pub. Co.

Choi, J., Jeon, W. P. and Choi, H. (2006), 'Mechanism of drag reduction by dimples on a sphere', *Physics of Fluids* **18**, 041702

Chung, J. and Whitney, A. (1993), 'Flow-induced moment and lift for a circular cylinder with cable attachment', *International Journal of Offshore and Polar Engineering* **3-4**, December 1993

Chung, J. Whitney, A. Lezius, D. and Conti, R. J. (1994), 'Flow-induced torsional moment and vortex suppression for a circular cylinder with cables', *Proceedings of the 4th (1994) International Offshore and Polar Engineering Conference*, 10–15 April 1994, Osaka, Japan

Gerrard, J. H. (1966), 'The mechanics of the formation region of vortices behind bluff bodies', *Journal of Fluid Mechanics* **25**, 401–413

Gerrard, J. H. (1978), 'The wakes of cylindrical bluff bodies at low Reynolds number', *Transactions of the Royal Society London, Series A*, **288(A1354)**, 351–382

Igarishi, T. and Tsutsui, T. (1992), 'Flow control around a circular cylinder by a small cylinder', *11th Australasian Fluid Mechanics Conference*, 14–18

Igarishi, T. and Tsutsui, T. (1994), 'Fluid forces acting on a circular cylinder controlled by a small rod', *Proceedings of the Third JSME-KSME Fluids Engineering Conference*, 25–27 July 1994, Sendai, Japan

Igarishi, T. and Tsutsui, T. (1999), 'Flow control around a circular cylinder by a small cylinder (Properties of Reattachment Jet)', *Proceedings of the 3rd ASME/JSME Joint Fluids Engineering Conference*, 18–23 July 1999, San Francisco, California

Kimura, T. and Tsutahara, M. (1991), 'Fluid dynamic effects of grooves on circular cylinder surface', *AIAA Journal* **29**, 2062–2068

Kline, S. and McClintock, F. (1953), 'Describing uncertainties in single-sample experiments', *Mechanical Engineering*, 3-8

Lienhard, J. H. (1966), 'Synopsis of lift, drag, and vortex frequency data for rigid circular cylinders', *Technical Extension Service*

Maxworthy, T. (1969), 'Experiments on the flow around a sphere at high Reynolds numbers', *Journal of Applied Mechanics* **36(3)**, 598–607

Massey, B. (2005), 'Mechanics of Fluids' **8th edition**, published by Taylor & Francis

Moffat, R. (1982), 'Contributions to the theory of single-sample uncertainty analysis', *Transactions of the ASME*, **104**, 250-260

Nakamura, Y. and Tomonari, Y. (1982), 'The effects of surface roughness on the flow past circular cylinders at high Reynolds number', *Journal of Fluids Mechanics* **123**, 363–378

Owen, J. C., Bearman, P. W. and Szewczyk, A. A. (2001), 'Passive control of VIV with drag reduction', *Journal of Fluids and Structures* **15**, 597–605

Pidwirny, M (2006), 'Ocean Circulation', Water and Oceans

Prasad, A. and Williamson, C. H. K. (1997), 'A method for the reduction of bluff body drag', *Journal of Wind Engineering and Industrial Aerodynamics* **69–71**, 155–167

Sumer, B. M. and Fredsoe, J. (1999), 'Hydrodynamics Around Cylindrical Structures', published by World Scientific Publishing

Schlichting, H. and Gersten, K. (2000), 'Boundary Layer Theory' **8th edition**, published by Springer-Germany

Sakamoto, H. Tan, K. and Haniu, H. (1991), 'An optimum suppression of fluid forces by controlling a shear layer separated from a square prism', *Transition of ASME, Journal of Fluids Engineering* **113**, 183–189

Sakamoto, H. and Haniu, H. (1994), 'Optimum suppression of fluid forces acting on a circular cylinder', *Journal of Fluids Engineering* **116**, 221–227

Strykowski, P. J. and Sreenivasan, K. R. (1990), 'On the formation and suppression of vortex shedding at low Reynolds numbers', *Journal of Fluid Mechanics* **218**, 71–107

Szepessy, S. and Bearman, P. (1991), ‘Aspect ratio and end plate effects on vortex shedding from a circular cylinder’, *Journal of Fluid Mechanics* **234**, 191–217

‘The World’s Oceans and Seas’ (2007), published by Encarta

Ting, L. L. ‘Golf ball aerodynamic behaviour as affected by the dimple depth and dimple shape changes’

Ting, L. L. (2003), ‘Effect of dimple size and depth on golf ball aerodynamic performance’, *4th ASME–JSME Joint Fluids Engineering Conference*, Honolulu, Hawaii, USA, 6–11 July 2003

Ting, L. L. ‘Effect of teardrop shaped dimple design on the golf ball aerodynamic performance’

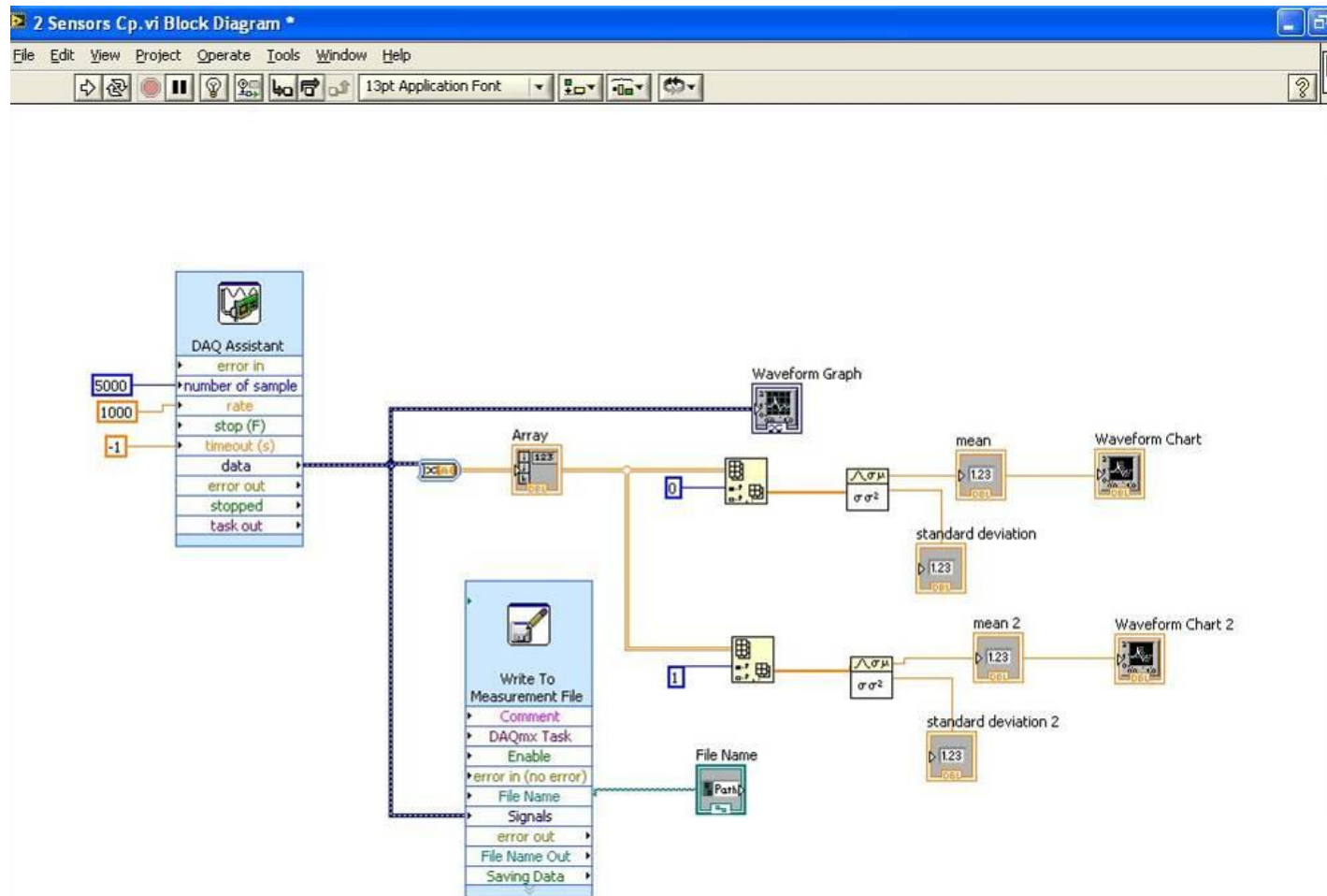
Tsutsui, T. and Igarashi, T. (2002), ‘Drag reduction of a circular cylinder in an air-stream’, *Journal of Wind Engineering and Industrial Aerodynamics* **90**, 527–541

White, F. M. (2003), ‘Fluid Mechanics’ **5th edition**, published by McGraw Hill

Williamson, C. H. K. (1988), ‘The existence of two stages in the transition to three-dimensionality of a cylinder wake’, *Physics of Fluids* **31(11)**, 3165–3168

Williamson, C. H. K. (1989), 'Oblique and parallel modes of vortex shedding in the wake of a circular cylinder at low Reynolds number', *Journal of Fluid Mechanics* **206**, 579–629

Appendix I – Schematics of the LabVIEW Code



Appendix II – A Sample of the Raw Experimental Data

Tap No.	No. of Samples x 12 (over 1 min)				Voltage Difference		
	Sensor 4 (Cylinder)	Std Dev. (Cylinder)	Sensor 5 (Pitot)	Std Dev. (Pitot)	Sensor 4 (Cylinder)	Sensor 5 (Pitot)	Cp (1 min)
0	3.169	0.037	3.146	0.032	3.169	3.146	1.007
1	3.000	0.070	3.139	0.030	3.000	3.139	0.956
2	2.687	0.108	3.142	0.031	2.687	3.142	0.855
3	2.278	0.146	3.140	0.031	2.278	3.140	0.725
4	1.720	0.161	3.141	0.030	1.720	3.141	0.548
5	1.350	0.080	3.137	0.030	1.350	3.137	0.430
6	1.193	0.328	3.141	0.031	1.193	3.141	0.380
7	1.340	0.395	3.138	0.030	1.340	3.138	0.427
8	1.417	0.257	3.139	0.030	1.417	3.139	0.451
9	1.430	0.320	3.139	0.030	1.430	3.139	0.456
10	1.442	0.318	3.139	0.030	1.442	3.139	0.459
11	1.442	0.297	3.144	0.032	1.442	3.144	0.459
12	1.431	0.317	3.141	0.030	1.431	3.141	0.456
13	1.411	0.314	3.137	0.030	1.411	3.137	0.450
14	1.397	0.326	3.140	0.031	1.397	3.140	0.445
15	1.383	0.315	3.138	0.030	1.383	3.138	0.441
16	1.366	0.260	3.140	0.031	1.366	3.140	0.435
17	1.370	0.226	3.141	0.031	1.370	3.141	0.436
18	1.374	0.219	3.138	0.030	1.374	3.138	0.438
19	1.373	0.288	3.138	0.031	1.373	3.138	0.438
20	1.380	0.330	3.138	0.030	1.380	3.138	0.440
21	1.399	0.324	3.138	0.030	1.399	3.138	0.446
22	1.415	0.207	3.142	0.032	1.415	3.142	0.450
23	1.432	0.327	3.137	0.031	1.432	3.137	0.456
24	1.442	0.327	3.138	0.030	1.442	3.138	0.460
25	1.440	0.309	3.139	0.031	1.440	3.139	0.459
26	1.441	0.332	3.140	0.031	1.441	3.140	0.459
27	1.422	0.386	3.140	0.031	1.422	3.140	0.453
28	1.278	0.388	3.138	0.031	1.278	3.138	0.407
29	1.279	0.291	3.136	0.031	1.279	3.136	0.408
30	1.541	0.240	3.141	0.031	1.541	3.141	0.491
31	1.904	0.191	3.139	0.032	1.904	3.139	0.607
32	2.297	0.141	3.141	0.032	2.297	3.141	0.731
33	2.716	0.104	3.135	0.030	2.716	3.135	0.866
34	3.022	0.060	3.136	0.031	3.022	3.136	0.964
35	3.177	0.033	3.139	0.032	3.177	3.139	1.012
36	3.165	0.036	3.138	0.031	3.165	3.138	1.009

Appendix III – Gantt Chart of the Project Progress

Preliminary Project Plan (from end of Nov-08, beginning of Dec-08)

ID	Task	2008		2009												2010 onwards							
		11	12	1	2	3	4	5	6	7	8	9	10	11	12	1	2	3	4	5	6	7	
1	Deliver the Intern Report	█																					
2	Detailed design of the experimental facilities		█	█																			
3	Components ordered or made			█	█																		
4	Review and design dimple configurations while waiting			█	█																		
5	Set up the whole test rig, make sure the wind tunnel and measurement instruments are working properly					█	█	█	█														
6	Test a smooth cylinder								█	█													
7	Different dimple designs in CFD									█	█	█	█	█	█	█	█	█	█	█	█	█	█
8	Test selected designs experimentally										█	█	█	█	█	█	█	█	█	█	█	█	█
9	Collect materials and write up 2009 Report													█	█								
10	Compare the results and propose a practical solution																				█	█	
11	Gather all the stuff and produce the Project Final Report																					█	█

